ADVERTIMENT. La consulta d'aquesta tesi queda condicionada a l'acceptació de les següents condicions d'ús: La difusió d'aquesta tesi per mitjà del servei TDX (www.tesisenxarxa.net) ha estat autoritzada pels titulars dels drets de propietat intel·lectual únicament per a usos privats emmarcats en activitats d'investigació i docència. No s'autoritza la seva reproducció amb finalitats de lucre ni la seva difusió i posada a disposició des d'un lloc aliè al servei TDX. No s'autoritza la presentació del seu contingut en una finestra o marc aliè a TDX (framing). Aquesta reserva de drets afecta tant al resum de presentació de la tesi com als seus continguts. En la utilització o cita de parts de la tesi és obligat indicar el nom de la persona autora.

ADVERTENCIA. La consulta de esta tesis queda condicionada a la aceptación de las siguientes condiciones de uso: La difusión de esta tesis por medio del servicio TDR (www.tesisenred.net) ha sido autorizada por los titulares de los derechos de propiedad intelectual únicamente para usos privados enmarcados en actividades de investigación y docencia. No se autoriza su reproducción con finalidades de lucro ni su difusión y puesta a disposición desde un sitio ajeno al servicio TDR. No se autoriza la presentación de su contenido en una ventana o marco ajeno a TDR (framing). Esta reserva de derechos afecta tanto al resumen de presentación de la tesis como a sus contenidos. En la utilización o cita de partes de la tesis es obligado indicar el nombre de la persona autora.

WARNING. On having consulted this thesis you're accepting the following use conditions: Spreading this thesis by the TDX (www.tesisenxarxa.net) service has been authorized by the titular of the intellectual property rights only for private uses placed in investigation and teaching activities. Reproduction with lucrative aims is not authorized neither its spreading and availability from a site foreign to the TDX service. Introducing its content in a window or frame foreign to the TDX service is not authorized (framing). This rights affect to the presentation summary of the thesis as well as to its contents. In the using or citation of parts of the thesis it's obliged to indicate the name of the author

Probing the Near-Field Optical Response of Plasmon Nanostructures with Two-Photon Luminescence Microscopy

Memoria de la tesis presentada por Petru Ghenuche para optar al grado de Doctor, mencion Doctor Europeo

Director de la tesis: Dr. **Romain Quidant**, Group leader del ICFO

Co-director de la tesis: Dr. **Gonal Badenes**, Group leader del ICFO

ICFO - Institut de Ciències Fotòniques

&

Departament de Física Aplicada y Simulación en Ciencias

Universitat Politècnica de Catalunya

Probing the Near-Field Optical Response of Plasmon Nanostructures with Two-Photon Luminescence Microscopy

Petru Ghenuche

ICFO - Institut de Ciències Fotòniques

UPC - Universitat Politècnica de Catalunya

A thesis submitted for the degree of

Doctor of Philosophy

February 16, 2009

Abstract

This thesis describes the design, fabrication and the optical characterization of plasmon-resonant systems able to confine and enhance light fields down to the sub-wavelength scale. Extensive 3D numerical modeling was first used to design different geometries of coupled plasmonic nanostructures through the calculation of their far-field and near-field optical response. On the basis of simulations, the nanostructures were fabricated by e-beam lithography and thin film deposition. Special efforts were devoted to increasing the resolution and optimizing the reproducibility of critical parameters such as particle shape and interparticle gaps. Finally, far-field spectroscopy combined with two-photon induced luminescence (TPL) spectroscopy was used to probe the local optical response of the optimized architectures.

We focused our attention on different families of structures: metal dimers, bar antennas, finite chains of nanoparticles and star-like particle arrangements. Particle dimers feature strong field enhancements in their sub-wavelength gap due to near-field coupling of their dipolar localized plasmon resonances. Based on the same physics, gap antennas, formed by two adjacent gold bars supporting multipolar resonances can efficiently couple to propagating light and concentrate it into tiny volumes. While finite particle chains were previously shown by other authors to be good candidates to guide light through sub-wavelength cross-sections, we show here that they can also be used

as efficient nanolenses able to concentrate light at their extremity. Finally, the near-field distribution in star-like arrangements of gold nanoparticles exhibits a strong dependence with the incident field polarization which can be exploited for dynamical optical addressing of nano-objects.

We have compared the far field spectroscopy of large ensembles of dimers and finite chains to TPL spectroscopy. Our main result is to show that TPL is preferentially sensitive to local fields and that it enables the assessment of spectroscopic features which cannot be resolved otherwise. In order to overcome the limitations of measurements on large ensembles a considerable effort was dedicated to mounting and optimizing an optical set-up enabling TPL measurement of single structures.

Using the developed TPL micro-spectroscopy, spatially resolved spectral mode mapping on single resonant gap-antennas was achieved. As predicted by calculations, we were able to directly visualize at resonance the strongly enhanced TPL signal within the gap. Our results show how TPL scans can be directly compared with the convoluted distribution of the fourth power of the calculated local mode field. By monitoring the evolution with the incident wavelength of the TPL signal within the gap and at the antenna extremities we got further insight in the physical mechanism behind the buildup of the antenna's resonance.

Finally, TPL microscopy was used to probe the local fields under different orientations of the incident linear polarization near star-like arrangement of gold disks. It is shown that, unlike the scattering spectrum, the TPL distribution over the structure is found to depend drastically on the incident polarization state.

Our study brings a significant contribution to the field of plasmon optics by proposing novel geometries able to efficiently confine optical fields down to the nanometric scale, but also by providing deep insight into the use of TPL microspectroscopy to probe their local optical response. Our findings are foreseen to be important in applications such as enhanced spectroscopy, bio-sensing and enhanced light-matter interaction, where one needs to assess the actual field experienced by small amounts of matter.

Resumen

Esta tesis describe el diseño, la fabricación y la caracterización óptica de sistemas plasmónicos resonantes capaces de confinar y aumentar campos de luz en la escala manométrica. En primer lugar, se utilizaron modelos numéricos 3D para diseñar diferentes geometras de nanoestructuras plasmónicas acopladas, a través del cálculo de la respuesta óptica de su campo lejano y cercano. Sobre la base de estas simulaciones se fabricaron las nanoestructuras por litografía de haz electrónico. Se puso especial énfasis en el aumento de la resolución y la optimización de la reproducibilidad de parámetros críticos como la forma de las partículas y el gap entre ellas. Por último, se empleó espectroscopía de campo lejano combinada con espectroscopía de luminiscencia inducida por dos fotones (TPL) para sondar la respuesta óptica local de las geometrías optimizadas.

Hemos centrado nuestra atención en diferentes tipos de estructuras metálicas: dímeros, antenas con gap, conjuntos finitos de partículas en cadenas y en forma de estrella. Los dímeros tienen una fuerte amplificación del campo en su gap nanométrico por el acoplamiento en campo cercano de sus resonancias plasmonicas dipolares. Análogamente, antenas con gap, formadas por dos barras de oro adyacentes que soportan resonancias multipolares, pueden acoplar de manera eficiente la luz y concentrarla en volúmenes pequeños. Se ha demostrado que cadenas finitas de partículas son buenos candidatos para guiar la luz a través de secciones transversales por debajo de la longitud de onda y aquidemostramos que también se pueden utilizar como nanolentes capaces de concentrar la luz en su extremo. La distribución del campo

cercano en conjuntos de partículas de oro en forma de estrella presenta una fuerte dependencia con la polarización del campo incidente que puede ser explotada para dirigirse dinámicamente a nano-objetos.

La espectroscopía de campo lejano de conjuntos de dímeros y de cadenas finitas de partculas se comparó con la espectroscopía de TPL. Nuestro principal resultado es mostrar que la TPL es preferentemente sensible a los campos locales, permitiendo evaluar características espectroscópicas que no podrían resolverse de otro modo. A fin de superar las limitaciones de las medidas de conjuntos, en una segunda etapa se dedicó un considerable esfuerzo a construir y optimizar un montaje óptico para medir la señal de TPL de estructuras únicas. El uso de la micro-espectroscopía de TPL permitió obtener mapas espectrales de los modos de antenas aisladas con resolución espacial. Como se predijo mediante cálculos, hemos sido capaces de visualizar directamente, en la resonancia, la señal de TPL amplificada dentro del gap. Nuestros resultados muestran cómo las medidas de TPL pueden compararse directamente con la distribución de la cuarta potencia del campo local calculado. Mediante el análisis de la evolución de la señal de TPL en función de la longitud de onda incidente en el gap y en las extremidades de la antena tenemos más conocimiento sobre el mecanismo físico detrás de la resonancia de la antena. Finalmente, la microscopía de TPL se utilizó para sondar el campo cercano para diferentes orientaciones de la polarización lineal incidente sobre los conjuntos de partículas en forma de estrella. Se demuestra que, a diferencia del espectro de dispersión, la distribución de TPL en la estructura depende drásticamente del estado de polarización incidente.

Nuestro estudio aporta una contribución significativa al campo de la óptica de plasmones, proponiendo nuevas geometrías para confinar de

manera eficiente los campos ópticos a la escala nanometrica, aportando un profundo conocimiento sobre el uso de micro-espectroscopa de TPL como sonda óptica local. Nuestros resultados tendrán importancia en aplicaciones tales como espectroscopía mejorada, biosensores y la interacción luz-materia, donde se necesita evaluar el campo experimentado por una pequeña cantidad de materia cercana a la nanoestructura.

Chapter 1

Introduction

1.1 Nano-optics: Extending optics down to the subwavelength scale

In the last decade, the need for smaller and faster devices has considerably increased the interest in nano-optics, the area of photonics that deals with the optics of nanostructures with dimensions beyond the diffraction limit of light [Novotny & Hecht (2006)]. These studies have already moved from fundamental studies of microscopy and spectroscopy to the development of applications in areas ranging from optical circuits [Almeida *et al.* (2004)], sensors [Kreuzer *et al.* (2006)], trapping [Quidant & Girard (2008)] to data processing [Bozhevolnyi *et al.* (2006)].

In particular, optical approaches are very attractive for the elaboration of future chips formed by distributed architectures in which a multitude of fast electronic computing units need to be connected by high-speed links. However the large size mismatch between electronic and dielectric photonic components prevents their immediate implementation. The section of dielectric photonic devices is limited in size by the fundamental laws of diffraction to about half the effective wavelength of light and tend to be at least one or two orders of magnitude larger than their nano-scale electronic counterparts [Ozbay (2006); Zia *et al.* (2006)].

Another challenge of nano-optics involves the optimization of the interaction of light with nanometer volumes of matter down to the molecular level (figure 1.1). The confinement of light fields down to dimensions much smaller than the incident wavelength combined with high field magnitudes is expected to have a crucial impact to the elaboration of future nano-devices such as optical switches, optical detectors and sources.

Independently, in confining light in volumes much smaller than its wavelength, conventional far field microscopy methods are not suitable to characterize nano-optical functionalities. There is thus a need for optical methods able to probe evanescent fields bound to nano-objects [Vigoureux & Courjon (1992);Drezet *et al.* (2006)].

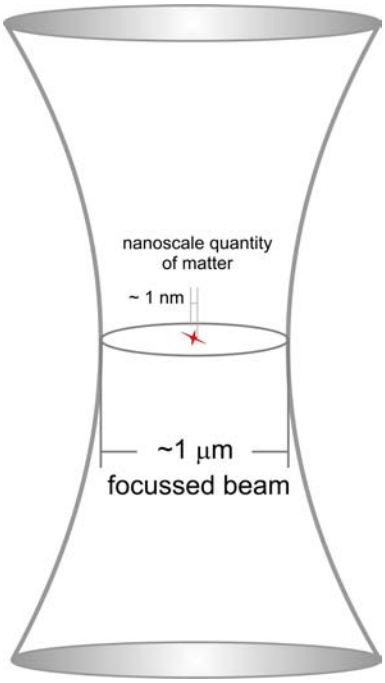

Figure 1.1: *In conventional optics the diffraction limit prevents the efficient optical control of light in subwavelength volumes. Different strategies have to be applied to bridge micro- and nano-scale and to improve the interaction of light with small quantities of matter down to the molecular level.*

1.2 Different strategies of nano-optics

Several strategies have been considered to control light at the nanoscale [Huang *et al.* (2008); Jahns *et al.* (2008); Zayats *et al.* (2005)]. Generally speaking, simple Fourier considerations explain why propagating waves cannot be focused to volumes much smaller than the wavelength. Increasing the spatial confinement along one component causes an evanescent behavior on the others as showed by the following two equations:

$$\Delta i \, \Delta k_i \geq 2\pi \ , \ i = x, y, z \tag{1.1}$$

$$k = \sqrt{{k_x}^2 + {k_y}^2 + {k_z}^2} = \frac{2\pi}{\lambda} \tag{1.2}$$

This is the result of the purely imaginary wave vector component in the later direction, necessary to compensate for the enlarged wave vector component [Novotny & Hecht (2006)].

Among the main promising approaches for focusing light to sub-λ volumes is the "super lens" proposed by Pendry (2000). A superlens composed of left-handed material ($\mu < 0,\ \epsilon < 0$) can amplify evanescent waves to form a "perfect" image. Five years later, Fang *et al.* (2005) experimentally demonstrated the concept of the superlens by using of a very thin silver film able to resolve 60-nanometer half-pitch resolution, or one-sixth of the illumination wavelength. While its application has been limited to the near-field, latest elaborations have permitted to form images with sub-diffracted limited features in the far-field [Liu *et al.* (2007)].

Another attractive concept is based on the photonic crystals allows the control the dispersion and propagation of light through a periodic modulation of the dielectric function [Noda *et al.* (2000)]. The most known effects include rejection of light in given wavelength window by Bragg reflection and waveguiding of light along linear and bent channels of defects. The application of photonic bandgap structures has already led to remarkable breakthroughs in optical integration providing interconnection between elements of photonic circuits and a relatively well-developed element base of passive components, such as filters, waveguides and nanocavities. Photonic bandgap (PBG) crystals are artificial systems that also enable concentrating light in small finite cavities formed by defects. Recently it has been demonstrated that a photonic double-heterostructure can be used to create nanocavities with extremely high-Q factors [Song *et al.* (2005)]. Also, a dynamic change of the Q factor of a subwavelength nanocavity on a picosecond timescale was achieved by Tanaka *et al.* (2007) by using a system combining a nanocavity, a nonlinear waveguide and a hetero-interface mirror.

Optical microcavities confine light to small volumes by resonant recirculation. In addition to ultrahigh-finesse Fabry-Perot microcavities, the whispering gallery modes of silica microspheres have received considerable attention. Devices based on optical microcavities are already implemented in applications like long-distance

transmission of data over optical fibres, narrow spot-size laser read/write beams in optical players [Braginsky *et al.* (1989); Kippenberg & Vahala (2008); Vahala (2003)].

Besides, the implementation of all-optical integrated circuits also requires (active) non-linear photonic elements capable of performing, optically, logic operations analogous to their electronic counterparts. While linear optical properties and light manipulation are significantly evolved, the effects relying on non-linear optical interactions required for the development of truly all-optical integrated circuits are much less advanced.

1.3 Plasmon optics

Alternatively to the above mentioned approaches, metal nanostructures sustaining surface plasmons (SP) may possess the right combination of electronic and optical properties to tackle some of the issues outlined above, offering the opportunity of extending optics down to the subwavelength scale [Barnes *et al.* (2003)] and realizing significantly faster processing speeds.

SPs are electromagnetic waves that are confined to the interface between materials with dielectric constants of opposite sign (typically, noble metal films in contact with a dielectric) [Kreibig (1995)]. Depending on the geometry of the metal, two distinct types of surface plasmons can be identified. Surface Plasmon Polaritons (SPP) sustained at a flat metal/dielectric interface are propagating electromagnetic surface waves associated to a collective oscillation of the free electrons of the metal with the incident electromagnetic field. Unlike SPP on flat and extended metal interfaces, Localized Surface Plasmons (LSP) are associated with bound electron plasmas in nano-voids or particles with dimensions much smaller than the incident wavelength. Whilst SPP have a continuous dispersion relation and therefore exist over a wide range of frequencies, LSP resonances only exist over a narrow frequency range owing to additional constraints imposed by their finite dimensions. The spectral position of this resonance is governed by

the particles size and shape and by the dielectric functions of both the metal and the surrounding media. In contrast to SPP, LSP can be directly coupled with propagating light; indeed their enhanced scattering cross-section at resonance makes them very efficient antennas [Cesario *et al.* (2007)].

With the development of scanning near-field optical microscopy (SNOM) it has become possible to study the surface polariton fields directly in the near-field proximity of the surface where they bound. The SPP scattering, interference, backscattering and localization have been visualized and investigated in direct space. The idea of two-dimensional surface polariton optics has been proposed and realized experimentally resulting in the development of optical elements for surface polaritons that allow SPP light to be manipulated and directed in the same way as optical beams are directed in three dimensions [Ditlbacher *et al.* (2002b); Hohenau *et al.* (2005)].

Beyond the intrinsic enhancement and confinement of fields nearby an isolated particle, significantly stronger optical energy concentration can be achieved when involving the electromagnetic coupling between several objects. In particular, it is now well known that pairs of particles (also known as coupled antennas) separated by a dielectric nano-gap are capable of confining the local fields well beyond the diffraction limit [Muhlschlegel *et al.* (2005); Novotny (2007); Righini *et al.* (2009); Schuck *et al.* (2005)]. This property has already opened new opportunities in ultra sensitive sensing of biomolecules [Aćimović *et al.* (2008); Bauer *et al.* (2003); Enoch *et al.* (2004)], enhanced spectroscopy [Chang & Furtak (1982)] and in enhancing the efficiency of photon sources and detectors [Muskens *et al.* (2007); Tang *et al.* (2008)]. More recently there has been a growing interest in exploiting such concepts to achieve dynamical spatial control of the subwavelength optical fields [Aeschlimann *et al.* (2007)]. Dynamical control of electromagnetic fields at the nanoscale is anticipated to have applications in the domains of nano-optical multiplexing, all-optical photonic chips and selective optical addressing of isolated nano-objects.

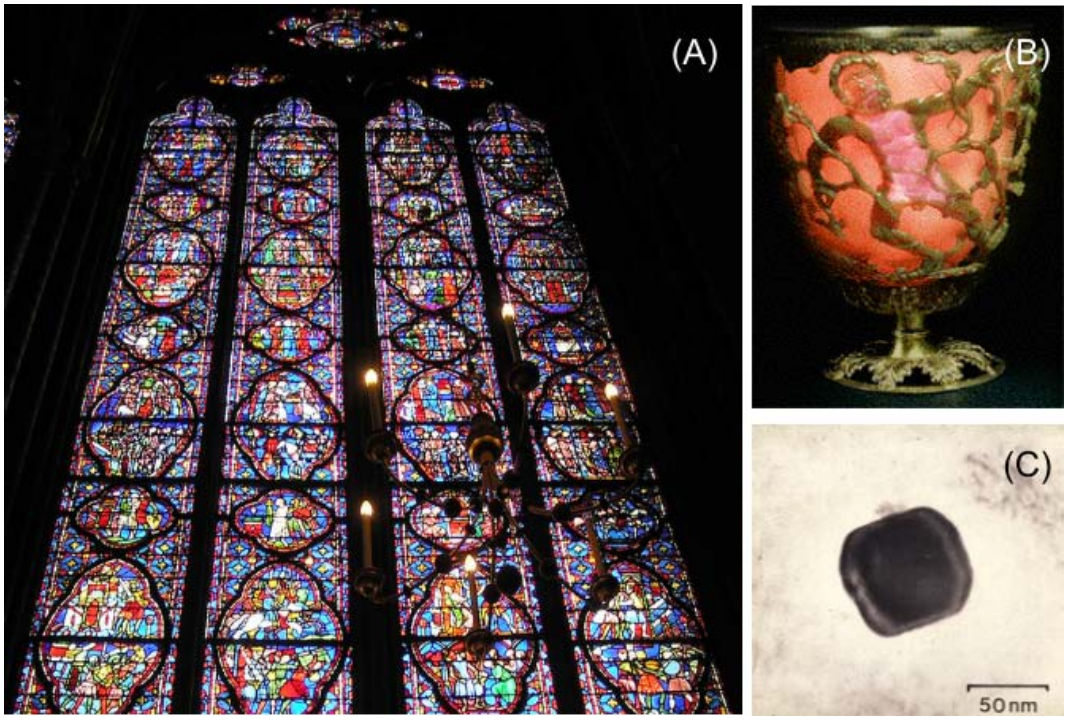

Figure 1.2: *Nano-optics in stained-glass. The makers achieved deep colors by dissolving small particles of metal in the molten glass. The surface plasmons of the nanosized particles cause them to reflect the colors selectively. (A) Stained-glass window of Sainte-Chapelle, Paris (13th century), (B-C) The Lycurgus cup (4th century) and electron microscopy revealing the gold nanoparticles (courtesy of the British museum).*

SPP elements can be fabricated with conventional lithography techniques such as e-beam and focused ion beam (FIB) milling in a 'top-down' approach [Dragoman & Dragoman (2008); Lal *et al.* (2007)]. Electron beam lithography is the most popular method, especially for thin structures with nanosized dimensions. Alternatively, nanoparticles or nanowires chemically synthesized can be used ('bottom-up' approach). While this approach is very attractive for the metal crystallinity which confers improved optical properties such as sharper and stronger resonances, colloids can not be arranged in a controlled fashion. The bottom-up approach is well represented by the self-assembly techniques and pro-

cesses.

Beyond the issues of fabrication, the SPP confined in small volumes are difficult to measure and model. Various tip-less methods exist to study SPPs. The detection of the leakage radiation (LR) emitted by plasmons, as they propagate along the substrate/metal/air system, into a higher refractive index substrate, is often used. Although LR contributes to SPP losses, it also permits the direct far-field detection of the SPP spatial intensity distribution [Hecht *et al.* (1996); Stepanov *et al.* (2005)]. More recently, fluorescent probes were proposed by Ditlbacher *et al.* (2002a). These techniques made possible the imaging of bound modes, but with a diffraction limit resolution. Alternatively Kubo *et al.* (2005) combined interferometric time-resolved two-photon photoemission with photoelectron emission microscopy (PEEM). The main drawback of PEEM is that it requires cumbersome and expensive equipements.

Near-field microscopy [Betzig & Trautman (1992); Durig *et al.* (1986)] or a photon scanning tunnelling microscope (PSTM), is another technique that can overcome the diffraction limit and measure the SPPs [Weeber *et al.* (2001)]. A PSTM uses a near-field probe (an optical fiber with a nm scale aperture) instead of a lens. As the probe is brought within a few nanometer of the metal surface, part of the evanescent tail of the SPP is able to couple to the probe, and is subsequently detected in the far-field. Multiple studies using a PSTM on (guided) SPPs are reported in literature over the last couple of years [Barnes *et al.* (2003); Bozhevolnyi *et al.* (2006)]. However in the case of plasmonic nanostructures very sensitive to their dielectric environment, the probe itself can interfere with the intrinsic properties of the structure under study and affects the resonance conditions or the actual local field distribution, as shown by Koenderink *et al.* (2005). Therefore, in this case, approaches free of scanning tips are preferred, despite their limited spatial resolution [Felidj *et al.* (2006)]

Among alternative techniques sensitive to local fields near plasmon nanostructures, nonlinear far-field microscopy has recently gained some interest. Owing to their dependence with the second or higher power of the field, nonlinear processes

are preferentially sensitive to the most intense field bound to the metal. Raman scattering imaging has shown to provide an indirect information on the near field along metal rods [Felidj *et al.* (2006)]. Furthermore, scanning confocal microscopy based on detecting two photon luminescence (TPL) of gold has recently shown to be well suited to probe the local optical response of gold nanostructures [Beversluis *et al.* (2003); Bouhelier *et al.* (2005); Hohenau *et al.* (2006)]. However, to date, there is no study of the actual relation between TPL and the local response of gold plasmonic structures.

1.4 Outline

This thesis is dedicated to the study of plasmonic structures that are able to concentrate light in nanometric volumes using two photon induced luminescence microscopy. Our work has relied on a permanent interaction between numerical design, nanofabrication and optical characterization. We have designed and fabricated different architecture of plasmonic systems and performed a systematic study by TPL micro-spectroscopy. Our results show how TPL spectra and maps can be directly compared with calculated spectroscopy and the distribution of the fourth power of the local electric field.

The manuscript is organized as follows:

In chapter 2, extensive calculations performed using the Green dyadic method are used to predict the far- and near-field behavior of ensembles of coupled metallic nanoparticles: dimers and finite chains. The experimental results show that the TPL spectra can provide additional data on the electromagnetic modes of the nanostructures, being able to resolve the finest resonant features that are not assessed with conventional linear spectroscopy.

Chapter 3 focuses on a detailed description of an optical setup specially developed for single nanostructures characterization, its resolution and the TPL nature of the signal. Chapter 4 describes the high resolution mode mapping and spectroscopy of single nanoantennas. Finally, in the last part, the technique is

applied to a different system to show the applicability of TPL microscopy to different gold plasmonic samples.

References

Aćimović, S., Kreuzer, M.P., González, M.U. & Quidant, R. (2008). Plasmon near-field coupling in metal dimers as a step towards single molecule sensing. *Nano. Lett.*, **submitted**. 6

Aeschlimann, M., Bauer, M., Bayer, D., Brixner, T., Garcia de Abajo, F.J., Pfeiffer, W., Rohmer, M., Spindler, C. & Steeb, F. (2007). Adaptive subwavelength control of nano-optical fields. *Nature*, **446**, 301–304. 6

Almeida, V.R., Barrios, C.A., Panepucci, R.R. & Lipson, M. (2004). All-optical control of light on a silicon chip. *Nature*, **431**, 1081–1084. 2

Barnes, W.L., Dereux, A. & Ebbesen, T.W. (2003). Surface plasmon subwavelength optics. *Nature*, **424**, 824–830. 5, 8

Bauer, G., Hassmann, J., Walter, H., Haglmuller, J., Mayer, C. & Schalkhammer, T. (2003). Resonant nanocluster technology - from optical coding and high quality security features to biochips. *Nanotechnology*, **14**, 1289–1311. 6

Betzig, E. & Trautman, J.K. (1992). Near-Field Optics: Microscopy, Spectroscopy, and Surface Modification Beyond the Diffraction Limit. *Science*, **257**, 189–195. 8

REFERENCES

Beversluis, M.R., Bouhelier, A. & Novotny, L. (2003). Continuum generation from single gold nanostructures through near-field mediated intraband transitions. *Phys. Rev. B*, **68**, 115433. 9

Bouhelier, A., Bachelot, R., Lerondel, G., Kostcheev, S., Royer, P. & Wiederrecht, G.P. (2005). Surface plasmon characteristics of tunable photoluminescence in single gold nanorods. *Phys. Rev. Lett.*, **95**, 267405. 9

Bozhevolnyi, S.I., Volkov, V.S., Devaux, E., Laluet, J.Y. & Ebbesen, T.W. (2006). Channel plasmon subwavelength waveguide components including interferometers and ring resonators. *Nature*, **440**, 508–511. 2, 8

Braginsky, V.B., Gorodetsky, M.L. & Ilchenko, V.S. (1989). Quality-factor and nonlinear properties of optical whispering-gallery modes. *Phys. Lett. A*, **137**, 393–397. 5

Cesario, J., Gonzalez, M.U., Cheylan, S., Barnes, W.L., Enoch, S. & Quidant, R. (2007). Coupling localized and extended plasmons to improve the light extraction through metal films. *Opt. Express*, **15**, 10533–10539. 6

Chang, R.K. & Furtak, T.E., eds. (1982). *Surface Enhanced Raman Scattering*. Plenum Press, New York. 6

Ditlbacher, H., Krenn, J.R., Felidj, N., Lamprecht, B., Schider, G., Salerno, M., Leitner, A. & Aussenegg, F.R. (2002a). Fluorescence imaging of surface plasmon fields. *Appl. Phys. Lett.*, **80**, 404–406. 8

Ditlbacher, H., Krenn, J.R., Schider, G., Leitner, A. & Aussenegg, F.R. (2002b). Two-dimensional optics with surface plasmon polaritons. *Appl. Phys. Lett.*, **81**, 1762–1764. 6

Dragoman, M. & Dragoman, D. (2008). Plasmonics: Applications to nanoscale terahertz and optical devices. *Prog. Quant. Electron.*, **32**, 1–41. 7

Drezet, A., Hohenau, A. & Krenn, J.R. (2006). Heisenberg optical near-field microscope. *Phys. Rev. A*, **73**, 013402. 2

Durig, U., Pohl, D.W. & Rohner, F. (1986). Near-field optical-scanning microscopy. *J. Appl. Phys.*, **59**, 3318–3327. 8

Enoch, S., Quidant, R. & Badenes, G. (2004). Optical sensing based on plasmon coupling in nanoparticle arrays. *Opt. Express*, **12**, 3422. 6

Fang, N., Lee, H., Sun, C. & Zhang, X. (2005). Sub-diffraction-limited optical imaging with a silver superlens. *Science*, **308**, 534–537. 4

Felidj, N., Laurent, G., Grand, J., Aubard, J., Levy, G., Hohenau, A., Aussenegg, F. & Krenn, J.R. (2006). Far-field raman imaging of short-wavelength particle plasmons on gold nanorods. *Plasmonics*, **1**, 35. 8, 9

Hecht, B., Bielefeldt, H., Novotny, L., Inouye, Y. & Pohl, D.W. (1996). Local excitation, scattering, and interference of surface plasmons. *Phys. Rev. Lett.*, **77**, 1889–1892. 8

Hohenau, A., Krenn, J.R., Stepanov, A.L., Drezet, A., Ditlbacher, H., Steinberger, B., Leitner, A. & Aussenegg, F.R. (2005). Dielectric optical elements for surface plasmons. *Opt. Lett.*, **30**, 893–895. 6

Hohenau, A., Krenn, J.R., Beermann, J., Bozhevolnyi, S.I., Rodrigo, S.G., Martin-Moreno, L. & Garcia-Vidal, F. (2006). Spectroscopy and nonlinear microscopy of au nanoparticle arrays: Experiment and theory. *Phys. Rev. B*, **73**, 155404. 9

Huang, F.M., Kao, T.S., Fedotov, V.A., Chen, Y. & Zheludev, N.I. (2008). Nanohole array as a lens. *Nano Lett.*, **8**, 2469–2472. 3

Jahns, J., Cao, Q. & Sinzinger, S. (2008). Micro- and nanooptics - an overview. *Laser & Photon. Rev.*, **2**, 249–263. 3

REFERENCES

Kippenberg, T.J. & Vahala, K.J. (2008). Cavity optomechanics: Back-action at the mesoscale. *Science*, **321**, 1172. 5

Koenderink, A.F., Kafesaki, M., Buchler, B.C. & Sandoghdar, V. (2005). Controlling the resonance of a photonic crystal microcavity by a near-field probe. *Phys. Rev. Lett.*, **95**, 153904. 8

Kreibig, M., Uwe; Vollmer (1995). *Optical Properties of Metal Clusters*. Springer-Verlag. 5

Kreuzer, M.P., Quidant, R., Badenes, G. & Marco, M.P. (2006). Quantitative detection of doping substances by a localised surface plasmon sensor. *Biosens. Bioelectron.*, **21**, 1345–1349. 2

Kubo, A., Onda, K., Petek, H., Sun, Z., Jung, Y. & Kim, H. (2005). Femtosecond imaging of surface plasmon dynamics in a nanostructured silver film. *Nano Lett.*, **5**, 1123–1127. 8

Lal, S., Link, S. & Halas, N.J. (2007). Nano-optics from sensing to waveguiding. *Nat. Photon.*, **1**, 641–648. 7

Liu, Z., Lee, H., Xiong, Y., Sun, C. & Zhang, X. (2007). Far-Field Optical Hyperlens Magnifying Sub-Diffraction-Limited Objects. *Science*, **315**, 1686–. 4

Muhlschlegel, P., Eisler, H.J., Martin, O.J.F., Hecht, B. & Pohl, D.W. (2005). Resonant optical antennas. *Science*, **308**, 1607. 6

Muskens, O., Giannini, V., Sanchez-Gil, J. & GomezRivas, J. (2007). Strong enhancement of the radiative decay rate of emitters by single plasmonic nanoantennas. *Nano Lett.*, **7**, 2871–2875. 6

Noda, S., Tomoda, K., Yamamoto, N. & Chutinan, A. (2000). Full Three-Dimensional Photonic Bandgap Crystals at Near-Infrared Wavelengths. *Science*, **289**, 604–606. 4

Novotny, L. (2007). Effective wavelength scaling for optical antennas. *Phys. Rev. Lett.*, **98**, 266802. 6

Novotny, L. & Hecht, B. (2006). *Principles of Nano-Optics*. Cambridge University Press, Cambridge, England. 2, 4

Ozbay, E. (2006). Plasmonics: Merging photonics and electronics at nanoscale dimensions. *Science*, **311**, 189–193. 2

Pendry, J.B. (2000). Negative refraction makes a perfect lens. *Phys. Rev. Lett.*, **85**, 3966–3969. 4

Quidant, R. & Girard, C. (2008). Surface-plasmon-based optical manipulation. *Laser & Photon. Rev.*, **2**, 47–57. 2

Righini, M., Ghenuche, P., Cherukulappurath, S., Myroshnychenko, V., Garcia de Abajo, F.J. & Quidant, R. (2009). Nano-optical trapping of rayleigh particles and escherichia coli bacteria with resonant optical antennas. *Nano Letters*. 6

Schuck, P.J., Fromm, D.P., Sundaramurthy, A., Kino, G.S. & Moerner, W.E. (2005). Improving the mismatch between light and nanoscale objects with gold bowtie nanoantennas. *Phys. Rev. Lett.*, **94**, 017402. 6

Song, B.S., Noda, S., Asano, T. & Akahane, Y. (2005). Ultra-high-q photonic double-heterostructure nanocavity. *Nat. Mater.*, **4**, 207. 4

Stepanov, A.L., Krenn, J.R., Ditlbacher, H., Hohenau, A., Drezet, A., Steinberger, B., Leitner, A. & Aussenegg, F.R. (2005). Quantitative analysis of surface plasmon interaction with silver nanoparticles. *Opt. Lett.*, **30**, 1524–1526. 8

Tanaka, Y., Upham, J., Nagashima, T., Sugiya, T., Asano, T. & Noda, S. (2007). Dynamic control of the q factor in a photonic crystal nanocavity. *Nat. Mater.*, **6**, 862. 4

REFERENCES

Tang, L., Kocabas, S.E., Latif, S., Okyay, A., Ly-Gagnon, D., Saraswat, K. & Miller, D.A.B. (2008). Nanometre-scale germanium photodetector enhanced by a near-infrared dipole antenna. *Nat. Photon.*, **2**, 226. 6

Vahala, K.J. (2003). Optical microcavities. *Nature*, **424**, 839–849. 5

Vigoureux, J.M. & Courjon, D. (1992). Detection of nonradiative fields in light of the heisenberg uncertainty principle and the rayleigh criterion. *Appl. Opt.*, **31**, 3170–3177. 2

Weeber, J.C., Krenn, J.R., Dereux, A., Lamprecht, B., Lacroute, Y. & Goudonnet, J.P. (2001). Near-field observation of surface plasmon polariton propagation on thin metal stripes. *Phys. Rev. B*, **64**, 045411. 8

Zayats, A.V., Smolyaninov, I.I. & Maradudin, A.A. (2005). Nano-optics of surface plasmon polaritons. *Phys. Rep.*, **408**, 131–314. 3

Zia, R., Schuller, J.A., Chandran, A. & Brongersma, M.L. (2006). Plasmonics: the next chip-scale technology. *Materials Today*, **9**, 20–27. 2

Chapter 1

TPL measurements on ensembles of coupled metallic nanoparticles

1.1 Introduction

The use of the electromagnetic coupling between metallic nanostructures is known to be a powerful approach to generate strong optical field enhancement combined with high confinement in volumes below the diffraction limit [Kottmann & Martin (2001a)]. However, measuring subwavelength light confinement remains a major challenge, specially when it reaches dimensions beyond the maximum resolution of near-field optical microscopy [Hillenbrand *et al.* (2003)].

Probing the actual, unperturbed local field near plasmonic nanostructures is particularly needed when one wants to optimize their interaction with a nearby small quantity of mater (e.g. a molecule), since the object will mainly respond to the electric near-field intensity. Therefore, in order to understand their interaction one needs to look at the near-field spectroscopy of the metal host rather than its (far-field) scattering or extinction spectroscopy. This becomes particularly critical when the metallic system is large enough to experience some retardation effects. In that case indeed, the local field spectroscopy may display important differences with the far-field, as evidenced by Messinger *et al.* (1981).

Recently, several works have shown that TPL microscopy can provide information on the local optical response of resonant gold nanostructures [Beversluis *et al.* (2003)]. Indeed, due to the non linear nature of its excitation, the TPL signal is proportional to the fourth power of the electromagnetic field in the metal. For this reason the TPL is more sensitive to high local fields.

In this study, two geometries of coupled plasmonic structures: dimers and finite chains of gold nanoparticles (figure 1.1) are investigated:

a. Dimers: The dimer geometries are formed by two closely spaced nanoparticles separated by an air gap of length $\delta \ll \lambda$. The accumulations of surface charges occurring in the space between the particles when driving the structure with a field polarized along the main dimer axis leads to confined high local field in their gap [Kottmann & Martin (2001a); Lereu *et al.* (2008); Zhdanov *et al.* (2008)].

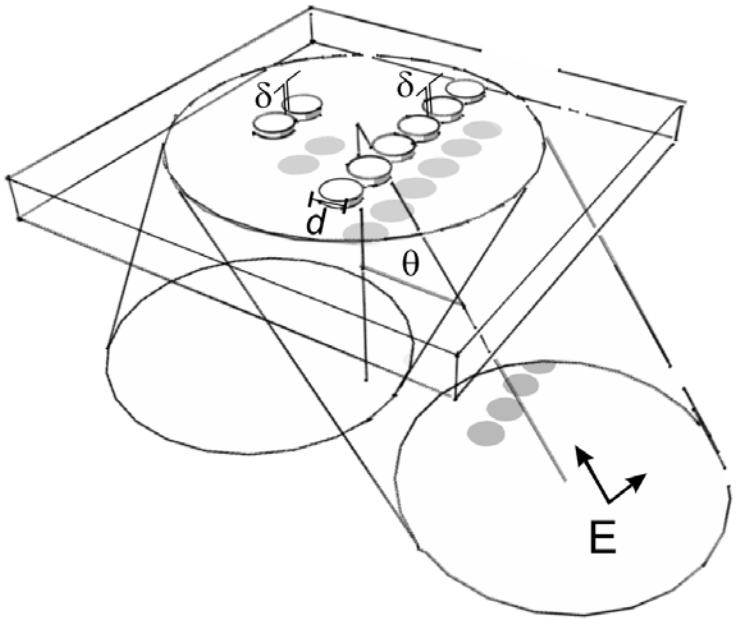

Figure 1.1: *Description of the optical configuration. The particles are lying onto a glass substrate. The illumination is performed by a linearly polarized plane wave with incident angle θ.*

b. Chains have attracted recently a lot of attention for their ability to confine [Krenn *et al.* (1999a)] and guide light through subwavelength cross-sections [Maier *et al.* (2003); Quinten *et al.* (1998)]. Moreover, as will be shown bellow, under extended illumination, an intense and sub-λ free-space hot spot of similar magnitude than reported for nanometer gap systems can be achieved.

Linear (scattering) and nonlinear (TPL) spectroscopy have been performed and compared for both types of structures. In certain configurations, where the local field is strongly enhanced, TPL spectroscopy is able to retrieve further information about the system than the linear technique.

In the first part of this chapter the concept of two photon induced luminescence is discussed. In the following section the Green dyadic method is used to investigate the spectroscopic properties of the structures and their near field. Next, the sample and the the optical setups are described. In the second part

of the chapter, the experimental results for the two investigated geometries are presented.

1.2 Two-photon luminescence in gold nanoparticles

Nonlinear far-field microscopy has recently gained interest among the alternative techniques to SNOM able to probe local surface plasmon fields [Danckwerts & Novotny (2007); Lesuffleur *et al.* (2006); Palomba & Novotny (2008)]. Owing to their dependence with the second or higher power of the field, nonlinear processes are preferentially sensitive to the most intense field bound to the metal. In particular, TPL scanning confocal microscopy has recently shown to be well suited to probe the local optical response of gold nanostructures [Beversluis *et al.* (2003); Bouhelier *et al.* (2005); Hohenau *et al.* (2006)].

Two-photon induced photoluminescence in gold is considered as a three-step process. Electrons from the d-band are first excited by two-photon absorption to the sp-conduction band, generating electronhole pairs. Then the intraband scattering processes move the electrons closer to the Fermi level. In a third step, the electronhole recombination occurs, either through non-radiative processes or by emission of luminescence [Mooradian (1969)].

TPL efficiency of gold is generally quite poor, but TPL signals from nanostructured gold can be strongly amplified by a resonant coupling with localized surface plasmons, as shown by Beermann & Bozhevolnyi (2005). Bouhelier *et al.* (2005) showed that in the case of small particles where the optical properties are dominated by LSP resonances, photoluminescence spectra feature a resonance at the same energy as extinction and scattering resonance suggesting that photoemission indeed relates to the particle plasmons.

1.3 Simulations tools: the Green dyadic method

The optical properties of a single metallic nanoparticle can be strongly modified when interacting electromagnetically with others. Both its spectroscopy and local field depend on the environment through the number of neighbors and their distribution [Bohren & Huffman (1983); Kreibig (1995)].

In order to foresee and to understand the behavior of coupled nanostructures both their far-field and near-field response are of interest. While far-field spectroscopy provides the resonance features of the system, by mapping the electric near-field intensity at the vicinity of the particles, one can assess the spatial distribution of the plasmon modes. In order to design structures with desired properties, extensive calculations have been performed. Both near- and far-field responses were calculated using the Green dyadic method (Appendix A). The theoretical results presented here were obtained using the codes developed by J.C. Weeber at the Université de Bourgogne in France [Girard *et al.* (1997)]. This formalism, which only requires the definition of the system geometry and its dielectric function provides a self-consistent resolution of Maxwell's equations accounting for the multipolar response of metallic nanoparticles and the presence of the substrate [Martin *et al.* (1995)]. The frequency-dependent complex permittivity of gold was taken from the experimental data of Palik (1985).

The chosen geometries consists of gold nanoparticles lying onto a glass substrate and illuminated by a polarized plane wave under an incidence angle Θ (figure 1.1). The inter-particle distance is set to 20 - 25 nm for chains and it is varied between 0 (contact) to 100 nm for dimers. These distances, that can be achieved with a good reproducibility experimentally, are short enough to assure a strong near-field coupling between neighbor particles through the overlapping of their evanescent fields. Here we focus on structures with resonances in the visible or near infra-red part of the spectrum, matching the wavelength range of our lasers(He-Ne or Ti-Saph).

The nanoparticles were defined as parallelepipeds or cylinders for the small gap cases, with 100 nm side basis and 20 nm height. Although approximative, this geometry has shown to be suitable to simulate the experimental near-field optical response of metal dots fabricated by e-beam lithography [Krenn *et al.* (1999b,c)].

1.3.1 Spectral properties

1.3.1.1 Dimers

To predict the response of gold dimers, we first computed the evolution of the scattering power spectra of a dimer. We focus our attention on the case where the incident electric field is polarized along the structure's main axis (Longitudinal polarization - LP). In this case, the dipolar resonance peak that dominates the spectrum of an isolated particle is strongly red-shifted with respect to the single-particle resonance from 720 to 810 nm (figure 1.2), this shift being larger for smaller separation distance.

Figures 1.2 (A) and 1.6 (A) shows the resonance of the dimer with a inter-particle distance of 20 and 30 nm respectively. In a first approximation, the behavior of the dimer resonance can be explained using a simple dipolar model based on the interaction of polarization charges formed at the particles surface. For LP, the increasing compensation of surface charges when the particles get closer induces weaker repulsion forces corresponding to higher resonance wavelengths. On the contrary, for an incident field orthogonal to the dimer axis, these forces tend to increase giving rise to a slight blue shift ([Kottmann & Martin (2001a); Rechberger *et al.* (2003)].

In the particular case when the two particles are touching, in addition to the dipolar resonance a second peak associated to a quadrupolar resonance appears in the region of interest (figure 1.6 (B)). This peak results from retardation effects in the touching dimers that acts as an effective bigger particle. This double

peak spectral feature can be used to increase the sensitivity of LSP bio-chemical sensors, as proposed previously in Enoch *et al.* (2004).

1.3.1.2 Finite chains of particles

A generalization of the previous study is the case of finite chain of particles. Their spectroscopy, for different number N of particles under both, normal incidence (NI) and total internal reflection (TIR) were studied. The results are plotted in figure 1.2.

Besides the observed shift in the dimer case ($N = 2$), a further shift occurs by adding a third particle together with the appearance of a quadrupolar like resonance that becomes significant for $N = 4$ and for $N = 5$ (interparticle separation 20 nm). We observe that under both NI ($\Theta = 0^o$) and TIR ($\Theta = 60^o$), for a small number of particles ($N \leq 5$), the spectra are dominated by the successive order of multipolar like modes resulting from the coupling of the LSP of the single particles (figure 1.2 (A and C)).

For a better understanding of the far-field properties of the longer chains, the influence of the incidence angle Θ for a ten particle chain was calculated (figure 1.3). For Θ smaller than the critical angle for total reflection $\Theta_c = 41.8^o$ smooth spectra (figure 1.3 (A)) is observed. The sharp resonant features shown in figure 1.2 (D) only appear for $\Theta > \Theta_c$ when the forward scattering becomes in-plane (figure 1.3 (B)) and consequently contributes to the coupling with the next neighbor. The strength of the resonances increases with the incident angle before reaching a threshold for $\Theta = 70^o$. Despite the discrete character of the chain, the blue shift of both peaks when increasing the incidence angle and thus decreasing the in-plane incident wavelength $\lambda_{//}$ suggests some kind of cavity mode. This hypothesis is corroborated by the appearance of this regime from a minimum chain length. In the case of a large N, at normal incidence, the spectra get much broader with some weak, low quality factor resonances (figure 1.2(B)).

A different behavior is observed for a larger number of particles ($N \geq 10$) in TIR (figure 1.2 (D)). The chain spectrum is less sensitive to N and is characterized

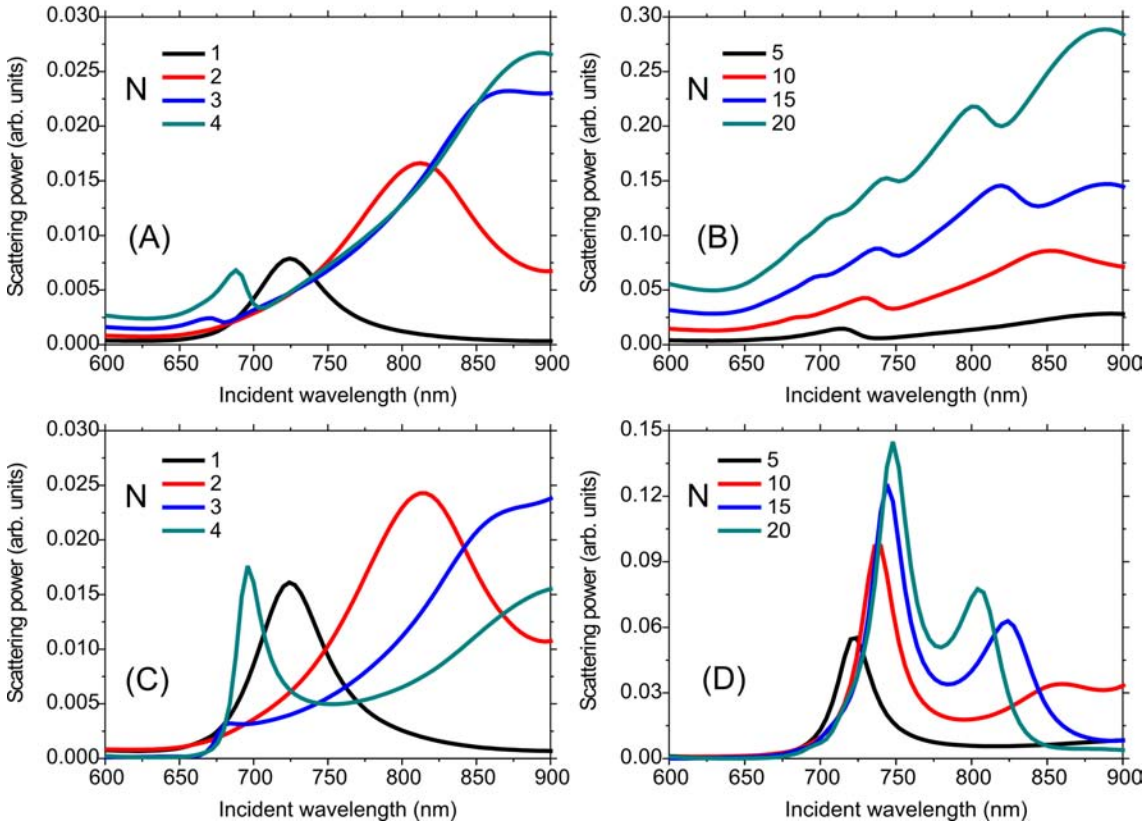

Figure 1.2: *Evolution of the scattering power spectrum of the chain as a function of the number N of gold particles for NI - $\Theta = 0^o$ (A-B) and TIR - $\Theta = 60^o$ (C-D). Longitudinal polarization, $d = 100$ nm, $\delta = 20$ nm).*

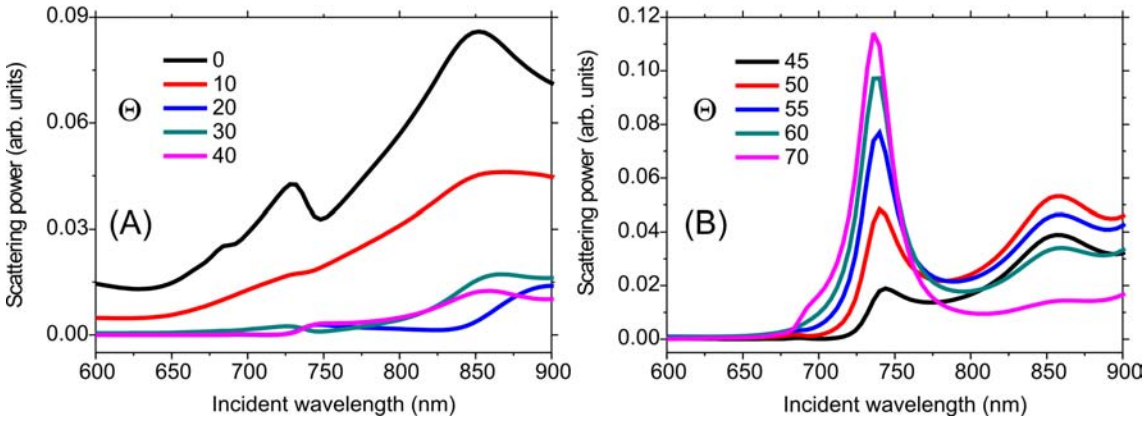

Figure 1.3: *Evolution of the scattering power spectrum of a 10 particles chain as a function of the incidence angle* Θ*. (A) the incidence angle is below the critical angle* $\Theta_c = 41.8^o$ *and (B) the incidence angle is above* Θ_c*.*

by the presence of two resonances. The main peak, at lower wavelength is slightly red-shifted when increasing the chain length whereas the secondary one displays the opposite tendency.

To get further insight into the origin of the double resonance it is interesting to monitor the position of the two main peaks when increasing the number of particles (figure 1.4). In the NI case (figure 1.4 (A)) a strong red-shift of the peaks is observed, followed by a saturation of the main peak around 850-900 nm when $N \geq 5$. The TIR case is drastically different. When N is increased the peak's separation becomes smaller and the length of the chain plays a critical role in the resonance position. Interestingly, the resonances are organized into well defined continuous dispersion lines(figure 1.4 (B)).

This resonant behavior is observed even for a much larger number of particles (figure 1.5 (A)). When $N \geq 25$ the second peak gets closer to the main one and a third peak appears in the near-infrared part of the spectrum. At $N = 40$ the first two peaks merge and the third one migrates towards the blue for $N = 50$ and 60. For larger N, the first peak is getting stronger, narrower and fixed at $\lambda = 752$ nm and the new one emerging being weaker. We believe that for these parameters,

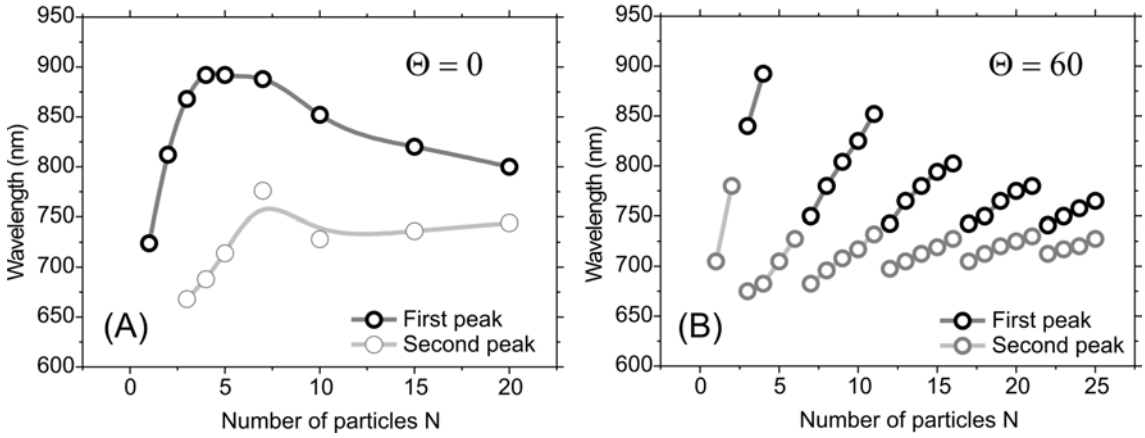

Figure 1.4: *Evolution of the resonance peaks of the scattering power spectrum of the chains as a function of the number N of gold particles for (A) $\Theta = 0^o$ and (B) $\Theta = 60^o$ (the solid lines are just a guide to the eye).*

in the limit of $N \geq 100$ the spectra of our chains will be dominated by a sole narrow resonance peak defined by the effective wavelength of the supported SP. It is interesting to mention that the all above resonances are contained within the same envelope centered around 750 nm which describes the resonance of individual particles.

A possible interpretation for this behavior is to consider that the chain behaves as a continuous wire of effective dielectric function ϵ_{eff} ($\epsilon_{Air} < \epsilon_{eff} < \epsilon_{Gold}$) along which a cavity-like resonance builds up. This would explain why a finite length is necessary to observe the discrete modes. In this way, the ϵ_{eff}, the effective length L_{eff} of the cavity together with the response of the individual particle determines the cavity modes.

For a more realistic comparison with experiments, is important in practice to account for the unavoidable size distribution caused by the fabrication process. To address this aspect, calculations for an imperfect chain with were performed, including randomly distributed defect particles with a size deviation of 10 % and interparticle separation of 25 nm, particle diameter of 90 nm and 15 nm height (single particle resonance around 720 nm). These assumptions relates with the

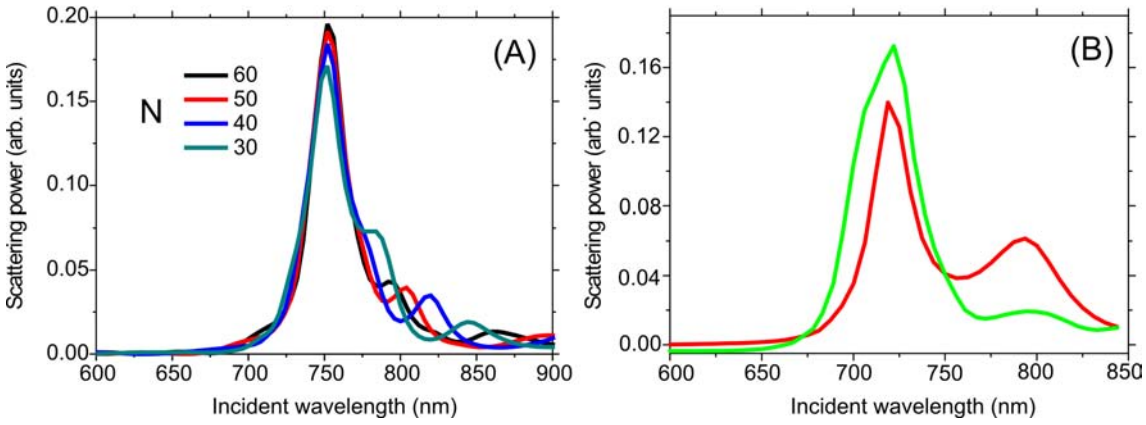

Figure 1.5: *(A) Evolution of the scattering power spectrum of the chains for a large number N of gold particles when $\Theta = 60^o$, longitudinal polarization. (B) Corresponding scattering power spectra spectrum of a 15 particles chain. Green curve corresponds to an imperfect chain including some geometrical defects.*

SEM analysis on the fabricated chains. In figure 1.5 (B) where the resonance of perfect and modified 15 particles chains are compared, we observe a broadening of the resonance peaks together with a significant decrease in intensity of the second peak. A significant impact of this effect on the experimental spectroscopic data can be foreseen, specially when measuring over a large number of chains.

1.3.2 Near-field distribution and field enhancement

Besides the far-field analysis of the structures shown above, the corresponding near-field optical distribution can be calculated. In this way one can get further insight in the underlying physics associated with every specific mode. In all the following, a field normalization has been performed with the incident field intensity at the same position in the absence of any gold structure providing the electric field intensity enhancement factor Γ produced by the structures.

Figure 1.6 (C-D) and figure 1.7 (A) shows the distribution of the electric field intensity, computed 20 nm above a 30 nm gap dimer and contact dimer $\delta = 0$, for NI and a longitudinal polarization, at their respective main resonance. For

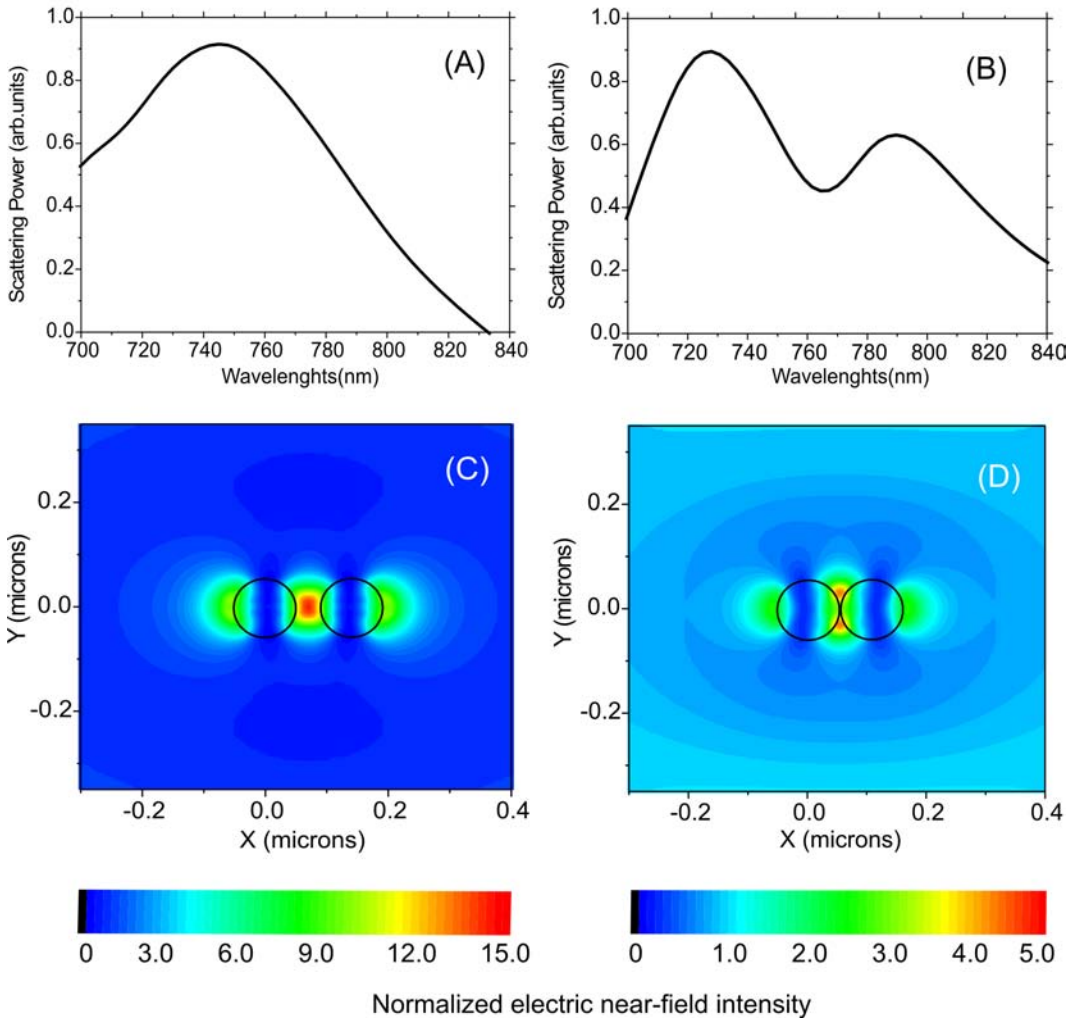

Figure 1.6: *Scattering power spectrum of a dimer with a 30 nm gap (A) and touching dimer (B) for a longitudinal polarization and* $\Theta = 0^o$. *(C-D) Electric near-field distribution calculated 20 nm above the respective structures in the same conditions at their respective main resonances. The contours give the particle location and size.*

the 30 nm gap dimer, a strong field in the gap with a intensity enhancement value of around 15 is observed at resonance (740 nm). In the contact case, at the quadrupolar resonance, two hot spots can be observed around the contact region with a $\Gamma \sim 5$. In both cases the fields are confined in volumes well below the diffraction limit, reaching a confinement level down to λ /15, FWHM for the contact case.

Figure 1.7 (B) shows the full near-field map of the electric field intensity, computed 20 nm above the 40 particle chain, in TIR case, for $\Theta = 60^o$ at its main resonance, $\lambda = 752$ nm. For the considered height at the chain extremity, the spot size is estimated at less than one fifth of the incident wavelength (λ /5 at FWHM or $1/e^2$ along X or Y). As expected, the highest field intensity enhancement is found at half-height of the chain in front of the last particle.

Figure 1.8 depicts the electric field intensity profile computed in the same conditions as above, for the 40 particle chain at $Y = 0$ for both $\Theta = 0^o$ and $\Theta = 60^o$, at their respective main resonance. Under normal incidence, the electric near-field extends symmetrically over the whole chain with a maximum of 2.7 at both extremities. These maxima results from the sudden jump in the dielectric function. Illumination under total reflection dramatically increases the asymmetry of the field profile. In this resonant regime, the field intensity increase from the first particle to the last one. The maximum value localized at the left extremity corresponds to a dramatic field enhancement with regards to the incidence (i.e. a gain of about 150 times compared to $\Theta = 0$). The fact that the periodicity of the oscillation does not fully match the pitch of the chain together with the overall modulation confirms the cavity mode type of the resonance mentioned above. We have additionally observed that for an incident wavelength corresponding to the secondary resonance, the field intensity is lower and displays a different distribution (inset of figure 1.8).

The surface plasmon wavelengths λ_{eff} can be computed as 2 times the observed modulation pitch of the field intensity along the structure, as described by Laroche & Girard (2006) and Ditlbacher *et al.* (2005). In the case of the 40

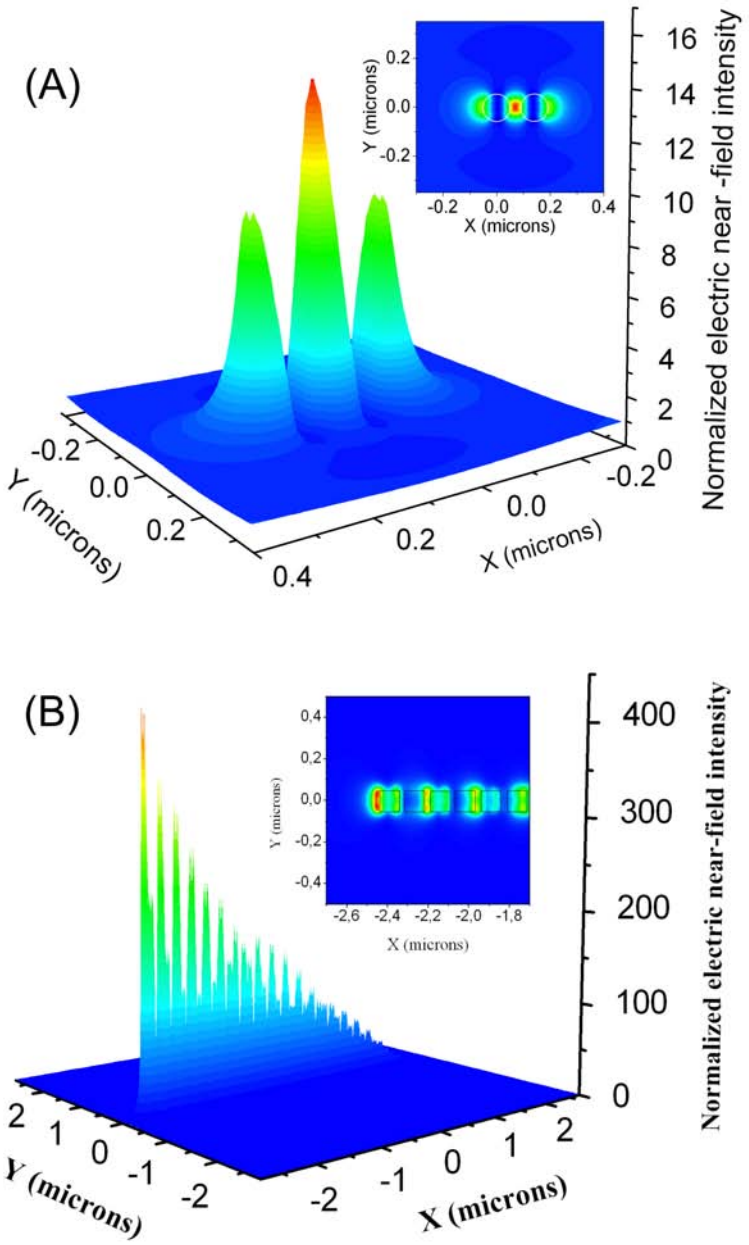

Figure 1.7: *3D Near-field intensity maps associated with a dimer with 30 nm gap (A) and a chain of 40 particles (B). Inset: (A)The projection of the field of the dimer and (B) the projection of the field for the last 6 particles of the chain. The contours give the particle location and size.*

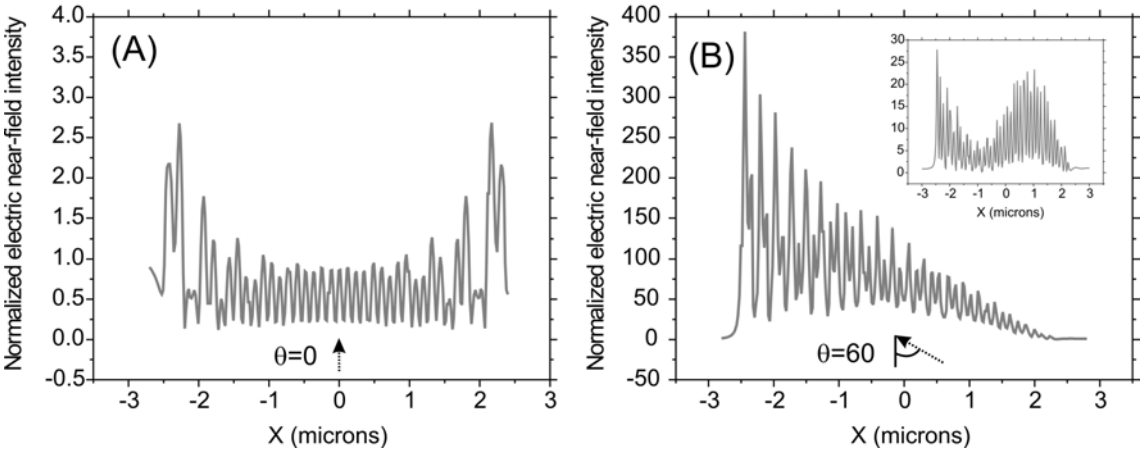

Figure 1.8: *Electric near-field intensity profiles (Y = 0) calculated 20 nm above a 40 particle chain for (A) Θ = 0 (λ = 880 nm) and (B) Θ = 60 (λ = 752 and 816 nm - inset)*

particles chain (4.78 μm long) a λ_{eff} of 558 nm was found for an incidence angle of 60 degrees. This values are shorter than the exciting light wavelength of 752 nm. This difference indicates that the surface plasmon mode can not directly couple to far field light.

The ability of the chain to accumulate light at their extremity originates from each of the particles of the chain that acts as a very efficient scattering center of the incident evanescent field, when the incident wavelength is matching their resonance. Due to the strong coupling between the particles, part of its energy is transferred to its closer neighbors. Each of the particles thus sees a field which is the sum of the incident field and the scattering from its nearest-neighbors. In the particular case of an incidence under total internal reflection and for the incident in-plane k-vector aligned along the chain axis, the resulting in-plane forward scattering of the particles considerably increases the coupling and it creates a cumulative field increase along the chain that gives rise to an intense field at its extremity.

For the TIR case the evolution of the enhancement factor with the number N of particles follows a linear increase for $N \geq 3$ before reaching an asymptotic

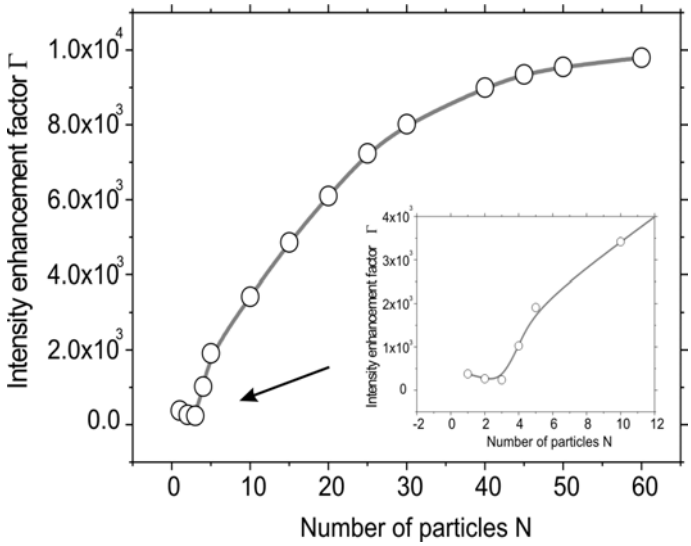

Figure 1.9: *Evolution of the enhancement factor* Γ *with the number* N *of particles. The enhancement was calculated 20 nm above the particle chain for the incidence angle* $\Theta = 60$*. Inset: a zoom of the low* N *region (the solid line is just a guide to the eye).*

value $\Gamma = 10^4$ for $N \geq 40$ (figure 1.9). Absorption losses are probably responsible for the saturation regime observed in both cases: $N \geq 40$ and $\Theta \geq 70$ degrees (figures 1.9 and 1.10). These maximum values are much higher compared to a single particle ($\Gamma = 300$) and commensurable with what has been reported with dimers displaying a nanometer separation distance [Hao *et al.* (2004); Kottmann & Martin (2001a); Xu & Käll (2002)].

The influence of the incidence angle Θ on the enhancement factor is represented in figure 1.10. For a 10 particle chain the incidence angle is changed from 0 to 90 degrees. A high increase of the Γ factor when the incidence angle exceeds the critical value is clearly evidenced.

In order to discard any edge or lighting-rod effects, the de-tuning method, described by Kottmann *et al.* (2000) has been applied. For an illumination wavelength shifted by 30 nm from the central peak, the field localization at the chain extremity is still observed, but corresponds to a much smaller Γ (reduction factor

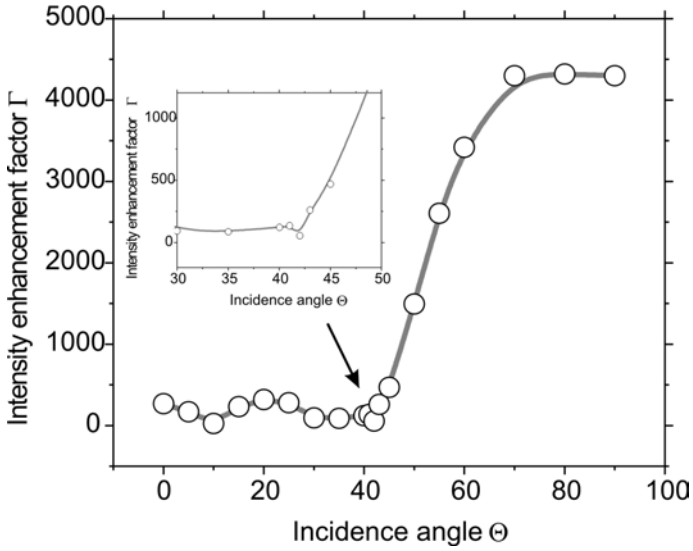

Figure 1.10: *Evolution of the enhancement factor* Γ *of a 10 particles chain as a function of the incidence angle* Θ*. The enhancement was calculated 20 nm above the particle chain. Inset: Zoom of the* Γ *evolution around the critical angle* $\Theta_c = 41.8^o$ *value (the solid line is just a guide to the eye).*

of 40).

Figure 1.11 presents a systematic study of the electric near-field intensity distribution near a 15 particle chain. In figures 1.11 (A-B) the distribution of the electric near-field intensity computed 20 nm above the chain for both $\theta = 0^o$ and $\theta = 60^o$ at their respective main scattering resonances is shown. Again, the intensity increases from the first particle to the last one leading to a high field intensity enhancement at the extremity. This value is more than 10 times larger than the maximum intensity observed under normal incidence.

The field map of the imperfect chains, described in the previous section was also calculated, and it is important to note that the output field enhancement is maintained significant with a reduction of only 15% (figure 1.11 (C)).

It is interesting to compare the finite chain geometry to a continuous gold wire with the same section and length. Similar to a chain, calculations for a wire display sharper resonances under TIR illumination compared to normal incidence.

However, no significant field enhancement occurs for these resonances (figure 1.11 (D)), indicating again that the particle forward scattering is at the origin of the high field enhancement at the chain extremity.

For the study of intrinsic properties of the chains, independently of the illumination and the detection conditions, the local density of electromagnetic states (ELDOS) above the gold particles is computed according to Chicanne *et al.* (2002). Figure 1.11 (E) shows the evolution with the incident wavelength of the ELDOS distribution computed 100 nm above a 15 particle chain. Far away from the scattering resonances presented in figure 1.5 (B), at 633 nm, the chain behaves like a discrete object where each of the particles acts individually. Inversely, a clear modulation is observed at $\lambda = 720$ nm corresponding to the main resonance. Its period of about 280 nm, different from the chain's pitch (115 nm) shows that the chain behaves like a linear cavity where resonances build up from the constructive interference of counter-propagating fields. This hypothesis is confirmed by the lower order resonance (period of 400 nm) observed when switching the incidence to the secondary resonance ($\lambda = 790$ nm).

On the basis of these results, a full interpretation of the optical properties of finite plasmonic chains can be provided. Although the system is discrete, light travels by tunneling through the interparticle gap spaces and a stationary wave from the interference of incident and reflected light is formed. For a suitable ratio between the effective wavelength and the chain length, a cavity resonance is built up. Its efficiency is mainly governed by the near-field coupling between particles and therefore by the gap distance.

To conclude this section, the optical properties of dimers and finite chains of closely packed gold nano-particles illuminated by a plane wave under normal and total internal reflection incidence was investigated numerically. We have first studied the case of dimers, where a subwavelength confinement of the field can be achieved within their gap. For the chains, the results show that the in-plane forward scattering of the particles contributes to strengthening their coupling, leading to sharp resonances in their scattered light. These resonances

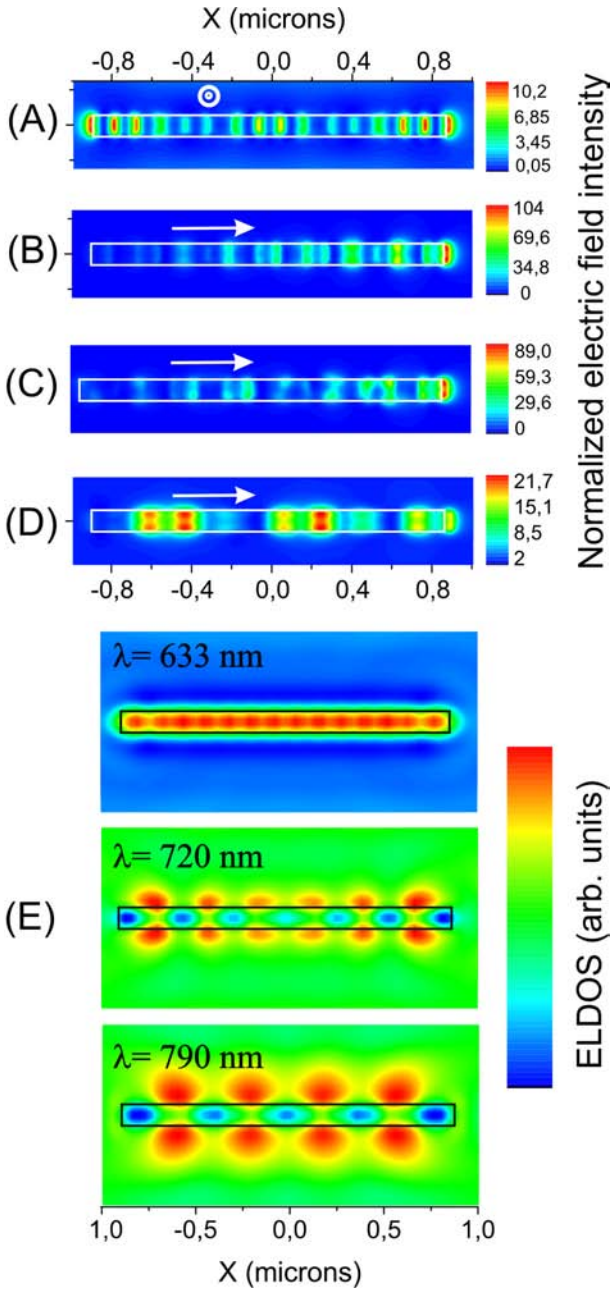

Figure 1.11: *Electric near-field distribution calculated 20 nm above a* 15 *particle chain* ($d = 90$ *nm*, $\delta = 25$ *nm*) *for (A)* $\theta = 0^o$ *at* $\lambda = 790$ *nm, (B)* $\theta = 60^o$ *at* $\lambda = 720$ *nm, (C)* $\theta = 60^o$ *at* $\lambda = 720$ *nm for the imperfect chain considered in figure 1.5 (B) and (D) above a continuous gold wire of the same length and section for* $\theta = 60^o$ *at* $\lambda = 810$ *nm. The arrows indicate the incident k-vector direction. (E) Evolution with the incident wavelength of the ELDOS calculated 100 nm above a 15 particle chain. The rectangle gives the chain and wire location*

attributed to a cavity-like mode correspond in the near-field zone to an intense and localized *hot-spot* at the chain extremity. The robustness of this effect has been demonstrated by simulations accounting for a significant level of defects .

1.4 Sample description

The fabrication of the plasmonic gold nanostructures, although critical, is now rendered more accessible by well established e-beam lithography processes (Appendix B).

Dimers: The particles have roughly a cylindrical shape with diameter of about 100 nm and 15 nm height. The pitch of the array, fixed at 400 nm has been chosen to maximize the signal from the ensemble without interfering significantly with the near-field coupling between the particles of each single dimer [Enoch *et al.* (2004); Gunnarsson *et al.* (2005)]. Several 50 μm $\times$50 μm matrices with different separation distances: $\delta = 0$ (contact) to 80 nm were fabricated (figure 1.12 (A) and (C)).

Chains: Each sample contains several periodic arrays (50 μm $\times$50 μm) of chains with different lengths, up to 25 particles. The gold particles forming the chains have roughly a cylindrical shape with an average diameter of 90 nm, 15 nm height and spaced by 25 nm (figure 1.12 (B) and (D)). The separation distance between two adjacent chains was fixed to 1 μm.

In practice, one has to face unavoidable size variations for structures with features smaller than 20 - 30 nm. In figure 1.13 we show the typical result of a lithographic process. SEM analysis enables to evaluate the size dispersion around the designed values (30 nm for the gap and 95 nm for the diameter). These variations are expected to have a significant influence on the spectra, as previously shown by our calculations (figure 1.5 (B)).

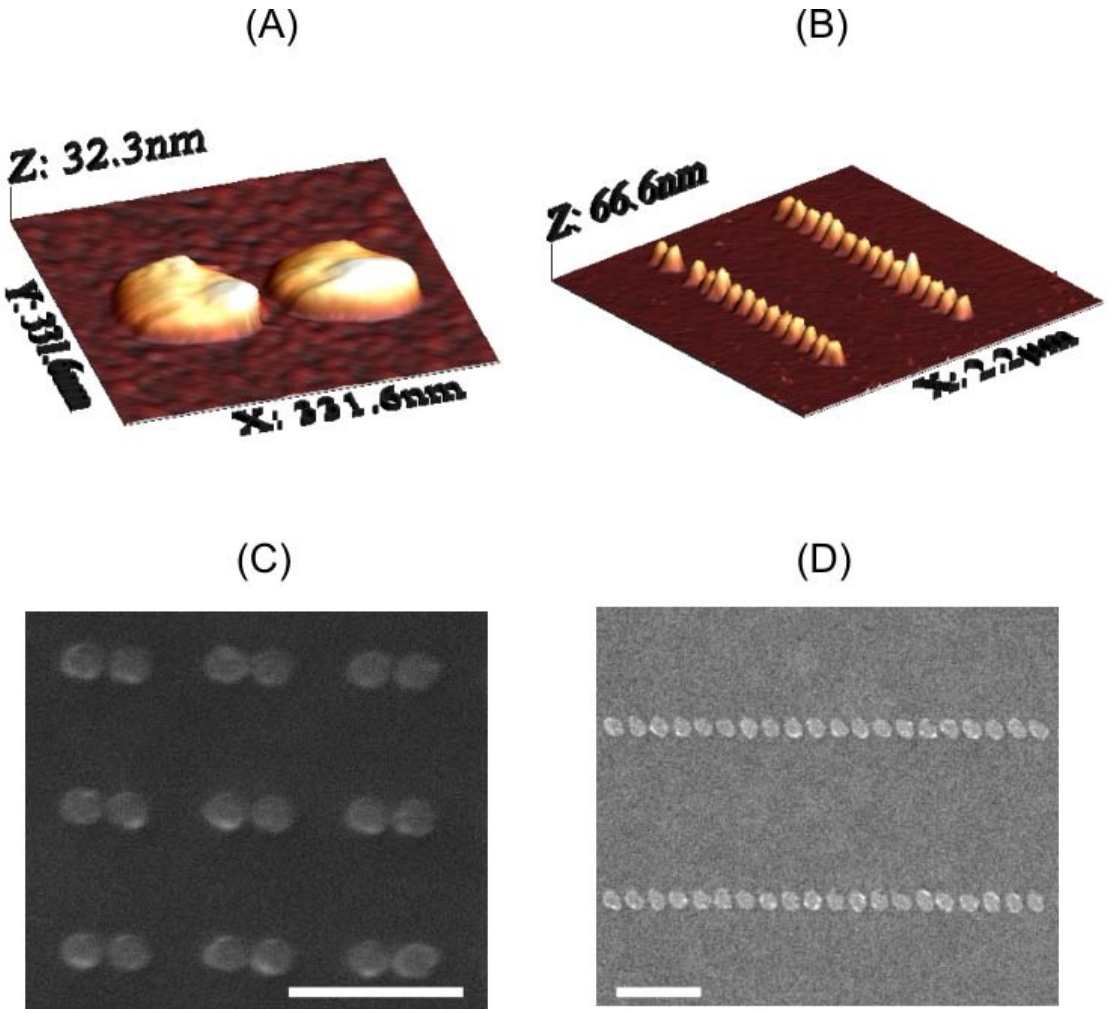

Figure 1.12: *Dimers and chains fabricated by e-beam lithography. (A-B) AFM images, (C-D) SEM images. Scale bars: 500 nm.*

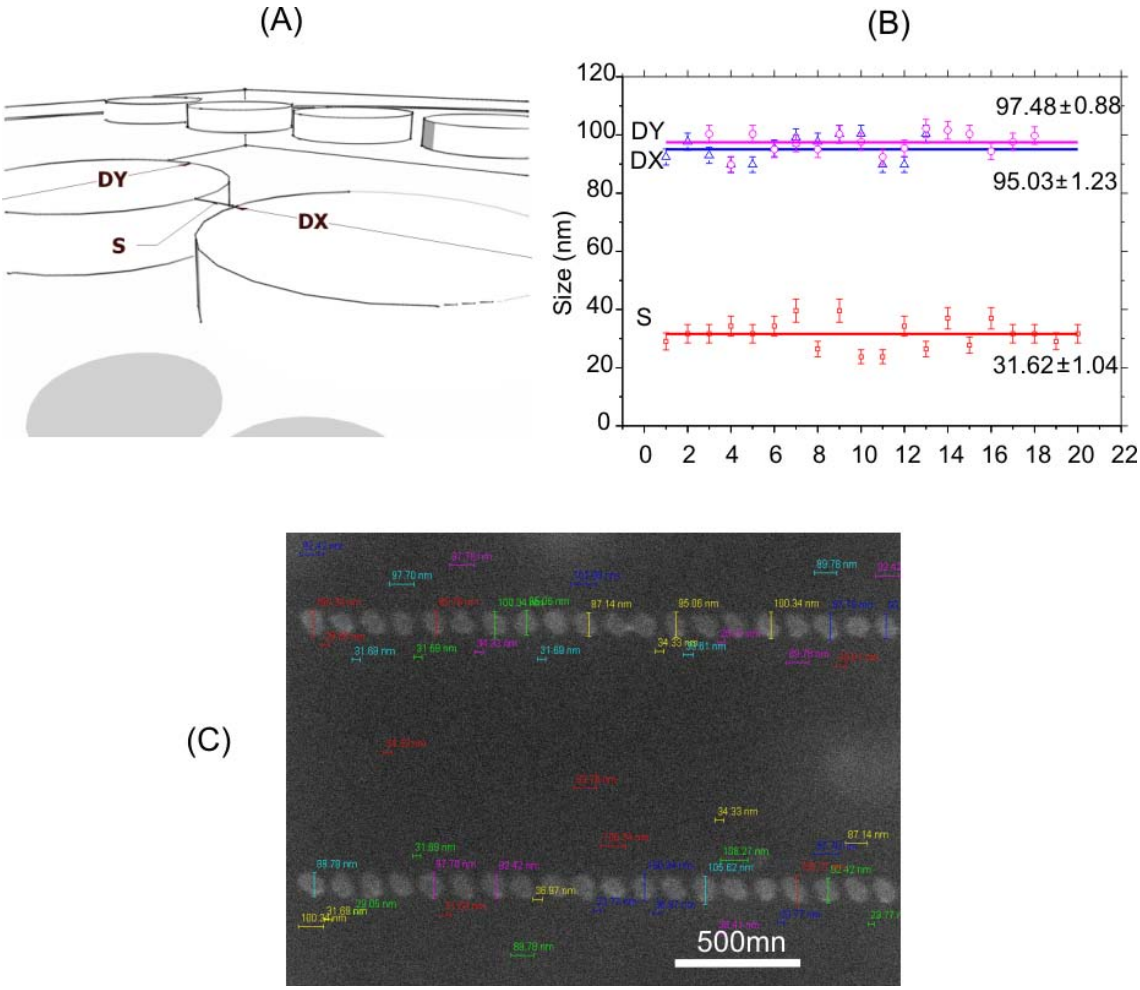

Figure 1.13: *Analysis of the size distribution of the fabricated chains: (A) chain geometrical configuration, (B) size distribution plot of particles diameter (DX and DY) and separation distance (S) and (C) SEM image of the 20 particles chains with measurements taken (Scale bar: 500 nm) .*

1.5 TPL spectroscopy

In this section the fabricated structures are characterized by both scattering and TPL spectroscopy. The specificities and the advantages of TPL signal in providing near-field spectral features not observed in the scattering spectra are discussed.

1.5.1 Dimers

In the previous sections, the important potential of these subwavelength structures have been presented. Here, the spectroscopic signature of dimers with different separation distances δ between the particles in a dimer is studied.

After fabricating the sample, their quality was first checked by recording their scattering spectra. In figure 1.14 (A) a typical resonance of a matrix of dimers with 50 nm gap in LP is presented. When δ is varied for both incident polarizations a tendency like the one shown in figure 1.14 (B) is observed. In agreement with our calculations and previous works, one can observe a red shift in the longitudinal polarization and a blue shift in the transverse one when decreasing δ [Rechberger *et al.* (2003)].

In the following, the region where the near field coupling dominates ($\delta = 0$ up to 40-50 nm) was studied. After this value the coupling decreased rapidly and the spectra becomes similar with the one of a single particle.

In order to measure the TPL response of the dimers, the sample was placed upside-down in the sample plane of an inverted laser scanning nonlinear microscope. The illumination was performed with a Kerr-lens mode-locked Ti:Sapphire laser which delivers 150 fs pulses at a repetition rate of 76 MHz. After attenuation with a tunable neutral density filter, the laser beam is sent to the sample surface through a microscope objective (20×, $NA = 0.45$) and scanned over the matrices (figure 1.15 (A)). The TPL spectra is obtained by tuning the laser stepwise throughout the wavelength range (700 - 900 nm). Constant power at the sample plane is ensured by adjusting the neutral density filter. For this measurements the average power entering the microscope was set to 25 mW. The corresponding

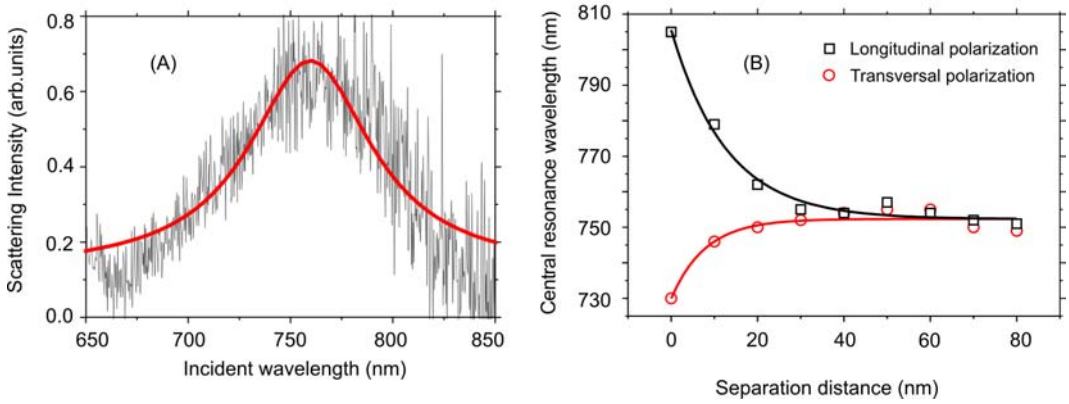

Figure 1.14: *Evolution of the extinction resonance wavelength with the separation distance δ. (A) Spectrum of a dimer with a 50 nm separation between the particles. The red curve is a Lorentz fit, (B) Evolution of the resonance wavelength with δ for longitudinal and transversal polarization. The solid lines are exponential fits of the points.*

intensity level is, in agreement with other works [Bouhelier *et al.* (2005)], below the threshold after which structural damage may occur. Linear spectroscopy performed before and after the TPL scan confirms that the structures were not structurally affected.

For each incident wavelength the signal emitted by the dimers is collected by the same microscope objective and optically filtered through a BG39 filter. Finally, the TPL is detected using a photomultiplier tube (Hamamatsu, H9305-04). By scanning the position of the incident beam a TPL image is recorded (figure 1.15 (B)). In post processing, the average of the signal is calculated both inside and outside the dimer matrix for background subtraction. The difference is called TPL signal in the following. In order to check the nature of this signal, we plotted its dependence with the incident laser power (see figure 1.16). The quadratic behavior (slope 2.1) shows that the considered signal mainly results from a two-photon absorption process.

Figure 1.17 (A) shows the TPL and scattering spectra under longitudinal

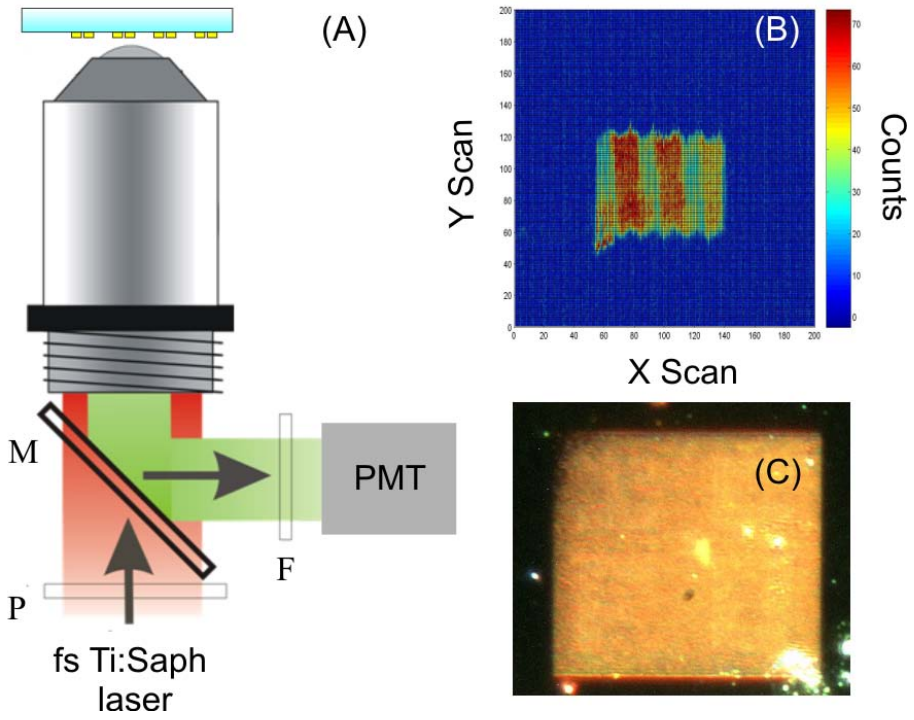

Figure 1.15: *Schematic representation of the experimental setup and the recorded images. (A) The set-up. (B) TPL scan image of a 50 by 50 micron square matrix. (C) Dark field image of the same type of matrix.*

polarization for dimers designed to have 30 nm separation distance. The TPL signal displays a clear resonance, similar to the scattering one. For the same incident power, the TPL signal in transversal polarization is indistinguishable from the noise-level confirming our measurement is mainly sensitive to the intense local field in the gap between the two particles.

The highest local field enhancement is expected for gap distances $\delta < 20$ nm [Schuck *et al.* (2005)]. This is proved by the TPL measurements performed with the same incident power. Only for small gaps dimers, the stronger local fields seem to cause structural modification to the particles. The resonance peaks recorded after the scan are blue shifted compared to the initial scattering spectra. Additional TPL measurements after the entire wavelength scan indicate that the change occurred at the beginning of the measurement sequence. This was con-

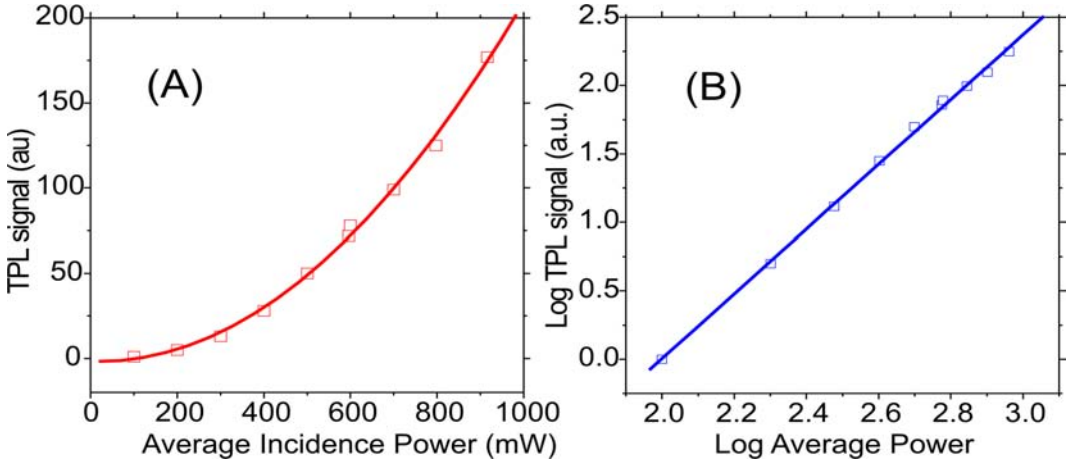

Figure 1.16: *Power dependence of the TPL signal. Quadratic fit (A) and linear fit in log log plot (B) with a 2.1 slope*

firmed by a new set of scattering measurements that give a similar resonance wavelength. Because the resonances are blue shifted under longitudinal polarization, we can assume that the particles did not fuse together. This is corroborated by SEM imaging that shows that after the TPL measurement, each particle was reduced in diameter to approximatively 90 nm and may thus get higher.

In the particular case of touching particles, a clear double peak resonance that does not appear in the scattering data is observed (figure 1.17 (B)). This behavior is quite similar to what is predicted by our simulations (figure 1.6 (B)) and prior works [Enoch *et al.* (2004); Kottmann & Martin (2001b)]. Here, a first indication that the TPL information may help to better predict and understand the optical response of small amounts of matter located at their vicinity. Indeed, an object located around the dimers would not see a maximum local intensity at 750 nm as expected from scattering measurements.

1.5.2 Finite chains of particles

In order to mach the illumination conditions simulated in the previous sections, a modification of the set-up was done to measure the finite chains of particles, as

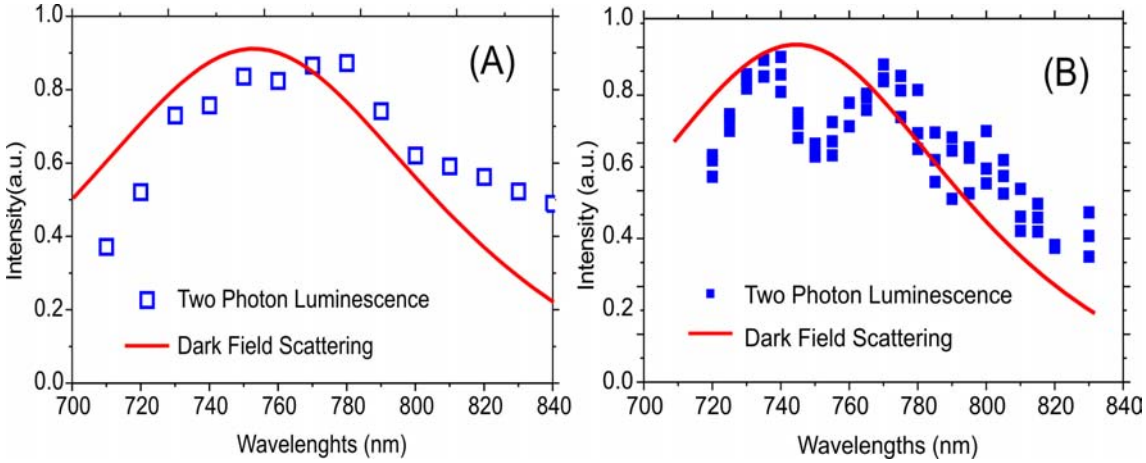

Figure 1.17: *Comparison of TPL and far-field spectrum for dimers with : (A) $\delta = 30$ nm and (B) touching dimers ($\delta = 0$ nm) under longitudinal polarization.*

sketched in figure 1.18. In this case, the fabricated sample is optically connected to a hemicylindrical glass prism by index-matching oil. The illumination can be independently performed with CW white light or a femtosecond laser beam to assess both the scattering and TPL spectra.

For the scattering measurements, the sample is illuminated under an incident angle θ by a linearly polarized and collimated white light beam generated by a 150 Watt quartz-halogen lamp. The light from the chains is collected by a $\times 40$, $NA = 0.65$ objective lens in the direction perpendicular to the sample surface and sent to a spectrometer. In order to measure the TPL response of the chains, the white light illumination is replaced by a Kerr-lens mode-locked Ti:Sapphire laser. To increase the signal to noise ratio, here a chopper with a lock-in amplifier (Stanford Research) was used to modulate the incident laser light and demodulate the signal. For the chains, an even stronger local field compared to the dimer case is expected . For this reason the incident power level is decreased to 15 mW by adjusting the neutral density filter at the prism entrance.

Figure 1.19 (A-B) shows the scattering spectrum of chains ($N = 15$) measured under longitudinal polarization for both $\theta = 0^o$ and $\theta = 60^o$. In agreement with the simulations of figure 1.19 (C-D), a broad scattering band is observed

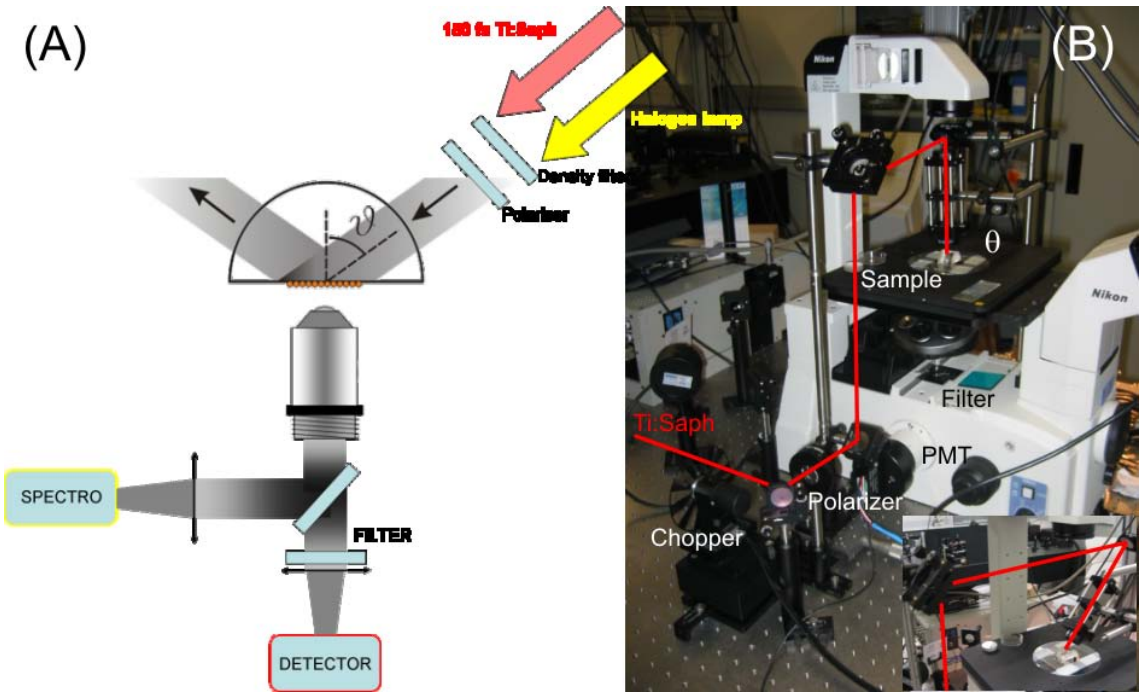

Figure 1.18: *Schematic representation of the experimental setup used to measure either the scattering or the TPL spectroscopy of the fabricated chains.*

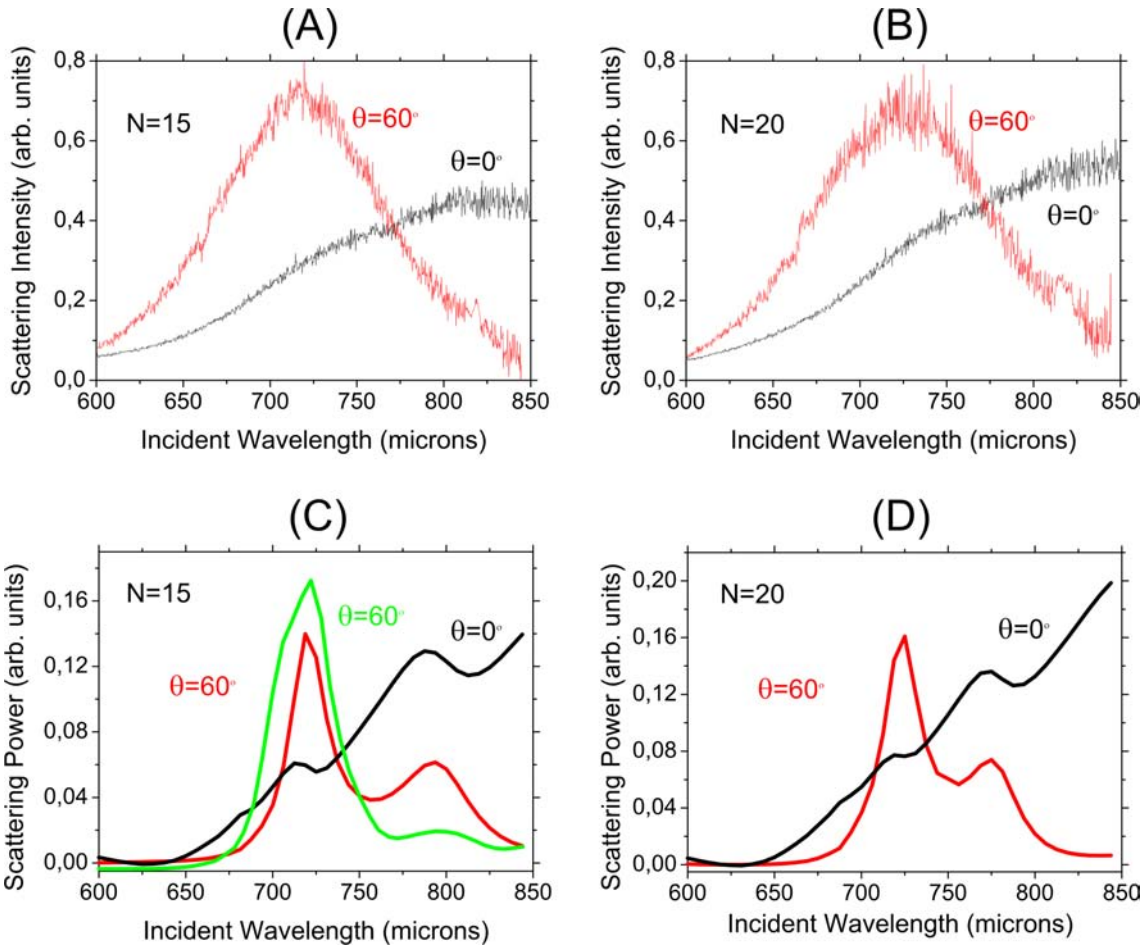

Figure 1.19: *Experimental scattering intensity spectra for (A) $N = 15$ and (B) $N = 20$ under $\theta = 60^o$ (grey) and $\theta = 0^o$ (black) and longitudinal polarization. (C-D) Corresponding calculated scattering power spectra (particle dimensions: 90 nm, 15 nm height, and spaced by 25 nm). The green curve corresponds to an imperfect chain including some geometrical defects.*

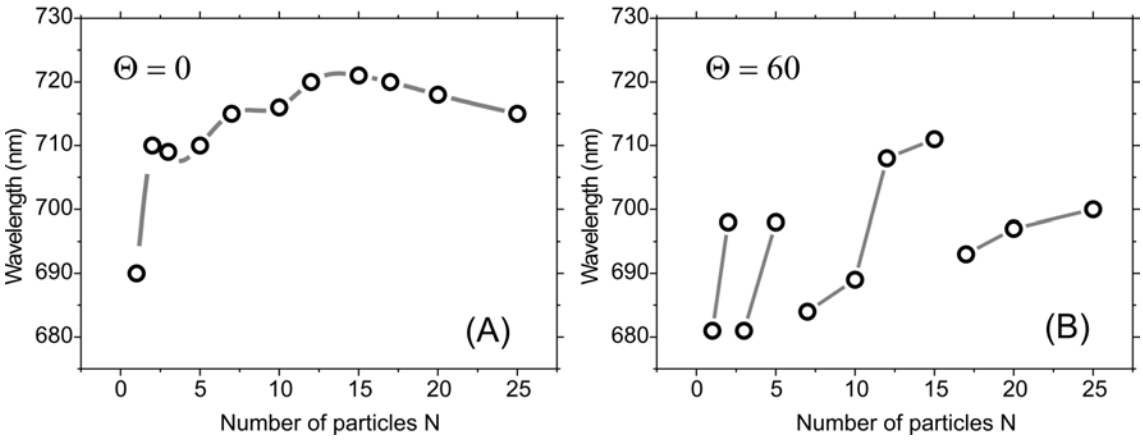

Figure 1.20: *Evolution of the measured resonance peaks of the scattering power spectrum of the chains as a function of the number N of gold particles for* $\Theta = 0^o$ *(A) and* $\Theta = 60^o$ *(B)(the solid lines are just a guide to the eye).*

under normal incidence. A sharper peak centered around 718 nm is measured for $\theta = 60^o$. Its central wavelength gets slightly red-shifted to 730 nm when increasing the chain length from 15 to 20 particles. Since this resonance occurs for a similar wavelength than the dipolar resonance of a single particle (around 720 nm), a conventional near-field coupling (where the peak would be strongly red-shifted) is excluded. These observations tend to corroborate the existence of resonant modes predicted by the theory, although the double peak features are not resolved by the scattering measurements.

Figure 1.20 shows the evolution of the measured peak resonance of the chains as a function of the number of particles. Even if the spectra do not show all the predicted characteristics, the peaks arrangement looks very similar with the predicted diagram (figure 1.4), for both normal and TIR incidence, confirming the important role of the chain's length.

The fact that the double peak is not resolved in the scattering experiment is mainly attributed to the significant background induced both by the detection process and the sample irregularity (see figure 1.5 (B) and 1.13). For the latest contribution, any defect in the particle shape and dimensions adds a parasitic

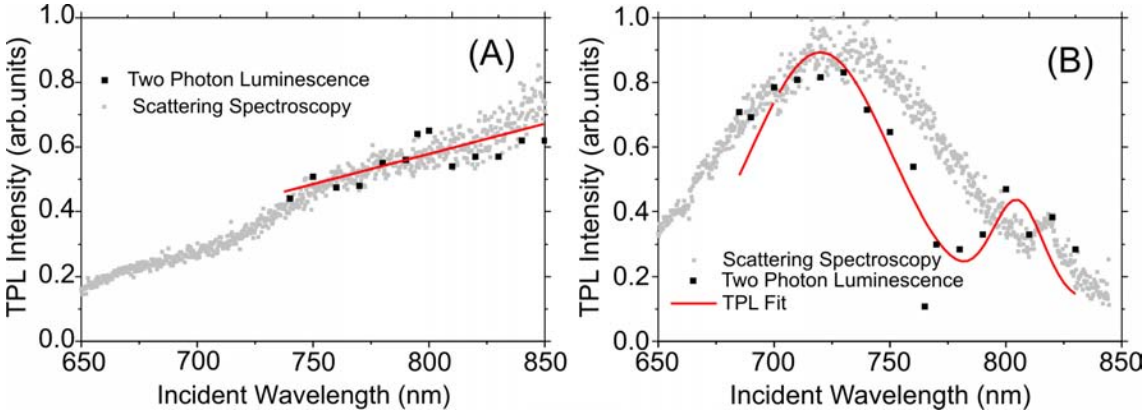

Figure 1.21: *Comparison of TPL (black squares) and far-field spectrum (gray squares) for 25 particle chains when : (A)* $\Theta = 0^o$ *and (B)* $\Theta = 60^o$ *under longitudinal polarization. The TPL data are fitted with a linear and a two peaks Lorentzian model respectively (red curves).*

background to the signal associated to the resonant modes of the chains. As described above, this is supported by the simulation of figure 1.18 (C) (green line) performed for an imperfect chain. Although this simple calculation cannot account for the actual degree of imperfections in the fabricated samples, it illustrates the resulting broadening of the resonance peaks in the scattering spectrum.

The TPL measurements were initiated with 25 particles chains. In figure 1.21 the overlap between the scattering spectra and the TPL one in both illumination conditions is presented. For the normal incidence one does not expect any resonance in the considered range of wavelengths. Both scattering and TPL spectra show a monotonous evolution. Conversely for $\theta = 60^o$ like with the contact dimer case, the TPL intensity spectra clearly provides further information over scattering. The two peaks predicted by the simulations can be resolved.

The results for differents number of particles ($N = 15$ and $N = 20$), under TIR illumination ($\theta = 60^o$) are shown in figure 1.22. Here, to be sure of the reproducibility of the acquired data and rule out any structural modification of the chains induced by the laser illumination [Bouhelier (2006)], each point of the curves corresponds to an average over two back and forth scans of the

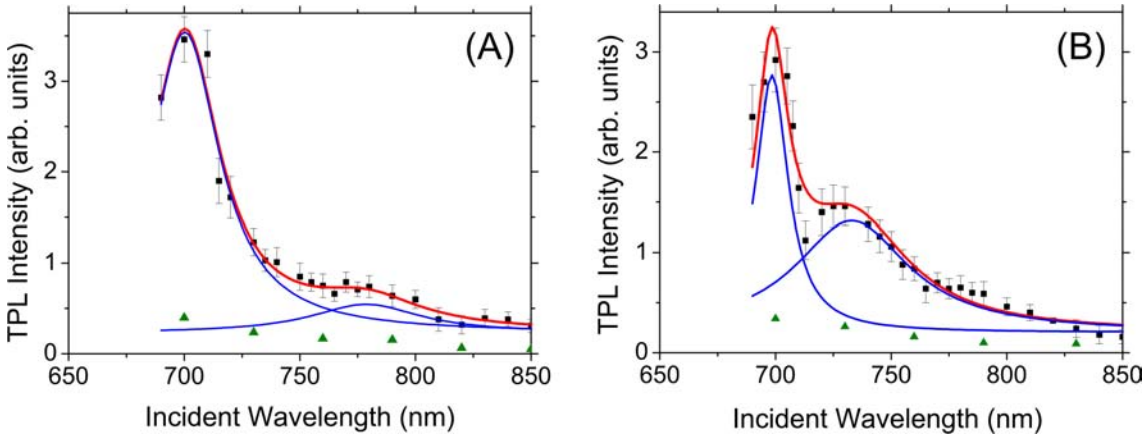

Figure 1.22: *Evolution of the TPL intensity with the incident wavelength for (A) $N = 15$ and (B) $N = 20$ both under longitudinal (squares) and transversal (triangles) polarizations. Data points for longitudinal polarization are fitted (red line) with a two peaks Lorentzian model.*

laser wavelength. Again, unlike the experimental scattering curves, the TPL displays a double peak response for both structures as predicted in figure 1.18 (C-D). While the small red-shift of the main resonance is not resolved, one can observe the strong blue shift of the secondary peak. Further discrepancies on the peaks position are attributed to the structural differences of the fabricated chains compared to the ideal object considered in the simulation.

Measurements were repeated under transverse polarization (E-field perpendicular to the chain axis) to verify that the observed features unambiguously result from modes of the chains. In this case, the TPL intensity remains at a significantly lower value without any peaks showing up. Note nevertheless that from the theory a resonance is expected to occur at lower wavelengths (around 680 nm) due to the near-field coupling between the particles. This resonance is weaker compared to the longitudinal polarization and could not be extracted out from the noise level in the scattering experiments but it plausibly explains the slight increase of the TPL signal towards the shortest wavelengths.

By calculating the ratio between the maximum TPL intensity under the two

polarization states, the TPL intensity enhancement factor γ associated to the main resonances of figure 1.22 (A-B) can be assessed. A ratio $\gamma \sim 10$ for the two chain lengths is obtained. Although this value indicates higher local field values in the longitudinal polarization state where the cavity modes are expected, it does not permit to deduce the actual enhancement factor of the local field with regards to the incidence. Indeed, while the cavity modes under longitudinal polarization correspond to an intense and localized local field at the chain extremity, calculations indicates much weaker field values under transverse polarization but extended over the whole chain. Because the TPL intensity we measured is directly proportional to the fourth power of the field inside the gold integrated over the whole structure, the ratio underestimates the actual enhancement factor.

1.6 Conclusions

To summarize, in this chapter we have shown:

- Extensive calculations based on the Green dyadic method are able to predict the far- and near-field behavior of two different types of coupled nanostructures.

- In the dimer geometry, a high confinement of the field together with a distinct double-peak spectroscopic signature can be achieved.

- For the finite chains, the in-plane forward scattering of the particles contributes to strengthening their coupling, leading to sharp resonances in their scattered light when the chain is illuminated under TIR.

- Under specific conditions, an intense and localized hot-spot is generated at the chain extremity that may be of interest for applications like SERS spectroscopy or bio-sensing. Simulated structures having a realistic defect level, that may occur in the fabrication process still preserve the effects, thus confirming the robustness of such modes.

- To the best of our knowledge, the work we presented is the first experimental comparison between the linear far-field and local spectroscopy of these types of systems.

- The experimental results show that the TPL spectroscopy can provide over conventional scattering spectroscopy additional data on the electromagnetic modes of the nanostructures, being able to resolve the finest resonant features. In particular, multipolar like resonances and cavity mode resonances that cannot be observed in the scattering response are clearly resolved with TPL.

However, the measurement are taken over a large number of structures with a strong size dispersion. While we are able to use this technique to assess the resonant behavior of our structures, the peaks are still quite broad, limiting the spectral resolution of the method. This limitation is expected to be overcome by going towards TPL measurements on single structures. Beyond this, high resolution TPL measurements on isolated structures could bring further insights on the mode distribution and enable local spectroscopy on specific regions of the structure.

1. TPL MEASUREMENTS ON ENSEMBLES OF COUPLED METALLIC NANOPARTICLES

Chapter published as:

- **P. Ghenuche**, R. Quidant and G. Badenes, *Cumulative plasmon field enhancement in finite metal particle chains*, **Optics Letters 30**, 1882 (2005): Ghenuche *et al.* (2005)
- D. ten Bloemendal, **P. Ghenuche**, R. Quidant, G. I. Cormack, P. Loza-Alvarez and G. Badenes, *Local field spectroscopy of metal dimers by TPL microscopy*, **Plasmonics 1**, 41 (2006): ten Bloemendal *et al.* (2006)
- **P. Ghenuche**, I.G. Cormack, G. Badenes, P. Loza-Alvarez and R. Quidant, *Cavity resonances in finite plasmonic chains*, **Applied Physics Letters 90**, 041109 (2007): Ghenuche *et al.* (2007)

References

Beermann, J. & Bozhevolnyi, S.I. (2005). Two-photon luminescence microscopy of field enhancement at gold nanoparticles. *Phys. Stat. Sol. C*, **2**, 3983–3987. 4

Beversluis, M.R., Bouhelier, A. & Novotny, L. (2003). Continuum generation from single gold nanostructures through near-field mediated intraband transitions. *Phys. Rev. B*, **68**, 115433. 2, 4

Bohren, C. & Huffman, D. (1983). *Absorption and scattering of light by small particles*. New York: Wiley. 5

Bouhelier, A. (2006). Field-enhanced scanning near-field optical microscopy. *Microsc. Res. Tech.*, **69**, 563–579. 31

Bouhelier, A., Bachelot, R., Lerondel, G., Kostcheev, S., Royer, P. & Wiederrecht, G.P. (2005). Surface plasmon characteristics of tunable photoluminescence in single gold nanorods. *Phys. Rev. Lett.*, **95**, 267405. 4, 24

Chicanne, C., David, T., Quidant, R., Weeber, J.C., Lacroute, Y., Bourillot, E., Dereux, A., Francs, G.C.D. & Girard, C. (2002). Imaging the local density of states of optical corrals. *Phys. Rev. Lett.*, **88**, 097402. 18

Danckwerts, M. & Novotny, L. (2007). Optical frequency mixing at coupled gold nanoparticles. *Phys. Rev. Lett.*, **98**, 026104. 4

REFERENCES

Ditlbacher, H., Hohenau, A., Wagner, D., Kreibig, U., Rogers, M., Hofer, F., Aussenegg, F.R. & Krenn, J.R. (2005). Silver nanowires as surface plasmon resonators. *Phys. Rev. Lett.*, **95**, 257403. 13

Enoch, S., Quidant, R. & Badenes, G. (2004). Optical sensing based on plasmon coupling in nanoparticle arrays. *Opt. Express*, **12**, 3422. 7, 20, 26

Ghenuche, P., Quidant, R. & Badenes, G. (2005). Cumulative plasmon field enhancement in finite metal particle chains. *Opt. Lett.*, **30**, 1882–1884. 36

Ghenuche, P., Cormack, I.G., Badenes, G., Loza-Alvarez, P. & Quidant, R. (2007). Cavity resonances in finite plasmonic chains. *Appl. Phys. Lett.*, **90**, 041109. 36

Girard, C., Weeber, J.C., Dereux, A., Martin, O.J.F. & Goudonnet, J.P. (1997). Optical magnetic near-field intensities around nanometer-scale surface structures. *Phys. Rev. B*, **55**, 16487–16497. 5

Gunnarsson, L., Rindzevicius, T., Prikulis, J., Kasemo, B., Kall, M., Zou, S. & Schatz, G. (2005). Confined plasmons in nanofabricated single silver particle pairs: Experimental observations of strong interparticle interactions. *J. Phys. Chem. B*, **109**, 1079–1087. 20

Hao, E., Schatz, G.C. & Hupp, J.T. (2004). Synthesis and optical properties of anisotropic metal nanoparticles. *J. Fluoresc.*, **14**, 331–341. 16

Hillenbrand, R., Keilmann, F., Hanarp, P., Sutherland, D.S. & Aizpurua, J. (2003). Coherent imaging of nanoscale plasmon patterns with a carbon nanotube optical probe. *Appl. Phys. Lett.*, **83**, 368–370. 2

Hohenau, A., Krenn, J.R., Beermann, J., Bozhevolnyi, S.I., Rodrigo, S.G., Martin-Moreno, L. & Garcia-Vidal, F. (2006). Spectroscopy and nonlinear microscopy of au nanoparticle arrays: Experiment and theory. *Phys. Rev. B*, **73**, 155404. 4

Kottmann, J. & Martin, O. (2001a). Plasmon resonant coupling in metallic nanowires. *Opt. Express*, **8**, 655–663. 2, 6, 16

Kottmann, J., Martin, O., Smith, D. & Schultz, S. (2000). Spectral response of plasmon resonant nanoparticleswith a non-regular shape. *Opt. Express*, **6**, 213–219. 16

Kottmann, J.P. & Martin, O.J.F. (2001b). Retardation-induced plasmon resonances in coupled nanoparticles. *Opt. Lett.*, **26**, 1096–1098. 26

Kreibig, M., Uwe; Vollmer (1995). *Optical Properties of Metal Clusters*. Springer-Verlag. 5

Krenn, J.R., Dereux, A., Weeber, J.C., Bourillot, E., Lacroute, Y., Goudonnet, J.P., Schider, G., Gotschy, W., Leitner, A., Aussenegg, F.R. & Girard, C. (1999a). Squeezing the optical near-field zone by plasmon coupling of metallic nanoparticles. *Phys. Rev. Lett.*, **82**, 2590–2593. 3

Krenn, J.R., Dereux, A., Weeber, J.C., Bourillot, E., Lacroute, Y., Goudonnet, J.P., Schider, G., Gotschy, W., Leitner, A., Aussenegg, F.R. & Girard, C. (1999b). Squeezing the optical near-field zone by plasmon coupling of metallic nanoparticles. *Phys. Rev. Lett.*, **82**, 2590–2593. 6

Krenn, J.R., Weeber, J.C., Dereux, A., Bourillot, E., Goudonnet, J.P., Schider, B., Leitner, A., Aussenegg, F.R. & Girard, C. (1999c). Direct observation of localized surface plasmon coupling. *Phys. Rev. B*, **60**, 5029–5033. 6

Laroche, T. & Girard, C. (2006). Near-field optical properties of single plasmonic nanowires. *Appl. Phys. Lett.*, **89**, 233119. 13

REFERENCES

Lereu, A.L., Sanchez-Mosteiro, G., Ghenuche, P., Quidant, R. & Hulst, N.F.V. (2008). Individual gold dimers investigated by far- and near-field imaging. *Journal of Microscopy*, **229**, 254–258. 2

Lesuffleur, A., Kumar, L.K.S. & Gordon, R. (2006). Enhanced second harmonic generation from nanoscale double-hole arrays in a gold film. *Appl. Phys. Lett.*, **88**, 261104. 4

Maier, S., Kik, P., Atwater, H., Meltzer, S., Harel, E. & B. Koel, A.R. (2003). Local detection of electromagnetic energy transport below the diffraction limit in metal nanoparticle plasmon waveguides. *Nat. Materi.*, **2**, 229 – 232. 3

Martin, O.J.F., Girard, C. & Dereux, A. (1995). Generalized field propagator for electromagnetic scattering and light confinement. *Phys. Rev. Lett.*, **74**, 526–529. 5

Messinger, B.J., von Raben, K.U., Chang, R.K. & Barber, P.W. (1981). Local fields at the surface of noble-metal microspheres. *Phys. Rev. B*, **24**, 649–657. 2

Mooradian, A. (1969). Photoluminescence of metals. *Phys. Rev. Lett.*, **22**, 185–187. 4

Palik, E., ed. (1985). *Handbook of Optical Constants of Solids*. Academic Press, New York. 5

Palomba, S. & Novotny, L. (2008). Nonlinear excitation of surface plasmon polaritons by four-wave mixing. *Phys. Rev. Lett.*, **101**, 056802. 4

Quinten, M., Leitner, A., Krenn, J.R. & Aussenegg, F.R. (1998). Electromagnetic energy transport via linear chains of silver nanoparticles. *Opt. Lett.*, **23**, 1331–1333. 3

Rechberger, W., Hohenau, A., Leitner, A., Krenn, J.R., Lamprecht, B. & Aussenegg, F.R. (2003). Optical properties of two interacting gold nanoparticles. *Opt. Comm.*, **220**, 137–141. 6, 23

Schuck, P.J., Fromm, D.P., Sundaramurthy, A., Kino, G.S. & Moerner, W.E. (2005). Improving the mismatch between light and nanoscale objects with gold bowtie nanoantennas. *Phys. Rev. Lett.*, **94**, 017402. 25

ten Bloemendal, D., Ghenuche, P., QuidantI, R., Cormack, G., Loza-Alvarez, P. & Badenes, G. (2006). Local field spectroscopy of metal dimers by tpl microscopy. *Plasmonics*, **1**, 41. 36

Xu, H. & Käll, M. (2002). Surface-plasmon-enhanced optical forces in silver nanoaggregates. *Phys. Rev. Lett.*, **89**, 246802. 16

Zhdanov, A., Kreuzer, M.P., Rao, S., Fedyanin, A., Ghenuche, P., Quidant, R. & Petrov, D. (2008). Detection of plasmon-enhanced luminescence fields from an optically manipulated pair of partially metal covered dielectric spheres. *Opt. Lett.*, **33**, 2749–2751. 2

Chapter 1

TPL measurements on single nanoantennas

1.1 Introduction

The use of two-photon induced luminescence as a non-invasive far field method to probe the local field around single nanostructures has attracted lately much attention. In particular, Muhlschlegel *et al.* (2005); Schuck *et al.* (2005) and Bouhelier *et al.* (2005) were able to use this technique to characterize the response of isolated gold antennas.

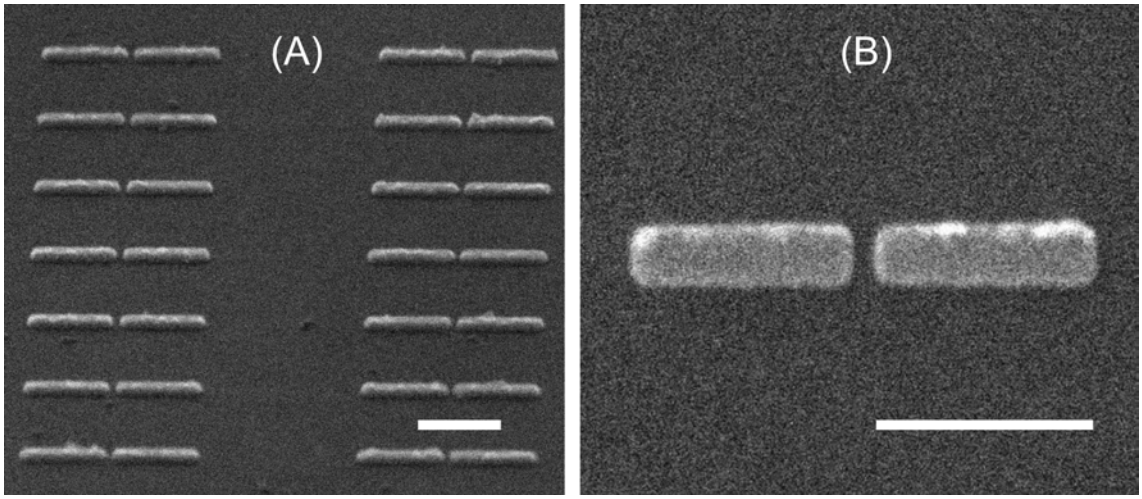

Figure 1.1: *SEM micro-graph of gold gap antennas fabricated by e-beam lithography (scale bar 500 nm). Each arm is 500 nm long, 100 nm wide and 40 nm high. (A) Ensemble of nanoantennas and (B) image of a single antenna*

In all these works the intensity of the overall TPL signal from the antenna has been studied as a function of the geometrical parameter (gap size, arm lengths), but the distribution of the field along single structures has not been yet resolved. This has prevented to draw what is the actual correlation between the distribution of the TPL signal and the mode distribution of the structures. In this chapter our goal is to monitor the TPL near single antennas and to compare it with 3D numerical calculations of the mode map.

In the previous chapter, the limitations of spectroscopic measurements averaged over a large number of structures have been described. As depicted in figure

1.1 (A) in practice, fabrication defects may be important when considering a large number of antennas. Measuring a single antenna as the one showed in figure 1.1 (B) will significantly reduce the importance of these defects and can offer the advantage of a narrower spectrum as well as important information about the mode distribution of the antenna, as shown in figure 1.2.

This chapter is organized as follows: The first subsection provides some general concepts about optical nano-antennas. Then the second subsection focuses on a detailed description of the new optical setup, including a study of its spacial resolution and the nature of the measured TPL signal.

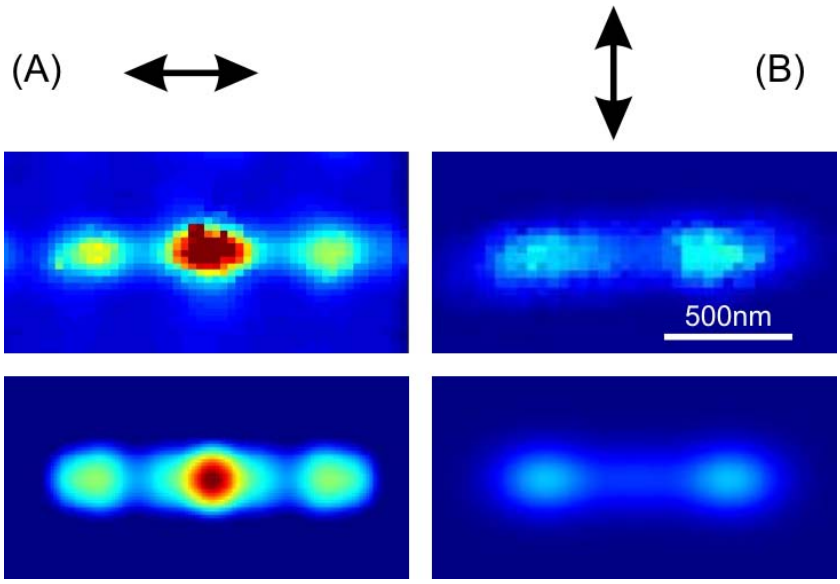

Figure 1.2: *TPL maps and simulated near field of a single gap antenna for longitudinal (A) and transversal (B) polarizations. (C-D) Corresponding distribution of the local field $|E|^4$ maps. The arrows depict the polarization directions.*

1.2 Optical Nanoantenna

Optical nano-antennas (ONA) are foreseen to be one of the most promising strategy to bridge the gap between diffraction limited (microscopic) light sources and the nanoscale. Because of the frequency invariance of Maxwell's equations, antenna concepts developed at radio-frequencies should be applicable to the optical regime. Independently of the technological challenges raised by their fabrication, this adaptation additionally requires dealing with metal absorption losses. Fortunately the antenna performance can be substantially enhanced by plasmon resonances that lead to strong local fields [Aizpurua *et al.* (2005); Lereu *et al.* (2008); Novotny (2007); Righini *et al.* (2009)]. Particularly, strong and confined fields can be generated within the dielectric subwavelength gap between two resonant metal wire antennas. The overall enhanced TPL intensity of such geometry was measured by Schuck *et al.* (2005) and Muhlschlegel *et al.* (2005).

At radio frequencies, the electromagnetic properties of metal nano-wires mainly obey geometrical considerations. For an incident field polarized along the wire long axis, standing waves (cavity like) resonances build up when its length L corresponds to a multiple of the effective wavelength λ_{eff} within the metal.

$$L = (n + \frac{1}{2})\lambda_{eff} \tag{1.1}$$

Unlike in the radiowave regime where λ_{eff} is very close from the wavelength in vacuum, in the specific case of real metals at optical frequencies, λ_{eff} corresponding to the wavelength of the SP propagating along the nanowires depends on the metal permittivity [Novotny (2007); Taminiau *et al.* (2007)] and the wire cross-section, as measured experimentally for gold and silver by Schider *et al.* (2003). With the aim of efficiently concentrating light fields to subwavelength volumes, several groups have recently investigated the configuration where two resonant adjacent metal nanowires form a subwavelength dielectric gap. Similarly to what occurs for dimers of spherical or cylindrical metal particles, the strong surface charge gradient in the gap leads to an intense and confined electromagnetic field.

This effect is expected to be strengthened at a wavelength where each of the arms of the dimer-antenna support a resonance described by equation (1.1) for which surface charges concentrate at the extremities.

Enhancement and confinement of optical field near ONA have direct implications in improving the interaction of light with subwavelength volume of matter down to the single molecule level. Muskens *et al.* (2007) reported on the enhancement of the quantum efficiency of single emitters coupled to ONA. When implemented at the extremity of an optical scanning probe, ONA can also be used to substantially improve optical addressing of single nano-systems [Farahani *et al.* (2005); Taminiau *et al.* (2007)]. They are also potentially interesting for compact and ultra-sensitive sensing [Enoch *et al.* (2004); Smythe *et al.* (2007)].

Improving the efficiency of these processes requires an extensive and accurate characterization of ONA necessary to optimize their performance. However, probing the optical response of ONA is particularly challenging owing to the strong confinement of the local field and the dramatic sensitivity of ONA modes to small changes of their electromagnetic environment. This last point renders particularly cumbersome the use of SNOM since the probe (acting itself like an antenna) may interfere with the intrinsic properties of the structure under study. Beyond this difficulty, SNOM imaging have been successfully used for mode mapping on dispersed metal rods, in conventional transmission mode Imura & Okamoto (2006) and collecting the two-photon induced luminescence of gold Imura *et al.* (2004a,b). Lately, gap antennas have also been investigated with s-SNOM in both near-infrared Cubukcu *et al.* (2006) and infrared spectral ranges Yu *et al.* (2007). In fair agreement with theoretical predictions, results show high resolution snapshots of the mode distribution although the field magnitude in the gap was found to be substantially weaker than expected.

1.3 Experimental Setup

A dedicated high resolution confocal scanning microscope has been constructed in order to resolve and measure the TPL signal on single nano-structures. In this section, we describe in detail the set-up and analyze the nature of the TPL signal.

The TPL scanning microscope is based on an inverted IX71 Olympus microscope, which has been modified for our purpose, as depicted in figure 1.3 . On the top part, a sample scanner (TRITOR 102 CAP by Piezosystem Jena) is attached, allowing for a high precision scan of the sample. The antennas were illuminated at normal incidence by a 150 fs-pulsed Ti:Saph laser (76 MHz repetition rate) through an immersion oil objective (Olympus infinity-corrected objective, $\times 100$, Numerical Aperture, $NA = 1.25$).

The polarization state of the incident beam is controlled by using a half-lambda plate and polarizers. Neutral density filters are used to adjust the incident power. In order to improve the resolution and achieve a diffraction limited focus, the numerical aperture of the objective is fully filled with the beam.

While incident photons are coupled into the structure mode, the resulting intense local fields induce locally a two-photon absorption process in gold which leads to a wide-band photoluminescence emission [Beversluis *et al.* (2003)]. This signal is collected back through the same objective and sent to an avalanche photodiode (SPCM-AQRH Single Photon Counting APD from Perkin Elmer) after filtering the incident wavelength. Scanning the sample with respect to the illumination spot enables to map the distribution of TPL intensity around the antenna.

In figure 1.4(A-B) the diffraction limited spot focussed on the sample for the two polarization states is imaged by a CCD camera. As expected for high NA objectives [Pawley (1995)], for linearly polarized input beams the focus has an elongated shape instead of the radial symmetry. This is well confirmed by calculations performed for a polarized focused beam at a glass-air interface (figure 1.4 (C-D)).

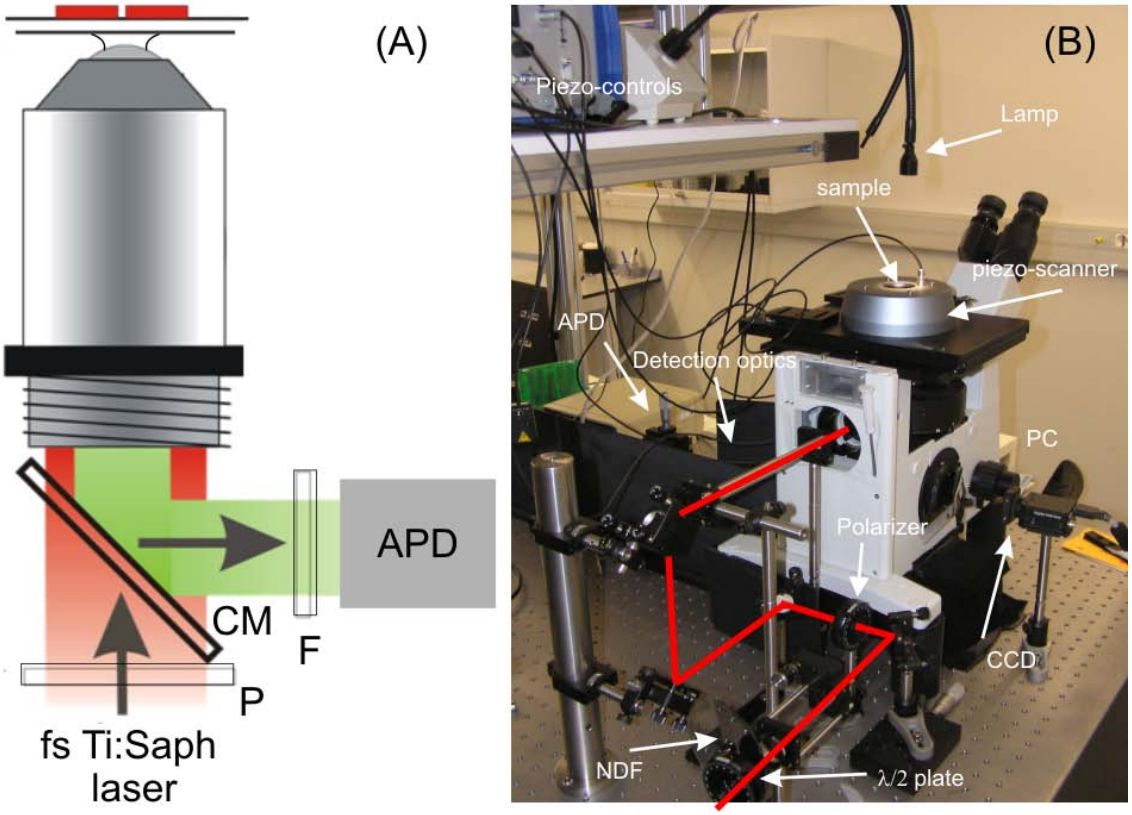

Figure 1.3: *(A) Schematic representation of the TPL setup and (B) Picture of the setup showing the important elements: (NDF) neutral density filter, ($\frac{\lambda}{2}$) half-lambda plate, (P) polarizer, (CM) cold mirror, (F) filter, (APD) avalanche photo-diode, (CCD) camera.*

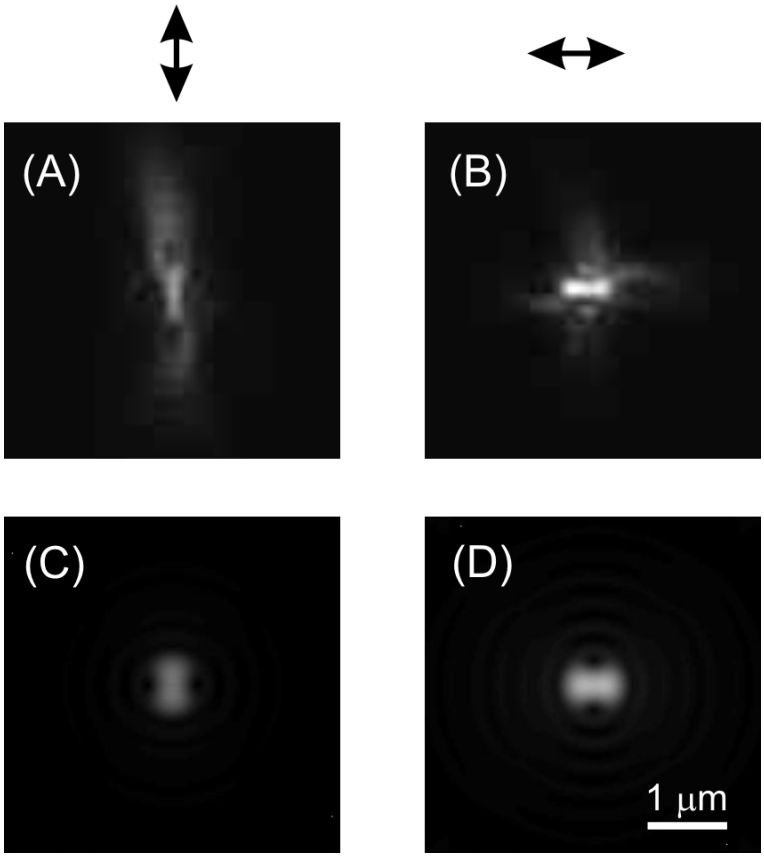

Figure 1.4: *(A-B) Intensity distribution of the beam at the plane of focus for the two incident polarizations recorded with a CCD camera, (C-D) Corresponding simulation.*

For spectroscopic measurements exactly the same incident power on the sample has to be assured for all the measurements. For this reason the incident power is adjusted by taking into account the actual transmission of the optical setup for each wavelength, as calculated by Pawley (1995).

1.4 Analysis of the TPL signal

When measuring on single nanostructures, one is faced to an important limitation: the typical luminescence signal coming from one single structure is very low, thus putting strong restrictions on the incident power levels that allows sufficient signal to noise ratio without destroying the investigated structures. Independently one need to test the reproducibility over several structures to rule out any influence of fabrication defects.

First, in order to study the origin of the signal, we plot in figure 1.5 (A) its dependence with the incident laser power. The incident power was measured at the entrance of the microscope and controlled with a neutral density filter. The points follow a quadratic dependence (a slope of 2.4 in the log-log plot). From the same measurements, the power dependence of the background level can also be extracted as shown in figure 1.5 (B). The linear behavior of the background and the quadratic behavior of the signal coming from the structures confirms that the measured signal mainly results from a two-photon absorption process.

Beyond a certain threshold (in our experiments being around 50 μW) a change is observed, its power dependence moving towards a higher slope (inset of figure 1.5 (A)). This effect is attributed to a structural modification of the antenna combined with the appearance of higher order nonlinear processes, as evidenced by Muhlschlegel *et al.* (2005).

In the following experiments presented, only half of the threshold value (e.g. 25 - 30 μW) has been used to prevent structural change of the structures. This range of power is high enough to lead to a fair TPL signal over noise level even from structures that sustain multipolar resonance (maximum APD signal of a few k-counts for a background of around 40 counts when 30 ms is used as integration time).

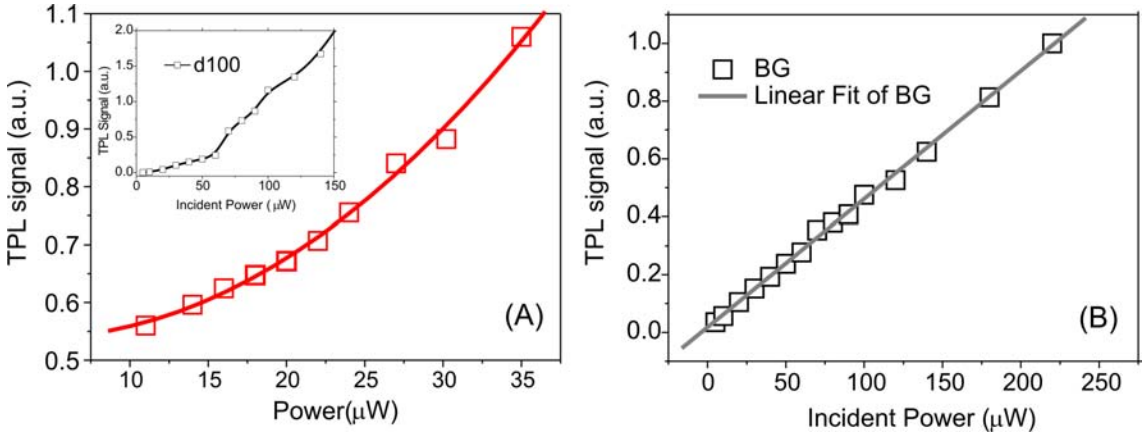

Figure 1.5: *(A) Evolution of the TPL signal with the incident power (the red curve is a quadratic fit). Inset: the full power range, (B) Power dependence of the background (BG) signal (the gray line is a linear fit).*

1.5 Influence of the Excitation and Detection Volumes

In this section complementary experiments were performed in order to asses the influence of the excitation and imaging conditions on the TPL maps.

In our setup the excitation irradiance distribution at the focus is estimated to be about 300 nm (FWHM of 275 and 321 nm for the two orthogonal directions at 730 nm as shown by Pawley (1995)) (figure 1.4).

However, the use of a nonlinear technique is expected to significantly increase the resolution, since the two photon absorption process in gold occurs in a region of about $300/\sqrt{2}$, so approximately 200 nm. The spatial resolution of our TPL measurements was verified by scanning a sample with an array of 100 nm diameter gold particles separated by 500 nm, confirming a resolution of approximately 200 nm.

Intuitively, the incidence and detection volumes should play an important role in the TPL image formation. Interestingly, we will show in this section that TPL maps are mostly dependent on the local excitation of the antenna mode.

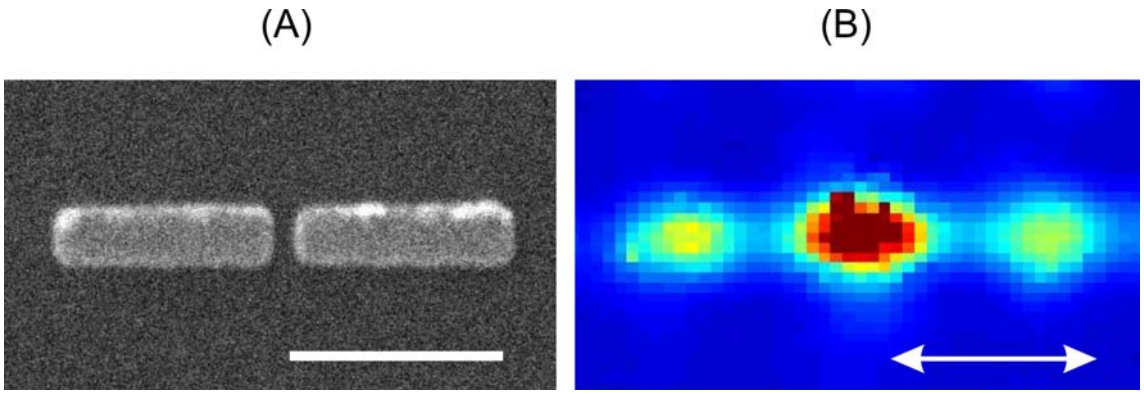

Figure 1.6: *(A)SEM micro-graph of a single antenna fabricated by e-beam lithography (scale bar 500 nm). The structure is 500 nm long, 100 nm wide and 40 nm high. (B) Corresponding TPL map recorded under longitudinal polarizations and for* $\lambda = 730$ *nm.*

In the following, a gap antenna with 500 nm arm length, 100 nm width and 40 nm gap illuminated under resonant conditions (730 nm incident wavelength, longitudinal polarization), as shown in figure 1.6 (A) was used to test our set-up. The TPL map recorded for this antenna under these conditions is dominated by a substantial field confinement in the gap area and at the extremities (figure 1.6 (B)).

Figure 1.7 depicts a scheme of the entire TPL setup, including the details of the optics used in both the incidence and detection paths. To change the illumination area, an iris that controls the objective NA (e.g. to control how much of the objective entrance area is filled) was introduced in the incident path. The less the objective entrance is filled the lower the NA. Figure 1.8 shows the evolution of the TPL resolution and NA for different iris diameters. In this way the resolution of the excitation can be changed from 200 to 450 nm, FWHM.

From the detection side, the combination of the microscope objective NA and the size of the APD's active window (120 μm) gives a detection area of around 1 μm. In order to decrease it, pinholes of different diameters: 50 μm and 30 μm corresponding to areas of 550 nm and 350 nm respectively were used on the

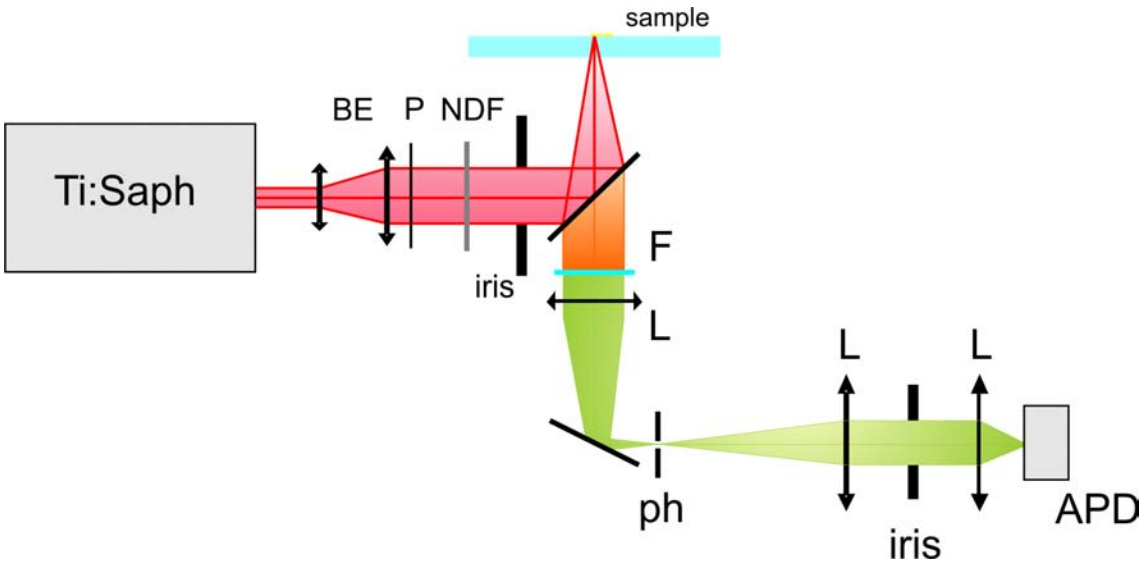

Figure 1.7: *Scheme of the TPL setup including the illumination and detection paths. BE - beam expander, P - pinhole, NDF - neutral density filter, F - filter, L - microscope lens, PH - Detection pinhole, APD - avalanche photodiode.*

detection path. To enlarge it, an iris (equivalent to the one from incident path) was used that allows an increase up to 2 μm.

To verify the evolution of the TPL images with the excitation volume the collection area was maintained at 1 μm while increasing the excitation area from 350 nm to successively 550 and 1000 nm, by stepwise reduction of an iris in the illumination path. The results, summarized in figure 1.9 clearly show how the resolution of the TPL maps is drastically dependent on the excitation area. For an area of 550 nm we can hardy distinguish the central spot from the edges ones and for 1000 nm only an elongated spot is observed.

In a second set of experiments, to check how the TPL images vary with the collection volume, the illumination area was maintained constant to 350 nm and the collection area was decreased from 2 μm to 550 nm by placing an iris on the detection path or a pin-hole in the conjugated image plane. Figure 1.10 shows that there is no major change in the TPL image, although, as expected the level of the signal goes down with the collection area. For a smaller collection area

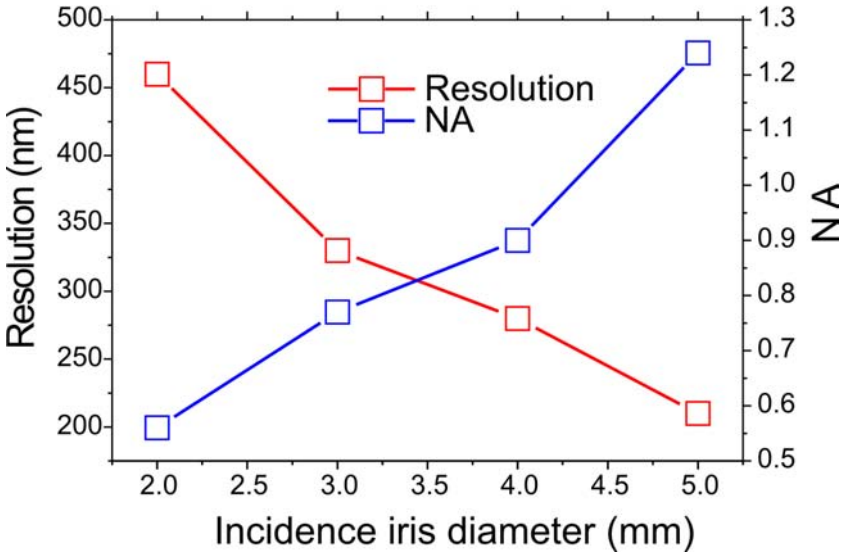

Figure 1.8: *Evolution of resolution and NA for different diameters of the incidence iris.*

some improvement in resolution is observed, but the ratio between the TPL signal within the gap and at the edges remains largely the same. For the smaller collection areas, the recorded images are much more sensitive to the alignment conditions and a small misalignment is probably responsible for the slight asymmetry observed.

These experiments confirm that the TPL distribution along the antenna is not governed by a specific relation between the size of the antenna and the collection area (when varied from 1000 to 350 nm) but rather by the excitation process.

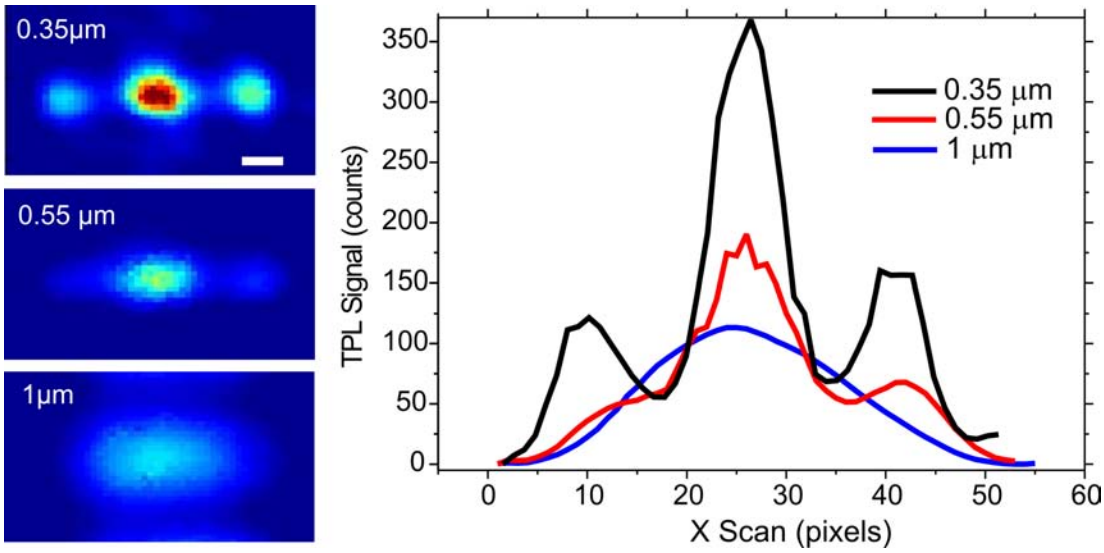

Figure 1.9: *Recorded image of a coupled antenna at resonance when for a fixed detections areas of 1 micron, the illumination area is changed. (Left) The recorded TPL images. (Right) Absolute cross-cuts along the long axis for all the illumination areas. Scale bar: 200 nm.*

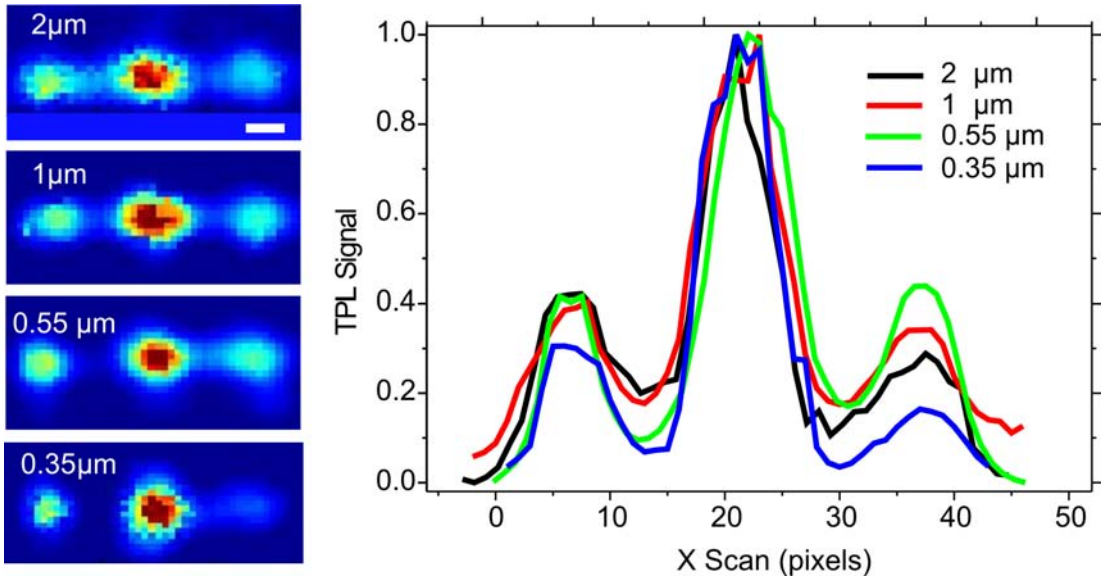

Figure 1.10: *Evolution with the collection area of the TPL image recorded above a coupled antenna at resonance for a fixed illumination area of 350 nm. (Left) TPL scans, (right) Normalized cross-cut along the long axis of the antenna. Scale bar: 200 nm.*

References

Aizpurua, J., Bryant, G.W., Richter, L.J., de Abajo, F.J.G., Kelley, B.K. & Mallouk, T. (2005). Optical properties of coupled metallic nanorods for field-enhanced spectroscopy. *Phys. Rev. B*, **71**, 235420. 4

Beversluis, M.R., Bouhelier, A. & Novotny, L. (2003). Continuum generation from single gold nanostructures through near-field mediated intraband transitions. *Phys. Rev. B*, **68**, 115433. 6

Bouhelier, A., Bachelot, R., Lerondel, G., Kostcheev, S., Royer, P. & Wiederrecht, G.P. (2005). Surface plasmon characteristics of tunable photoluminescence in single gold nanorods. *Phys. Rev. Lett.*, **95**, 267405. 2

Cubukcu, E., Kort, E.A., Crozier, K.B. & Capasso, F. (2006). Plasmonic laser antenna. *Appl. Phys. Lett.*, **89**, 093120. 5

Enoch, S., Quidant, R. & Badenes, G. (2004). Optical sensing based on plasmon coupling in nanoparticle arrays. *Opt. Express*, **12**, 3422. 5

Farahani, J.N., Pohl, D.W., Eisler, H.J. & Hecht, B. (2005). Single quantum dot coupled to a scanning optical antenna: A tunable superemitter. *Phys. Rev. Lett.*, **95**, 017402. 5

Imura, K. & Okamoto, H. (2006). Reciprocity in scanning near-field optical microscopy: illumination and collection modes of transmission measurements. *Opt. Lett.*, **31**, 1474. 5

REFERENCES

Imura, K.I., Nagahara, T. & Okamoto, H. (2004a). Imaging of surface plasmon and ultrafast dynamics in gold nanorods by near-field microscopy. *J. Phys. Chem. B*, **108**, 16344. 5

Imura, K.I., Nagahara, T. & Okamoto, H. (2004b). Plasmon mode imaging of single gold nanorods. *J. Am. Chem. Soc.*, **126**, 12730. 5

Lereu, A.L., Sanchez-Mosteiro, G., Ghenuche, P., Passian, A., Quidant, R., Garcia-Parajo, M. & van Hulst, N.F. (2008). Probing the local field of nanoantennas using single particle luminescence. *Journal of Physics: Conference Series*, **100**, 052038. 4

Muhlschlegel, P., Eisler, H.J., Martin, O.J.F., Hecht, B. & Pohl, D.W. (2005). Resonant optical antennas. *Science*, **308**, 1607. 2, 4, 9

Muskens, O., Giannini, V., Sanchez-Gil, J. & GomezRivas, J. (2007). Strong enhancement of the radiative decay rate of emitters by single plasmonic nanoantennas. *Nano Lett.*, **7**, 2871–2875. 5

Novotny, L. (2007). Effective wavelength scaling for optical antennas. *Phys. Rev. Lett.*, **98**, 266802. 4

Pawley, J., ed. (1995). *Handbook of biological confocal moicroscopy*. Plenium Press. 6, 8, 10

Righini, M., Ghenuche, P., Cherukulappurath, S., Myroshnychenko, V., Garcia de Abajo, F.J. & Quidant, R. (2009). Nano-optical trapping of rayleigh particles and escherichia coli bacteria with resonant optical antennas. *Nano Letters*. 4

Schider, G., Krenn, J.R., Hohenau, A., Ditlbacher, H., Leitner, A., Aussenegg, F.R., Schaich, W.L., Puscasu, I., Monacelli, B. & Boreman, G. (2003). Plasmon dispersion relation of au and ag nanowires. *Phys. Rev. B*, **68**, 155427. 4

Schuck, P.J., Fromm, D.P., Sundaramurthy, A., Kino, G.S. & Moerner, W.E. (2005). Improving the mismatch between light and nanoscale objects with gold bowtie nanoantennas. *Phys. Rev. Lett.*, **94**, 017402. 2, 4

Smythe, E.J., Cubukcu, E. & Capasso, F. (2007). Optical properties of surface plasmon resonances of coupled metallic nanorods. *Opt. Express*, **15**, 7439–7447. 5

Taminiau, T.H., Moerland, R.J., Segerink, F.B., Kuipers, L. & van Hulst, N.F. (2007). Lambda/4 resonance of an optical monopole antenna probed by single molecule fluorescence. *Nano Lett.*, **7**, 28–33. 4, 5

Yu, N., Cubukcu, E., Diehl, L., Bour, D., Corzine, S., J. Zhu, G.H., Crozier, K.B. & Capasso, F. (2007). Bowtie plasmonic quantum cascade laser antenna. *Opt. Express*, **15**, 13272. 5

Chapter 1

High resolution mode mapping and spectroscopy of single nanoantennas

This chapter first describes the high resolution mode mapping and spectroscopy of single nanoantennas. The concepts are then applied to a different system to show the applicability of TPL microscopy to different other gold plasmonic samples.

1.1 From dipolar to multipolar antennas

First single structure TPL measurements were performed on samples of gold dimers supporting dipolar resonances. While the method gives good results, the modes of these structures can not be resolved because of the resolution of the setup. This is why larger structures (e.g. 500 nm) supporting a multipolar resonance were used even though these modes have a much lower quality factor than dipolar ones.

The optical properties of the antennas have been modelled using the Green dyadic method (Appendix A). The geometries we consider consist of gold structures lying onto a glass substrate and illuminated by a polarized plane wave under normal incidence. The nanoparticles are defined as parallelepipeds with 100 nm width 40 nm height and variable length. In this way the scattering spectrum and the distribution map of the near field intensity around the particles can be obtained. To allow a more direct comparison with the experimental data, the actual resolution of the set-up has been taken into account by convoluting the maps with a 2D Gaussian profile with 200 nm, FWHM.

Figure 1.1 shows the TPL mapping of a sample of dimers having arm lengths varying from 100 to 500 nm in steps of 100 nm and with different gaps (30, 35 and 40 nm). A good agreement is found between the TPL response of the sample and the calculated near-field intensity distribution at $\lambda = 740$ nm, for longitudinal polarization.

In addition to imaging at fixed wavelength, the incident wavelength can be tuned in order to monitor the local spectroscopy of the TPL intensity. The TPL signal was collected for all the gap antenna at each wavelength by sampling the

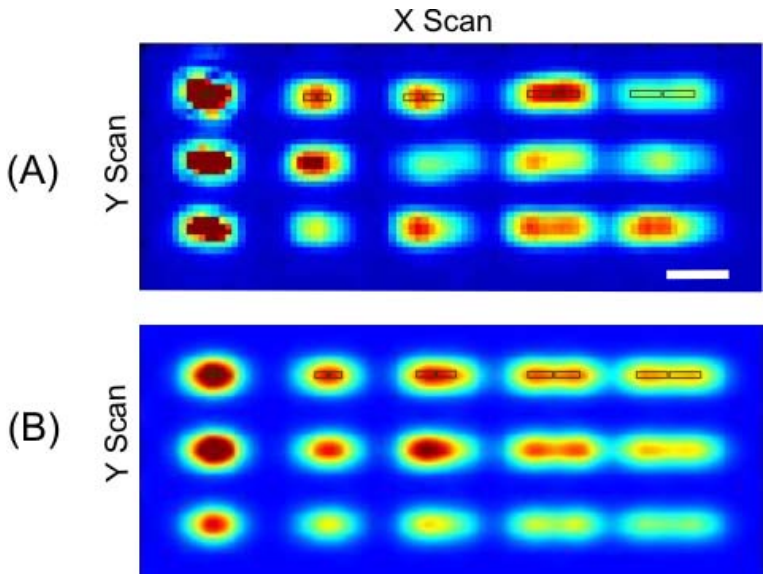

Figure 1.1: *(A) TPL images of gold particle dimers with 3 different gap and arm lengths varying from 100 nm to 500 nm ($\lambda = 740$ nm), (B) Corresponding distribution of the local field $|E|^4$ maps convoluted with a 200 nm FWHM gaussian profile. The structure location and size are represented by the black rectangles. Scale bar 1 μm.*

signal inside an area of 5×5 pixels, after applying a background correction. The resulted data are fitted by a Lorentzian function to determine the actual central resonance position.

As expected, for the 100 nm dimers a dipolar peak at 720 nm associated to a very strong TPL signal can be observed. When the arm's length is increased, the simulations show that the dipolar peak is significantly red-shifted and a quadrupolar peaks appear for higher lengths. In figure 1.2 (C-D) the position of the peaks inside the detection range for both the TPL scans and the simulated spectra are presented. A good qualitative agreement can be observed. Further discrepancies on the resonance position are mainly caused by the differences between the parameters of the fabricated sample and the ideal objects considered in the calculations.

Beyond, one can monitor the red-shift occurring when shortening the gaps

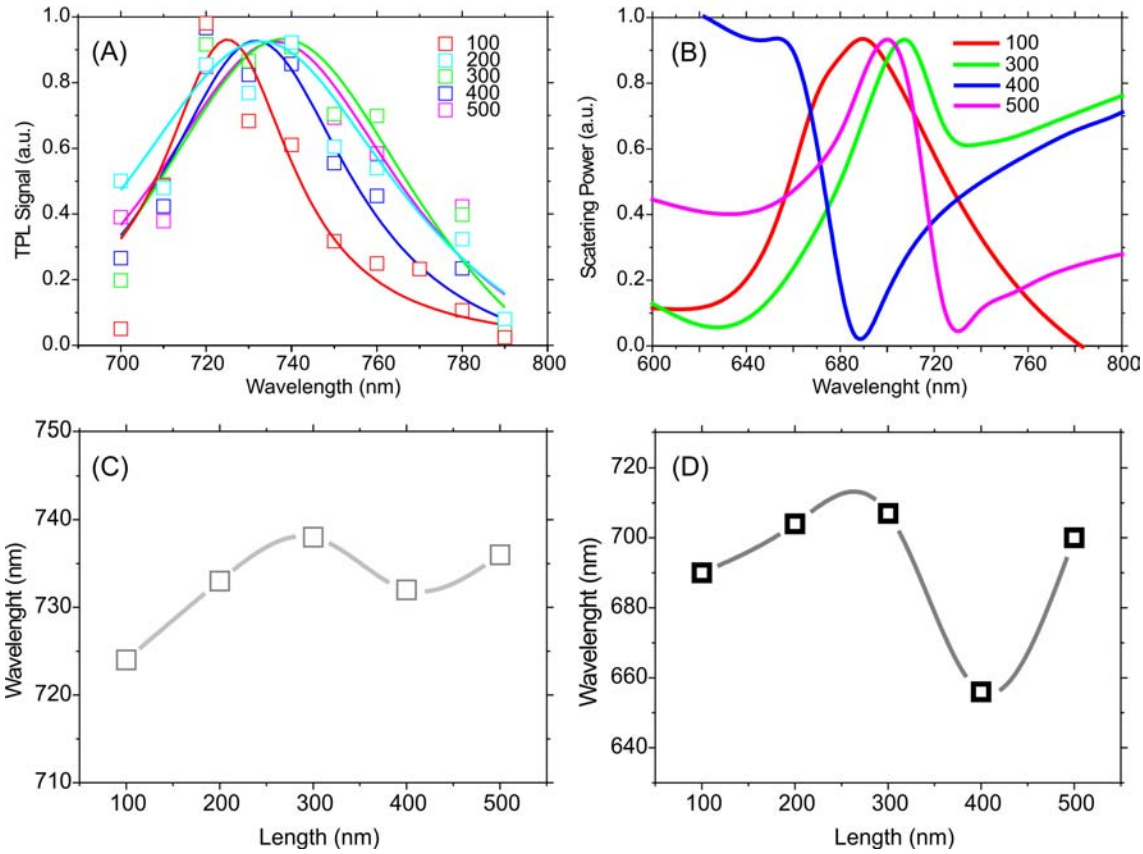

Figure 1.2: *(A) TPL spectra of gold particle dimers with different arms length (the full lines are Lorentz fits of the data). (B) Simulated scattering power of the structures. (C-D) The Experimental and theoretical resonance peaks position for all the lengths (gray lines are a guide for the eye)*

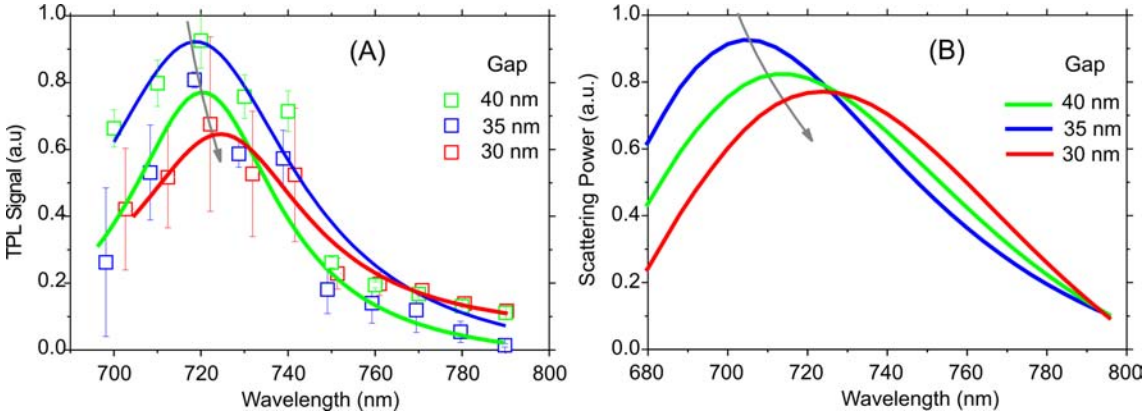

Figure 1.3: *TPL spectra of 100 nm gold particle dimers with 3 different gap sizes (40, 35 and 30 nm). Continuous lines are Lorentz fits of the experimental data.*

size from 40 to 30 nm, as shown in figure 1.3 (A)). Here again, a good agreement is found with the simulations (figure 1.3 (B)) [Rechberger *et al.* (2003)].

1.2 Multipolar Gap Antenna

In this section TPL-scanning microscopy is used to image the mode distribution of single multipolar gold antennas. Besides monochromatic measurements, spectroscopic imaging enables monitoring the resonant behavior of the structures, giving us further insight on the resonance build up. The results are found to be in very good quantitative agreement with full 3D modeling [Ghenuche *et al.* (2008b)].

The gold antennas were fabricated by e-beam lithography. Each of the rods is 500 nm long, 100 nm wide and 50 nm high while the gap between them has been fixed to about 40 nm, with 10 nm accuracy. For comparison, isolated 500 and 1000 nm long gold rods were also included to the sample. The actual resonances of the fabricated antennas were first determined by scattering spectroscopy (figure 1.4). In good agreement with the literature [Aizpurua *et al.* (2005); Novotny (2007)], the resonance of gap-antennas under LP is centered at 730 nm, slightly red-shifted and broadened with respect to the resonance of isolated 500 nm rods

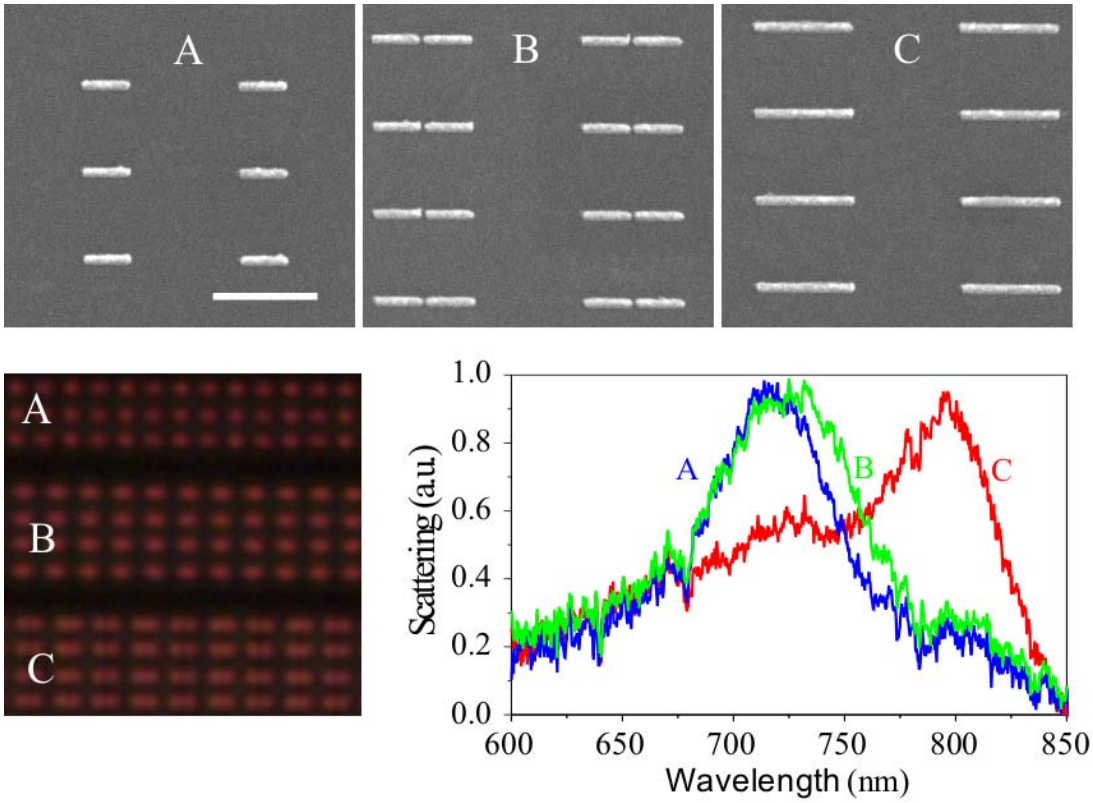

Figure 1.4: *SEM micrograph of gold optical antennas fabricated by e-beam lithography: (A) 500 nm bar, (B) coupled 500 nm antennas and (C) 1000 nm bar (scale bar 1000 nm). In the the bottom-left, a dark field image of the structures is shown and the bottom-right graph shows the corresponding experimental scattering spectra.*

at 710 nm, due to near-field coupling. The 1 μm long rods feature a resonance centered at 800 nm. Under transverse polarization (TP), all three geometries feature a short-axis resonance peaking at around 600 nm (data not shown).

Figure 1.5 shows TPL images recorded over the three different antennas. Measurements were performed under longitudinal polarization, at 730 nm. For a single 500 and 1000 nm gold bar the TPL signal is concentrated at each of the extremities (figure 1.5 (A) and (C)). When coupled to form a gap antenna the TPL map becomes dominated by a substantial field confinement and enhancement within

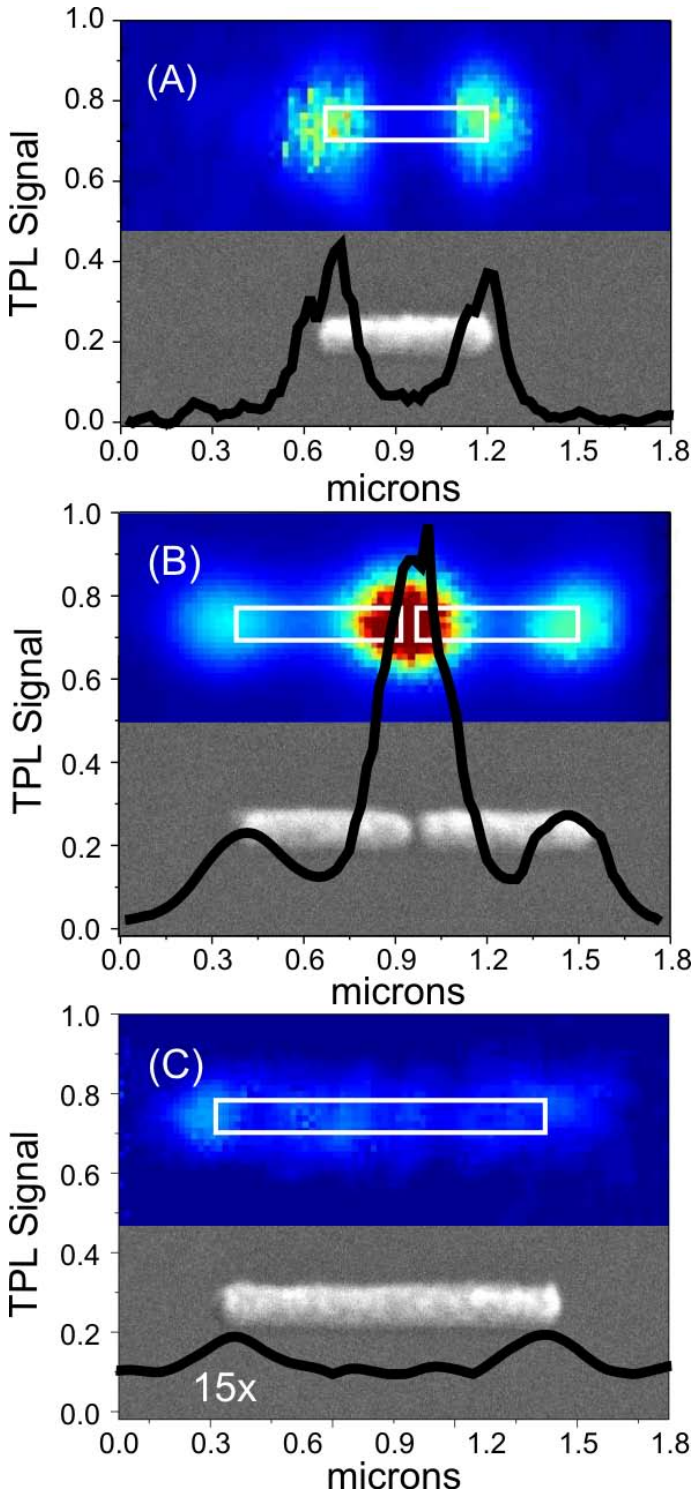

Figure 1.5: *TPL scans recorded on the three different gold antennas and their respective SEM micrographs. (A) 500 nm antenna, (B) coupled 500 nm antennas and (C) 1000 nm bar. All measurements were performed at 730 nm, LP and using the same incident laser power.*

the gap (figure 1.5 (B)).

1.2.1 Measurements at fixed wavelength

To better understand the relation between the measured TPL maps and the actual plasmonic modal field distributions, in this section, near-field calculations based on the finite integral technique (FIT) [CST Microwave Studio 5.1 (2004)] were carried out by Tim Taminiau from Niek van Hulst's group at ICFO.

Figure 1.6 (A) shows the distribution of the electric field (absolute value $|E|$) as calculated in a plane at half height of the three antennas considered experimentally, when illuminated by a plane wave, each at their respective resonances. In order to account for the actual shape of the fabricated structures, round corners with 30 nm radius have been introduced, while calculating with a 2 nm mesh size. The glass substrate and the ITO layer were included in the calculations and the frequency dependent dielectric constant for gold was taken from Palik (1985). For all antennas strong fields build up at the extremities of the bars. Moreover for the gap-antenna, the map is dominated by an even stronger field confinement within the air gap. Additional weaker field modulations along the sides of the gold bars are signatures of the multipolar resonance involved. The oscillations enable to assign directly the actual mode order associated to the resonances. The resonance of the isolated 500 nm bar when illuminated at 710 nm is attributed to a $3\lambda/2$ mode ($n = 1$) with $\lambda_{eff} = 333$ nm. The same $3\lambda/2$ mode is shifted to 730 nm when coupled to form a gap antenna. The 1000 nm bar features a $5\lambda/2$ resonance ($n = 2$) with $\lambda_{eff} = 400$ nm when excited at 760 nm (equation **??**). The $5\lambda/2$ resonance at 760 nm is significantly blue shifted compared to the resonance measured by scattering (figure 1.5).

As previously mentioned, owing to the quadratic dependence of the TPL signal with the local field intensity, we are rather interested in comparing our data with E^4 maps. Such E^4 maps show dominant spots at the extremities and in the gap of the antennas, as enhanced due to the fourth power (figure 1.6 (B)).

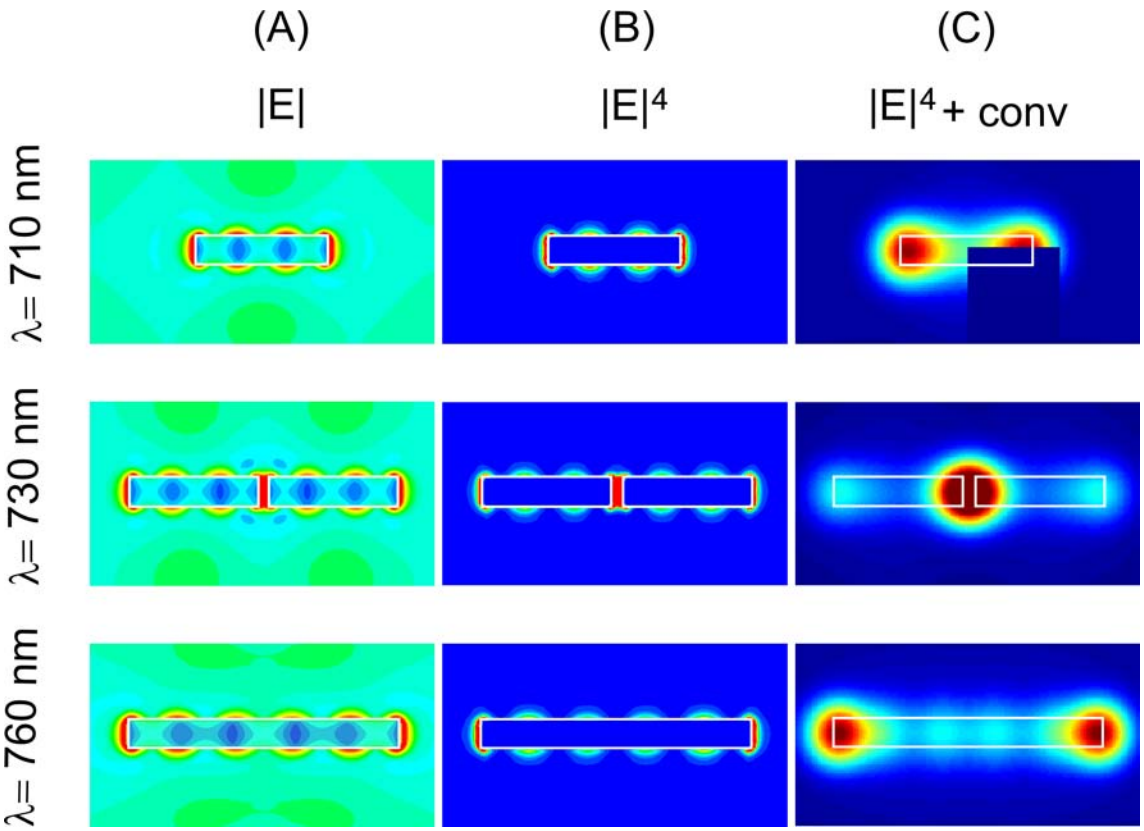

Figure 1.6: *Distribution of (A) the local field $|E|$ and (B) $|E|^4$ computed in the half-plane of the three types of antennas at their respective resonance wavelength. (C) is obtained by convoluting the $|E|^4$ maps with a 200 nm waist Gaussian profile and integrating over the third dimension.*

One should realize that the TPL is excited and detected through a diffraction limited focus, while scanning the antenna; instead the calculations represent the excitation field upon an incident plane wave. Here, to still allow comparison, the resolution of the set-up was taken into account by convoluting the E^4 maps with a 2D Gaussian profile with 200 nm FWHM, as plotted in figure 1.6 (C) . The resulting convoluted maps are fully dominated by the strong intensity in the gap and at the extremities, while the modal field oscillations along the bar are fully averaged out as the effective wavelength is too small to be resolved.

In figure 1.7 we show the TPL maps of all the three structures for LP at their resonance and the respective simulated field. Already at this stage one recognizes how the resulting theoretical maps nicely reproduce the TPL measurements. Next we will focus on the spectroscopic properties and the actual modal field distributions.

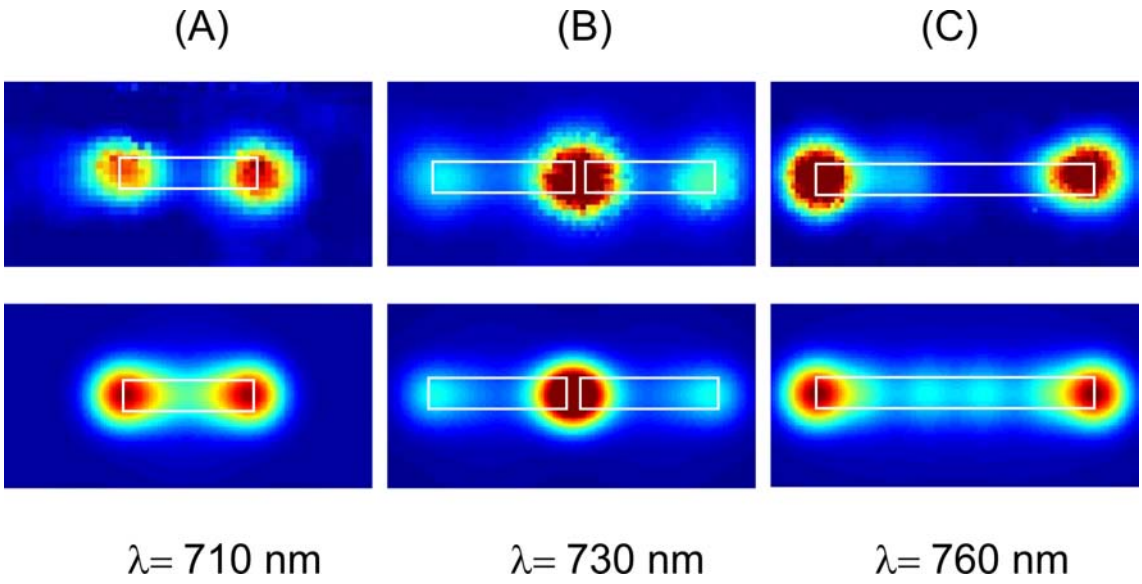

Figure 1.7: *TPL scans recorded on the three different gold antennas: (A) 500 nm bar, (B) coupled antenna and (C) 1000 nm bar. All measurements were performed at their respective resonance wavelength and LP (top). Corresponding convoluted distribution of the local field* $|E|^4$.

1.2.2 Spectroscopic study

At this stage, our observations show that resolved TPL scans can be directly correlated to the distribution of the fourth power of the electric near-field along gold antennas. Beyond measurements at fixed wavelength, a deeper characterization can be assessed by scanning the incident wavelength of the illuminating laser. In this way, one expects to monitor the spectroscopic behavior of determined area of the antenna near-field response.

In practice, for each incident wavelength, accounting for the transmittance of our optical set-up, the laser power was adjusted to maintain constant the power incident on the structure. Figure 1.8 (A) shows the evolution of the TPL map recorded over the gap antenna when the wavelength is scanned from 710 to 770 nm by steps of 10 nm. For comparison, figure 1.8 (B) shows the evolution of the corresponding convoluted $|E|^4$ maps. The resonance at 730 nm is nicely reproduced, while the intensity decreases rapidly by moving only 30 - 40 nm out of resonance. The maxima at the extremities appear slightly shifted compared to the gap maximum, with a $\sim$10 nm blueshift in the experiment. We repeated the measurements for the 500 and 1000 nm long antennas. For further quantitative analysis, the spectra of the average TPL intensity in the gap area of the coupled antennas together with the corresponding maxima of the convoluted $|E|^4$ maps are plotted in figure 1.10 (B).

In figure 1.9, we show the TPL and the associated calculated maps for the 1000 nm antenna, when the wavelength is scanned from 730 to 780 nm by steps of 10 nm. Again, a very good agreement between the theory and simulations is found.

Figure 1.10 summarizes the TPL spectroscopy measured on all the structures. In good agreement with theoretical predictions, TPL spectroscopy enables retrieving the actual resonances of the local field around the structures and determining their experimental specificities such as central wavelength and bandwidth. Furthermore, it enables a deeper analysis of the antenna properties. Interestingly,

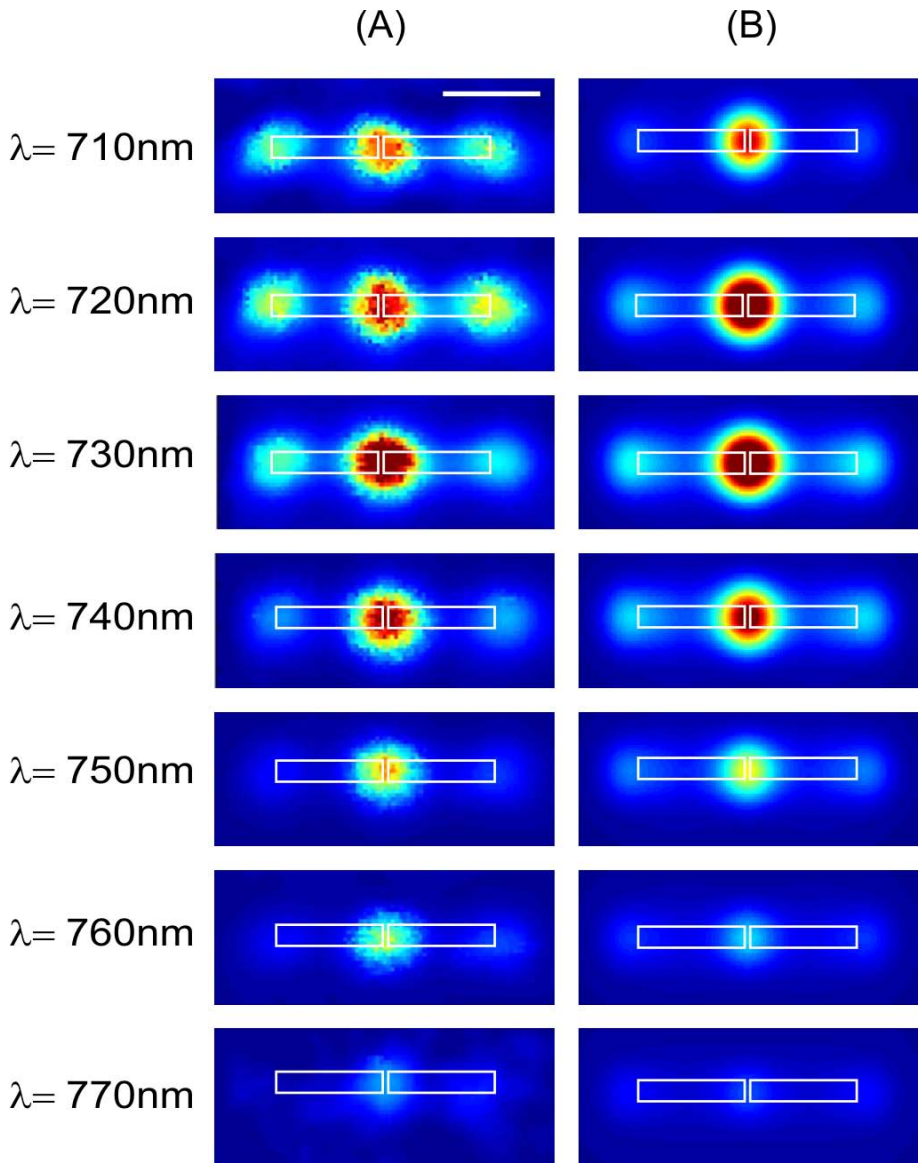

Figure 1.8: *Evolution with the incident wavelength of (A)the TPL map and (B) the computed convoluted $|E|^4$ distribution over a single gap antenna (scale bar: 500 nm).*

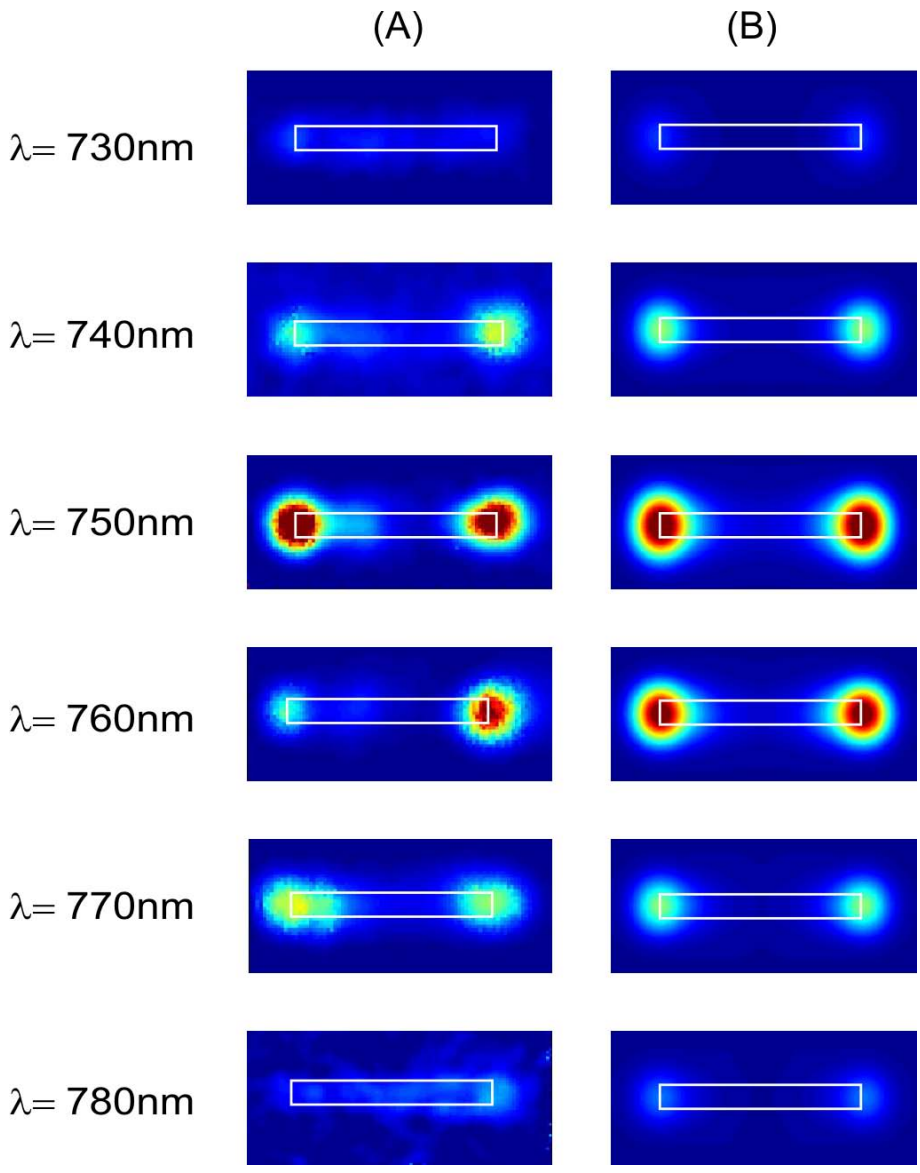

Figure 1.9: *Evolution with the incident wavelength of (A) the TPL map and (B) the computed convoluted $|E|^4$ distribution over a single 1000 nm antenna.*

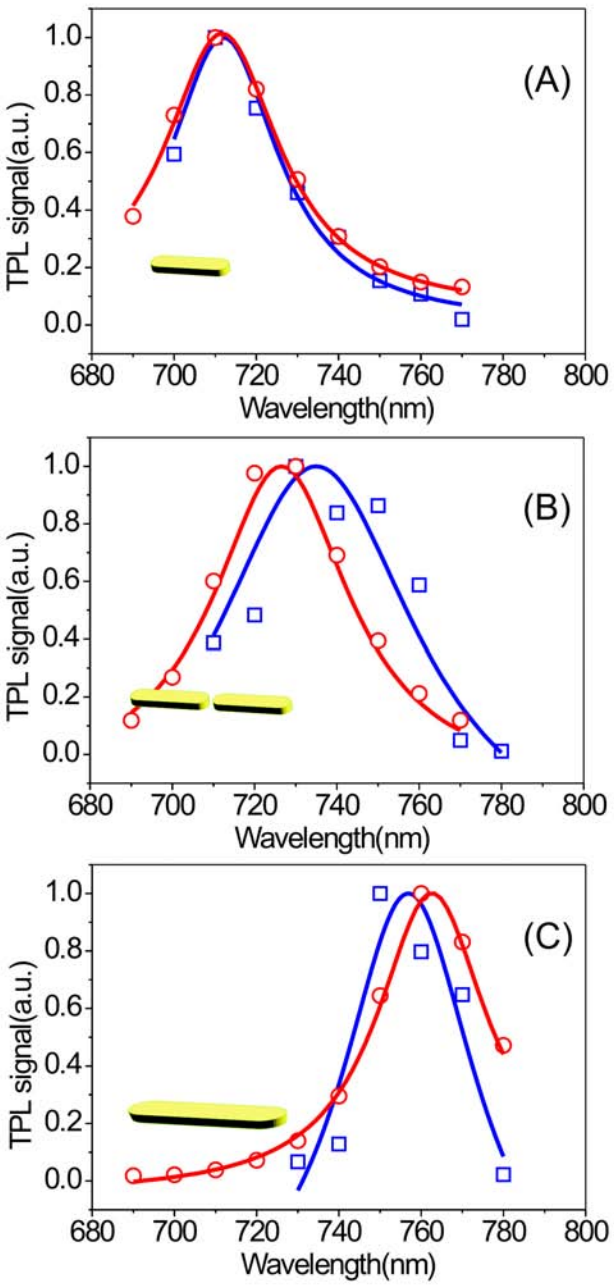

Figure 1.10: *Evolution with the incident wavelength of the TPL signal (blue squares) (A) for the extremities of a 500 nm antenna, (B) the gap of a coupled antenna, and (C) the extremities of a 1000 nm antenna. For comparison, the red circles account for the evolution of the corresponding calculated* $|E|^4$*. For comparison, all spectra have been normalized to unity (continuous lines are guides to the eyes).*

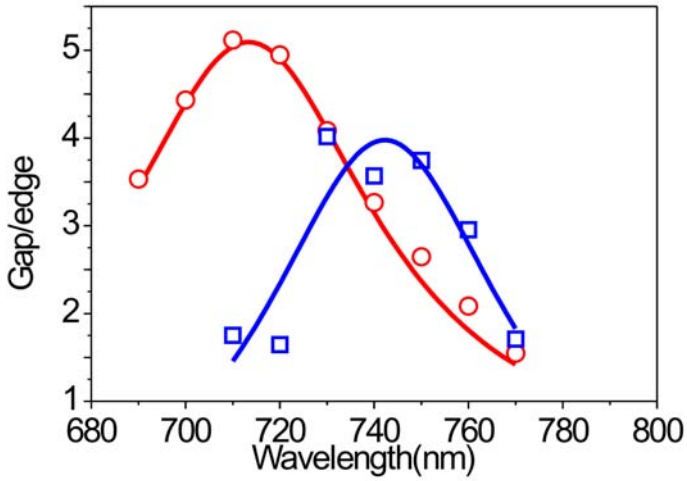

Figure 1.11: *Spectral evolution of the ratio between the signal in the antenna gap and at its extremities (blue squares). The red circles account for the evolution of the corresponding calculated $|E|^4$ ratio (continuous lines are guides to the eyes).*

while the scattering measurements provide a resonance at around 800 nm for the 1000 nm antenna (figure 1.4), the TPL spectrum shows the actual near field resonance peaking around 760 nm, as also predicted by theory. This may indicate that the complex far field scattering pattern of the $5\lambda/2$ mode leads to different spectral features compared to near field spectroscopy [Messinger *et al.* (1981); Søndergaard & Bozhevolnyi (2007); ten Bloemendal *et al.* (2006)].

Measuring the actual local field enhancement in plasmon nanoantennas is a cumbersome task which has led to results often far from the theoretical predictions. As mentioned above, the use of a near-field probe may substantially affect the intrinsic response of the antenna. Although the TPL intensity is clearly related to the local-field enhancement, it does not give a quantitative value. Considering the ratio between longitudinal and transversal resonances for a given antenna will also not yield accurate results since the comparison fully depends on the relative spectral position of both resonances [Muhlschlegel *et al.* (2005)].

Here TPL micro-spectroscopy provides an interesting alternative by comparing directly the TPL intensity in the gap at resonance and away from it. Since the signal off resonance is given by the lowest value detectable from the noise level of our experiment, this leads to an estimation of a minimum value for the actual enhancement. This way, we find a TPL enhancement factor of at least 80 for the gap antenna versus 15 for the single antenna, in very good agreement with the simulations. Beyond the evaluation of the actual local field enhancement factor due to resonance, the combination of spatial resolution and spectral analysis of TPL spectroscopic imaging also enables a deeper analysis of the antenna physics.

To illustrate the potential of our method, we plot in figure 1.11 the evolution with the incident wavelength of the ratio between the TPL signal for the gap area and for the antenna extremities. Interestingly, while both regions feature a resonance centered nearly at the same wavelength, the ratio features a peak centered around 740 nm for which the TPL response for the gap becomes up to 4 times stronger than at the edges. This effect is well reproduced by the corresponding $|E|^4$ analysis, despite a shift in wavelength mainly attributed to to subtle shifts in the resonance maxima for the weak TPL intensity at the extremities. These results indicate that the coupling between the arms does not simply introduce a new mode, with a fixed charge distribution, whose amplitude is enhanced at resonance, as observed for a single bar. Instead, for the gap antenna, a dynamical redistribution of charge along the antenna is observed. We believe this constitutes the first experimental observation of the spectral evolution of the mode field of a coupled nanoantenna.

1.3 Mode mapping of plasmonic stars using TPL microscopy

In this section, another geometry of gold nanostructures is investigated to demonstrate the applicability of TPL microspectroscopy. The star-like plasmonic structure features a strong dependence on the polarization of the illumination light. Recent two-photon photoemission electron microscopy (PEEM) measurements on similar structures have successfully demonstrated the adaptive control of the local optical fields distribution through a complex shaping of the incident polarization state [Aeschlimann *et al.* (2007)]. Here, we combine far-field spectroscopy and TPL microscopy to investigate the local optical response of this geometry to different orientations of a linearly polarized excitation. The TPL distribution over the structure is found to be strongly dependent on the incident polarization state, in good agreement with the corresponding electric near-field intensity map computed using the Green dyadic method.

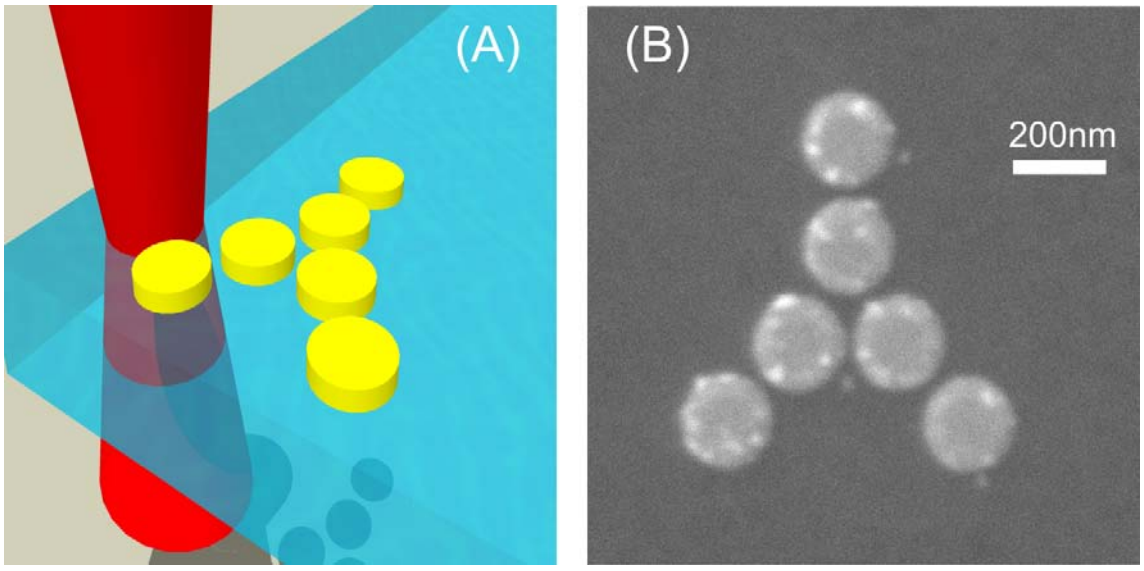

Figure 1.12: *(A) Sketch of the star structure and (B) SEM image of one of the structures.*

The fabricated structures consist of six 200 nm diameter and 40 nm height

discs arranged in a star-like shape (figure 1.12). The gap between consecutive discs was measured to be about 30 nm. Several of these structures were fabricated on the substrate in the form of a matrix. A period of 2 μm prevents significant electromagnetic interaction between adjacent structures.

1.3.1 Far-field Spectroscopy

In order to study the resonance characteristics of the structures, far-field scattering spectroscopy measurements were performed under dark-field illumination using a spectrometer coupled to an optical microscope through a multimode fiber. A polarizer placed in the illumination path allowed us to control the angle of polarization - ϕ of the incident light with respect to the sample. The results, including reference measurements on isolated disks, dimers and trimers, are summarized in figure 1.13 for different orientations of the incident polarization.

For a polarization along the vertical axis ($\phi = 0^o$), the star features a broad resonance centered at around 800 nm, significantly red shifted with respect to the respective resonances of the single disk, dimer and trimer (figure 1.13 (B)). This tends to indicate that, under this polarization, the structure supports a resonant mode, resulting from the complex near-field coupling between the constitutive disks, which is governed neither by dimers nor the trimer contained within the arrangement. Interestingly, very similar resonances are found for $\phi = 60^o$ (figure 1.13 (D)) and $\phi = 90^o$ (figure 1.13 (C)) revealing no significant dependence on the incident polarization of the scattering spectroscopy from the star.

1.3.2 Two-photon Luminescence Microscopy

Far-field spectroscopy measurements provided an insight in the resonance behavior of the structure and from these data we are now interested in investigating the associated local field distribution.

In our setup a $\lambda/2$ waveplate in the incident beam path allowed to control the polarization angle of the incident beam. The incident intensity of the light is

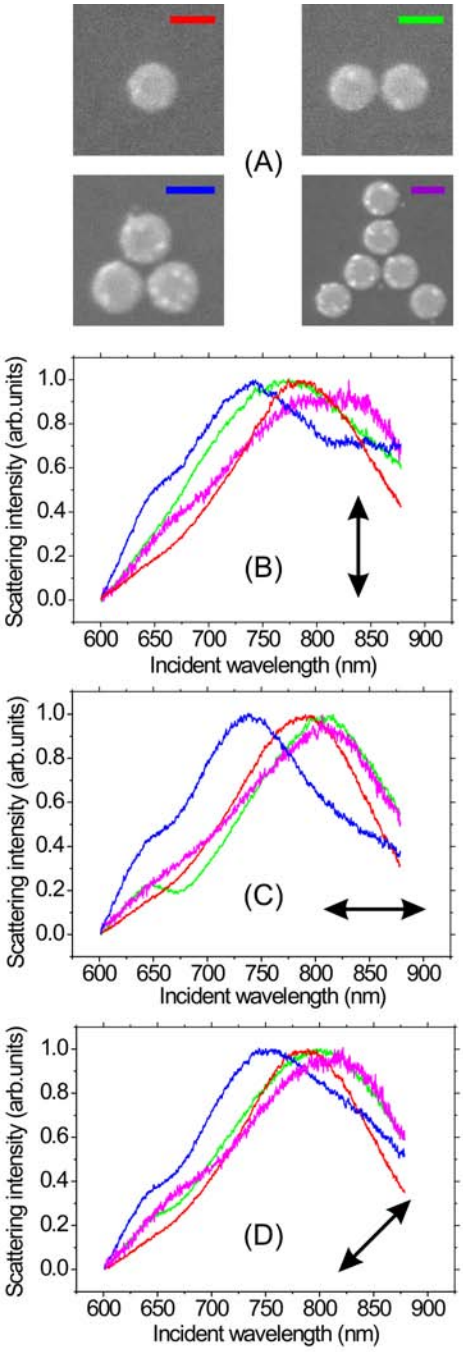

Figure 1.13: *(A) SEM images of single disk, dimers, trimers and stars. Scale bar 200 nm. Corresponding normalized scattering spectra for different orientations of the incident linear polarization: (B)* 0 ° *(C)* 90 ° *(D)* 60 °.

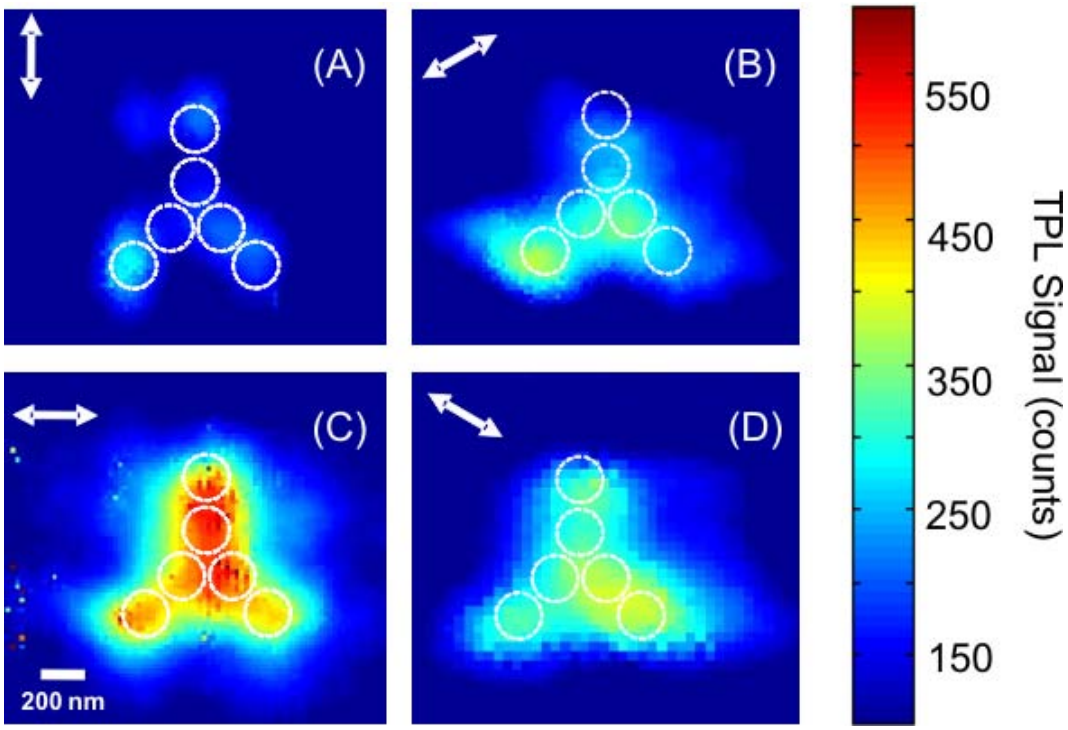

Figure 1.14: *TPL scans recorded above a single star for different polarizations of the incident light: (A)* 0° *(B)* 60° *(C)* 90° *(D)* 130°. *The white dashed circles locate the approximate position of the gold disks.*

always kept constant for all the polarization angles.

Figure 1.14 shows the TPL scans recorded over a single structure at an incident wavelength of 730 nm for four different orientations of the incident field. For an incident field polarized along the vertical axis ($\phi = 0^o$) the TPL intensity is found to be stronger at the extremities of the three arms (figure 1.14 (A)). On rotating the polarization by 60° (counter clockwise), a drastic change in the TPL distribution is observed (Figure 1.14 (B)). Now, signal dominates along the left bottom arm. This indicates that the local response is determined by the gap effects where the incident field would create strong surface charge gradients resulting into strong field magnitudes. Indeed a symmetrical pattern is achieved when aligning the polarization along the right bottom arm (130°) (figure 1.14 (D)). Finally it is interesting to see how the TPL emission concentrates at the

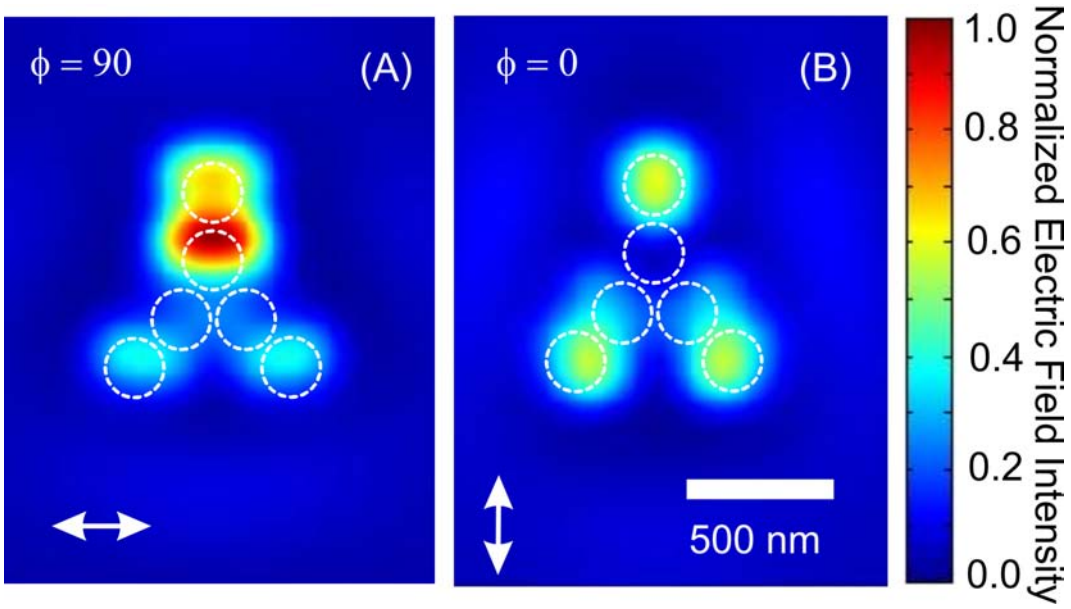

Figure 1.15: *Numerical simulations of the* $|E|^4$ *computed 20 nm above the structure for two different orientations of the incident polarization. A convolution with a 200 nm Gaussian profile was performed.*

star center when the polarization is orthogonal to the top arm (90 °) (figure 1.14 (C)).

At this point it is interesting to compare the experimental data with numerical simulations of the electric near field intensity distribution based on the Green dyadic method [Martin *et al.* (1995)]. In our model, the structure is illuminated through a glass substrate under normal incidence by a linearly polarized plane wave. Figure 1.15 shows the theoretical map for two directions of the incident polarization, $\phi = 0^o$ and 90^o. A comparison with the corresponding experimental maps of figure 1.14 (A) and (C) shows that the distribution of the TPL emission recorded in our experiment clearly relates to the actual near-field distribution across the structure, providing direct insight into the spatial map of the mode.

Relying on the correlation between TPL maps and local field distribution, a further analysis of our experimental data enables us to asses the actual ability to control the confinement of fields in the star geometry through a simple rotation of

the incident linear polarization. To illustrate this concept, we plot in figure 1.16 the angular dependence of the TPL intensity measured at each extremity of the three arms. Each point corresponds to an average TPL intensity over an area of 5×5 pixels above the three outer disks. This graph indicates that the confinement of the local field at determined locations of the structures can be substantially influenced by the polarization state. A maximum field concentration is achieved at the top particle when the polarization is perpendicular to the vertical axis (90 °). Conversely, the signal is maximum at the bottom-left and bottom-right particles for a polarization at 60 ° and 130 °, respectively. The difference in signal between $\phi = 0$ ° and 180 ° is attributed to the small structural modifications of the structures that may occur after many consecutive scans.

We believe such behavior opens possibilities for selective optical addressing of different objects located nearby the extremity of each of the star arms.

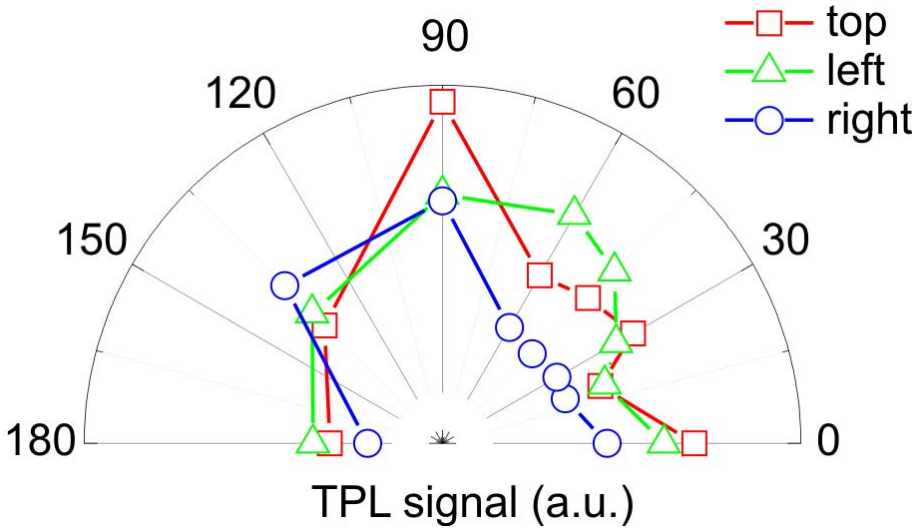

Figure 1.16: *Polarization dependence of the TPL intensity over a star-like structure. The red, blue and green line represents the average TPL signal around the top, left and the right arms, respectively.*

1.4 Conclusions

- We have presented a systematic study by TPL microscopy of gold nanoantennas. Our results show how TPL maps can be directly compared with the convoluted distribution of the fourth power of the local electric field calculated with 3D simulations.

- By monitoring the evolution of the TPL distribution with the incident wavelength we have assessed the actual resonance features such as central wavelength and bandwidth for dipolar and multipolar structures.

- In good agreement with theoretical predictions, spectroscopic imaging enabled us to measure a ten-fold enhancement of the local field intensity in the gap associated to the mode resonance.

- We have monitored for the first time in direct space the physical mechanism of field concentration within the gap as a result of a dynamical charge redistribution due to the near-field coupling between the two arms.

- A detailed far-field and near-field study of star-like nanostructures was performed. While the far-field spectroscopic data do not show significant dependence on the orientation of the incident polarization, TPL measurements reveal a drastic redistribution of the local field across the structure. This local reconfiguration of the field at the structure extremities, well corroborated by full 3D numerical simulations, could enable controlling dynamically the optical addressing of isolated adjacent nanobjects.

1. HIGH RESOLUTION MODE MAPPING AND SPECTROSCOPY OF SINGLE NANOANTENNAS

Chapter published as:

- **P. Ghenuche**, S. Cherukulappurath and R. Quidant, *Mode mapping of plasmonic stars using TPL microscopy*, **New J. Phys. 10**, 105013 (2008): Ghenuche *et al.* (2008a)

- **P. Ghenuche**, S. Cherukulappurath, T. H. Taminiau, N. F. van Hulst and R. Quidant, *Spectroscopic mode mapping of plasmonic gold nano-antennas*, **Phys. Rev. Lett. 101**, 116805 (2008), paper highlighted in Nature 455, 887(2008): Ghenuche *et al.* (2008b)

References

Aeschlimann, M., Bauer, M., Bayer, D., Brixner, T., Garcia de Abajo, F.J., Pfeiffer, W., Rohmer, M., Spindler, C. & Steeb, F. (2007). Adaptive subwavelength control of nano-optical fields. *Nature*, **446**, 301–304.

Aizpurua, J., Bryant, G.W., Richter, L.J., de Abajo, F.J.G., Kelley, B.K. & Mallouk, T. (2005). Optical properties of coupled metallic nanorods for field-enhanced spectroscopy. *Phys. Rev. B*, **71**, 235420. 5

CST Microwave Studio 5.1, w. (2004).

Ghenuche, P., Cherukulappurath, S. & Quidant, R. (2008a). Mode mapping of plasmonic stars using tpl microscopy. *New J. Phys.*, **10**, 105013 (8pp).

Ghenuche, P., Cherukulappurath, S., Taminiau, T.H., van Hulst, N.F. & Quidant, R. (2008b). Spectroscopic mode mapping of resonant plasmon nanoantennas. *Phys. Rev. Lett.*, **101**, 116805.

Martin, O.J.F., Girard, C. & Dereux, A. (1995). Generalized field propagator for electromagnetic scattering and light confinement. *Phys. Rev. Lett.*, **74**, 526–529.

Messinger, B.J., von Raben, K.U., Chang, R.K. & Barber, P.W. (1981). Local fields at the surface of noble-metal microspheres. *Phys. Rev. B*, **24**, 649–657.

REFERENCES

Muhlschlegel, P., Eisler, H.J., Martin, O.J.F., Hecht, B. & Pohl, D.W. (2005). Resonant optical antennas. *Science*, **308**, 1607. 15

Novotny, L. (2007). Effective wavelength scaling for optical antennas. *Phys. Rev. Lett.*, **98**, 266802. 5

Palik, E., ed. (1985). *Handbook of Optical Constants of Solids*. Academic Press, New York.

Rechberger, W., Hohenau, A., Leitner, A., Krenn, J.R., Lamprecht, B. & Aussenegg, F.R. (2003). Optical properties of two interacting gold nanoparticles. *Opt. Comm.*, **220**, 137–141.

Søndergaard, T. & Bozhevolnyi, S.I. (2007). Metal nano-strip optical resonators. *Opt. Express*, **15**, 4198–4204.

ten Bloemendal, D., Ghenuche, P., QuidantI, R., Cormack, G., Loza-Alvarez, P. & Badenes, G. (2006). Local field spectroscopy of metal dimers by tpl microscopy. *Plasmonics*, **1**, 41.

Chapter 1

Summary

The main achievement of this thesis has been to the engineer different plasmon-resonant nanoparticles able to confine light fields down to the sub-λ scale and to characterize them with TPL microspectroscopy. Our study shows that the TPL micro-spectroscopy is a powerful technique to probe their local fields and can provide additional data on the electromagnetic modes of the nanostructures, being able to resolve the finest resonant features. The combination of the TPL and linear spectroscopy is shown to be very beneficial for the study of these type of structures.

The TPL response of ensembles of strongly coupled metal nanostructures was investigated. Dimers with nanometric gaps evidenced strong spectroscopic signatures. In the case of finite chains illuminated under total internal reflection, the in-plane forward scattering of the particles contributed in strengthening of their coupling, leading to sharp resonances. The TPL measurements are well corroborated by calculations based on the Green dyadic method.

To overcome the limitations of measurements on large ensembles, a dedicated set-up was developed to measure the response of single objects. In parallel, considerable efforts were dedicated to the improvement of the fabrication methods

of the structures, to assure the smallest feature possible with a lift-off technique and a good reproducibility over a large number of structures.

Chapter 4 is dedicated to a systematic study by TPL microscopy of single gold nano-antennas. The results show how TPL scans can be directly compared with the convoluted distribution of the fourth power of the calculated local electric field. By monitoring the evolution of the TPL distribution with the incident wavelength we have assessed the resonance features such as central wavelength and bandwidth for dipolar and multipolar structures.

In good agreement with theoretical predictions, spectroscopic imaging enabled us to measure a ten-fold enhancement of the local field intensity in the gap associated to the mode resonance of a single gap antenna. We have monitored in direct space the physical mechanism of field concentration within the gap as a result of a dynamical charge redistribution due to the near-field coupling between the two arms.

A detailed far-field and near-field study of star-like nanostructures has been performed, showing a drastic redistribution of the local field across the structure with the orientation of the incident polarization. This reconfiguration of the local field at the structure extremities could enable controlling dynamically the optical addressing of isolated adjacent nanobjects.

TPL micro-spectroscopy can be successfully applied in studies where probing the unperturbed local field near plasmonic nanostructures is required. Such investigations are crucial in applications such SERS spectroscopy, bio-sensing and enhanced fluorescence, optical trapping, where one needs to asses the actual field experienced by a nearby molecule.

Here we have investigated structures created by e-beam lithography (Appendix A). However, chemically grown structures with a sharp shape and monocrystallinity can offer important advantages compared with lithographic methods by minimizing surface plasmon damping due to scattering at roughness or domain boundaries as demonstrated by Ditlbacher *et al.* (2005).

References

Ditlbacher, H., Hohenau, A., Wagner, D., Kreibig, U., Rogers, M., Hofer, F., Aussenegg, F.R. & Krenn, J.R. (2005). Silver nanowires as surface plasmon resonators. *Phys. Rev. Lett.*, **95**, 257403.

Appendix A

Theoretical calculations: the Green's dyadic method

In order optimize the structural and illumination parameters and to simulate the response of the structures described in this thesis, we have performed extensive numerical calculations based on the Green dyadic method [Girard *et al.* (1997); Greffet & Carminati (1997); Martin *et al.* (1995)]. The codes we used were originally developed by J.C. Weeber at Université de Bourgogne, France.

This formalism, which only requires the definition of the geometry and dielectric function of the object under study, provides a self-consistent resolution of Maxwell's equations, accounting for the multipolar response of metallic nanoparticles and the presence of the substrate. Recently, it has been shown that the consideration of multipolar particle modes is required to fully describe the near-field coupling between nanostructures with larger dimensions (comparable with the wavelength) [Girard & Quidant (2004)].

The method offers an advantage in computation time, compared with other techniques, by employing only a discretization of the scatterer and not of the substrate or the reference medium in which the scatterer is embedded. The

A. THEORETICAL CALCULATIONS: THE GREEN'S DYADIC METHOD

principles of this method are briefly listed below.

We start by considering a scatterer which is described by the dielectric tensor $\epsilon(\mathbf{r},\omega) = \epsilon_{ref}(\omega) + \epsilon_s(\mathbf{r},\omega)$, embedded in a infinite homogenous reference medium $\epsilon_{ref}(\omega)$. This scattering system can be a single object or formed by disconnected parts that are embedded in the reference system, with the tensor $\epsilon_{ref}(\mathbf{r},\omega)$ vanishing outside of the scattering system (figure A.1 (A)).

When the considered object is illuminated with an incident electric field $E_0(\mathbf{r})$, the scattered field $E(\mathbf{r})$ is a solution of the vectorial wave equation:

$$- \bigtriangledown \times \bigtriangledown \times E(\mathbf{r}) + k_0^2 \epsilon(\mathbf{r},\omega) E(\mathbf{r}) = 0, \tag{A.1}$$

where the $\epsilon(\mathbf{r},\omega)$ is the relative dielectric permittivity and k_0 is the wave number in vacuum. The field $E(\mathbf{r})$ at any point of the reference system can be then obtained using the Lippmann-Schwinger equation:

$$E(\mathbf{r}) = E_0(\mathbf{r}) - k_0^2 \int_v d\mathbf{r'}\; G^0(\mathbf{r},\mathbf{r'},\omega)\; \epsilon_s(\mathbf{r'},\omega)\; E(\mathbf{r'}), \tag{A.2}$$

where v is the volume of the perturbation and the Green's tensor, $G^0(\mathbf{r},\mathbf{r'},\omega)$ is describing the response of the system in position $\mathbf{r}$ to a point-like source excitation from $\mathbf{r'}$. Its main elements are computed from the components of the electric field emitted in $\mathbf{r}$ by three orthogonal dipoles located at $\mathbf{r'}$ (figure A.1 (B)).

Equation A.2 shows that the knowledge of the field in the scattering system is enough to compute the response at any position of the reference system using the Green's tensor $G^0(\mathbf{r},\mathbf{r'},\omega)$ associated with the homogeneous reference system. This tensor is known analytically for a homogeneous system [Martin *et al.* (1995)]. Since our structures are lying onto a glass substrate, a correction $G^0_{surface}(\mathbf{r},\mathbf{r'},\omega)$ is included to account for the effect of the surface (figure A.1 (C)).

The far-field scattering spectrum can be evaluated by using the asymptotic form of the tensor (e.g. in the limit of $\mathbf{r} \to \infty$) [Quidant (2002)].

For larger scatterers, the volume v is discretized in small cubic meshes, which are then treated as point scatterers (figure A.1), the integral from equation A.2

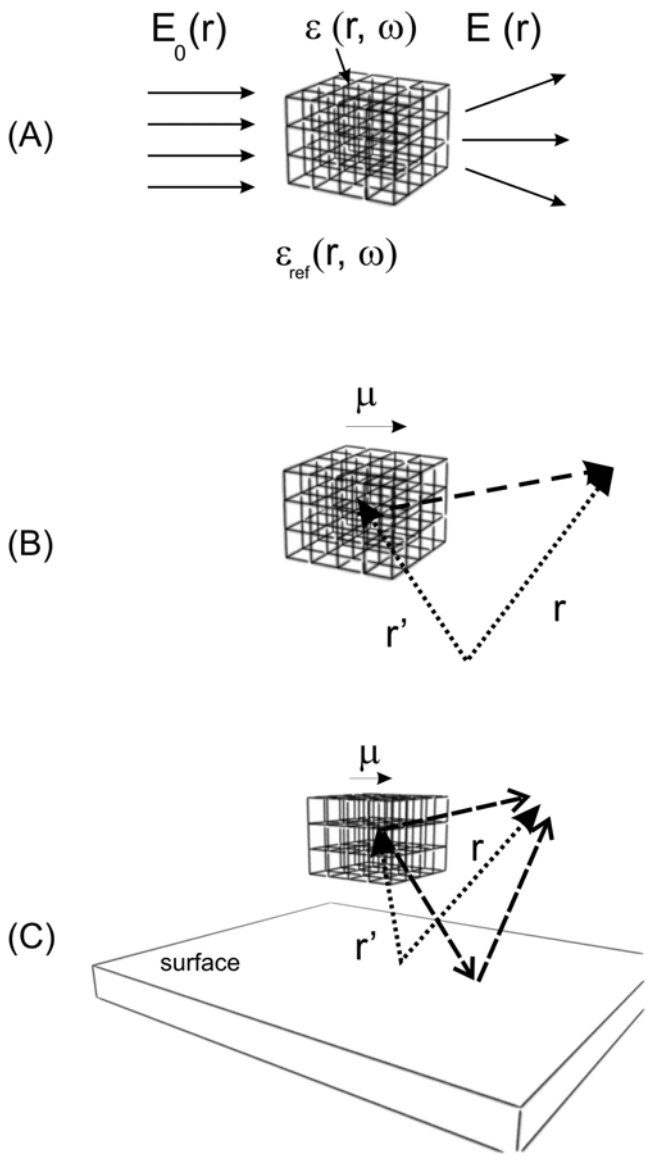

Figure A.1: *(A) Electric field $E_0(\boldsymbol{r})$ incident on a discretized scattering system $\epsilon(\boldsymbol{r}, \omega)$ embedded in a reference medium $\epsilon_{ref}(\omega)$, (B) the physical explanation of the Green's tensor in an homogenous medium and (C) in the presence of a surface.*

becoming a sum over finite volumes. In this way the structure can take arbitrary shape and the near-field map around the structure can be computed.

Small deviations between experimental and theoretical data are mainly the result of the differences between the modeled and real particles shape. The shape determined by AFM measurement or SEM imaging is only approximated in the calculations, due to the applied cubic discretization size which was chosen to stay within reasonable computation time. Further discrepancies between the real and the assumed values of the effective dielectric function of gold might lead to the observed deviations.

In this thesis, the Green's tensor method was used to calculate the scattering spectra and the near-field of plasmonic nanostructures. Figure A.2 shows a scheme of the simulation procedure.

The first step consists in designing the system: geometry (mesh size, number and distribution) and illumination conditions (polarization of the incident plane wave, angle of incidence) and to the properties of the materials used (superstrate, substrate, metal), as shown in figure A.2 (A). The frequency dependent complex permittivity of gold was taken from the experimental data of Palik (1985). Then, the far field scattering spectrum can be computed, allowing to asses the resonance feature of the structure (figure A.2 (B)). Finally, the electric field intensity[1] distribution is calculated at a determined wavelength and region of interest (figure A.2 (C)).

[1]The field intensity $I = |E|^2$.

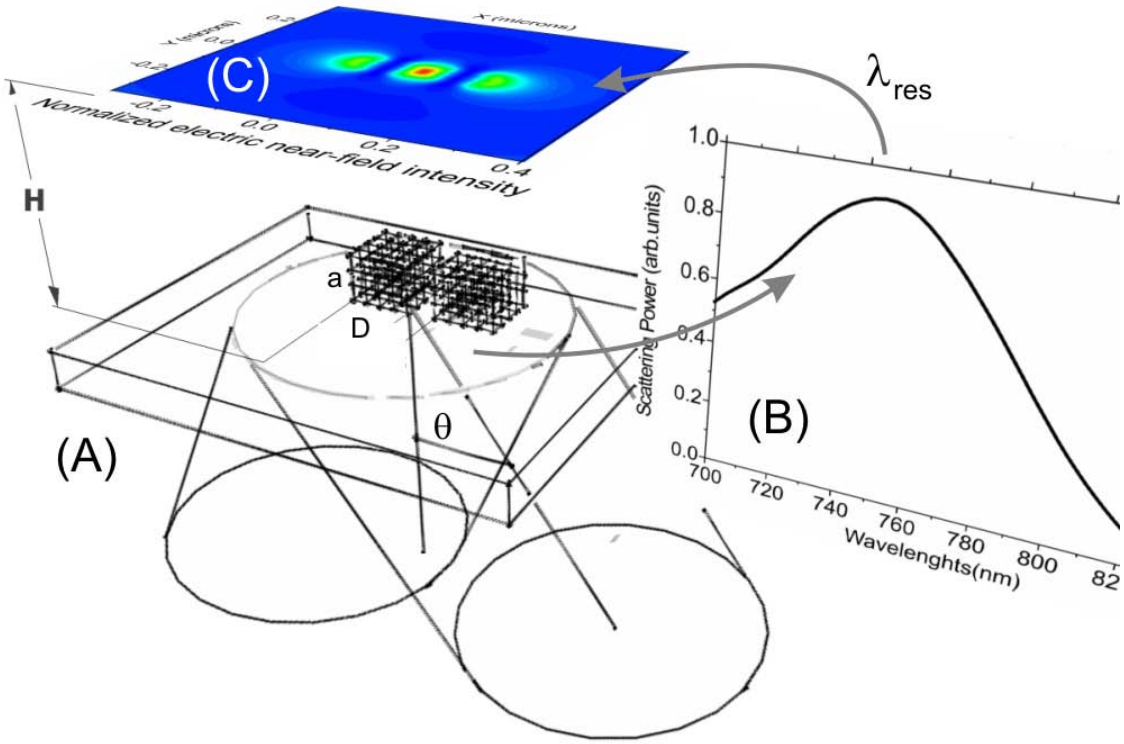

Figure A.2: *Scheme of the calculation procedure. (A) The system of interest is first defined (D - size of the particles, a - mesh size, incidence angle), (B) Computed scattering power spectrum, (C) Near-field map calculated at H above the structures.*

A. THEORETICAL CALCULATIONS: THE GREEN'S DYADIC METHOD

References

Girard, C. & Quidant, R. (2004). Near-field optical transmittance of metal particle chain waveguides. *Opt. Express*, **12**, 6141–6146.

Girard, C., Weeber, J.C., Dereux, A., Martin, O.J.F. & Goudonnet, J.P. (1997). Optical magnetic near-field intensities around nanometer-scale surface structures. *Phys. Rev. B*, **55**, 16487–16497.

Greffet, J.J. & Carminati, R. (1997). Image formation in near-field optics. *Prog. Surf. Sci.*, **56**, 133 – 237.

Martin, O.J.F., Girard, C. & Dereux, A. (1995). Generalized field propagator for electromagnetic scattering and light confinement. *Phys. Rev. Lett.*, **74**, 526–529.

Palik, E., ed. (1985). *Handbook of Optical Constants of Solids*. Academic Press, New York.

Quidant, R. (2002). *Dispositifs Optiques Submicroniques: Nanofabrication et Caracterisation en Champ Proche*. Ph.D. thesis, Equipe Optique Submicronique, Laboratoire de Physique, Universit de Bourgogne.

Appendix A

Sample Nano-Fabrication

In this work, the samples consisting of an arrangement of gold nanostructures are fabricated by an e-beam lithography technique [A.Hohenau *et al.* (2006); Quidant *et al.* (2004)]. The system we used is a FEI-QUANTA 200 scanning electron microscope equipped with a Raith-Elphy+ advanced lithography control. The most important steps of the process (figure A.1) are the following:

1. A layer of indium tin oxide (ITO) of 10 nm is deposited by e-beam deposition on a well cleaned glass substrate. ITO combines optical transparency with electrical conductivity to evacuate the charges created by the electron beam. To increase its transparency the coated glass was previously heated on a hot plate at 300 °C for one hour.

2. A Polymethyl methacrylate (PMMA) film with a thickness of typically three times the height of the desired structure was spin coated onto the substrate and then baked for two hours at 175 °C (figure A.1 (A)).

3. The resist was patterned using e-beam at an acceleration voltage of 30 kV.

4. After exposure, the PMMA resist was developed using MIBK:IPA (3:1).

A. SAMPLE NANO-FABRICATION

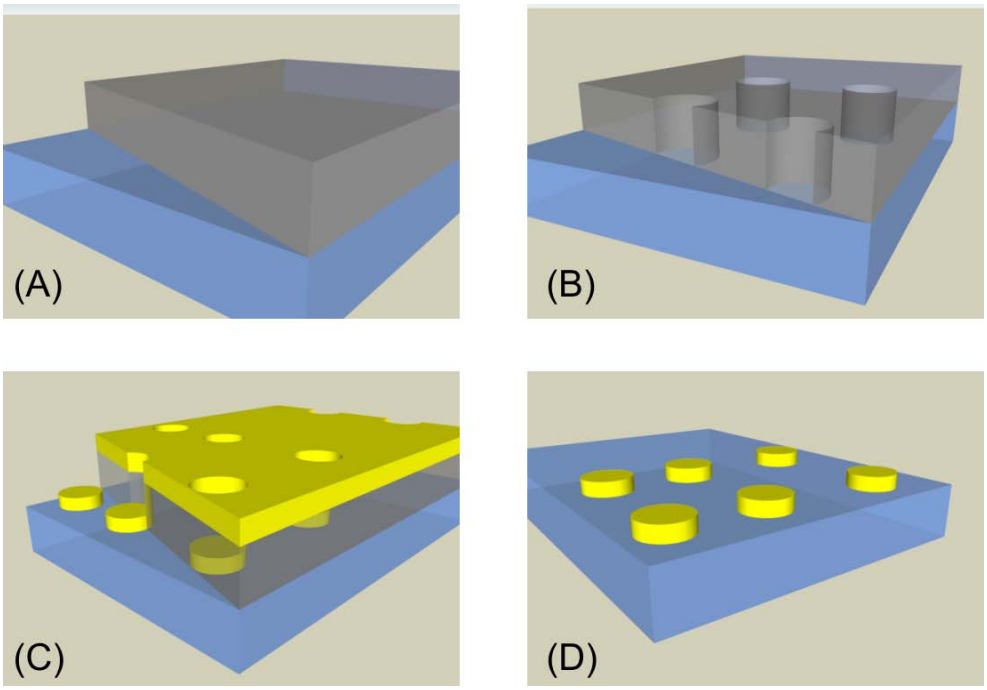

Figure A.1: *Sample fabrication using e-beam lithography. (A) A PMMA film is spin coated on the ITO coated glass substrate, (B) The positive resist is patterned using the electron beam, (C) The gold layer is deposited, (D) Final sample after lift-off.*

5. A 2 nm Ti adhesion layer and a Au layer was deposited using e-beam evaporation and thermal evaporation respectively (figure A.1 (C)).

6. The pattern was recovered onto the substrate using a lift-off process. The resist is dissolved and the top gold layer is removed (figure A.1 (D)).

After lift-off, the quality of the sample was checked with the scanning electron microscope (SEM). In figure A.2 is shown a sample that still maintains the different layers of the process. The in-plane size and shape of the nanostructures is controlled by changing the exposure beam parameters (dose, current or spot size) and their height by the gold evaporation.

With this method the nanostructures are created at desired locations, typically in periodic arrays of 50 to 100 μm. The separation between them is chosen smaller

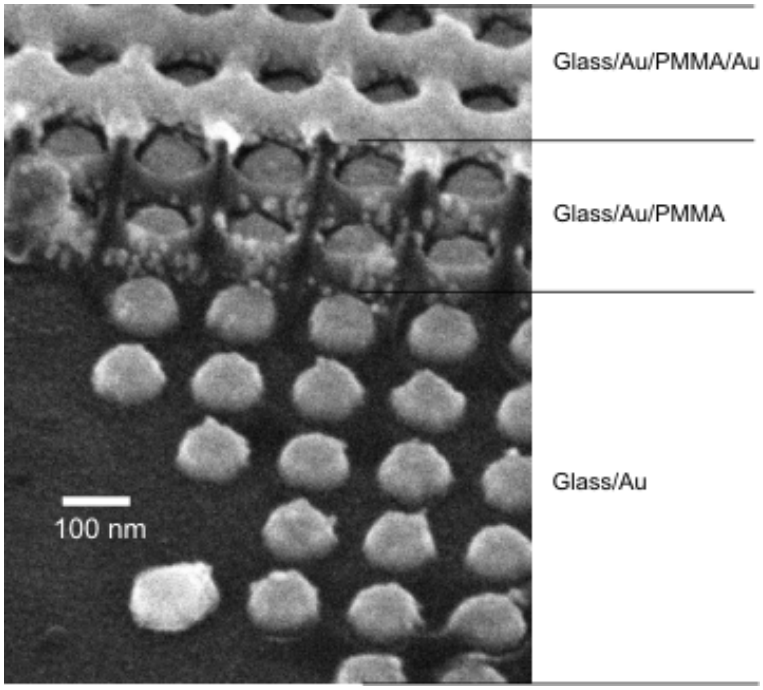

Figure A.2: *Side view of a sample with gold nanoparticles prior to the lift-off. The sample was scratched to allow a better view of the processes. Scale bar 100 nm. Courtesy of Nano-Optics Group, Institute of Physics - Karl Franzens University, Graz*

than 300 nm or bigger than 1μm in order to avoid diffraction orders that may disturb the measurement of plasmonic resonances [Lamprecht *et al.* (2000)].

For coupled nanostructures, the most difficult task is to assure a good reproducibility of the gap size (figure A.3). Typically the size resides around the resolution limit of the microscope (0 to few tens of nm) [Rechberger *et al.* (2003); Schuck *et al.* (2005); Sundaramurthy *et al.* (2006)].

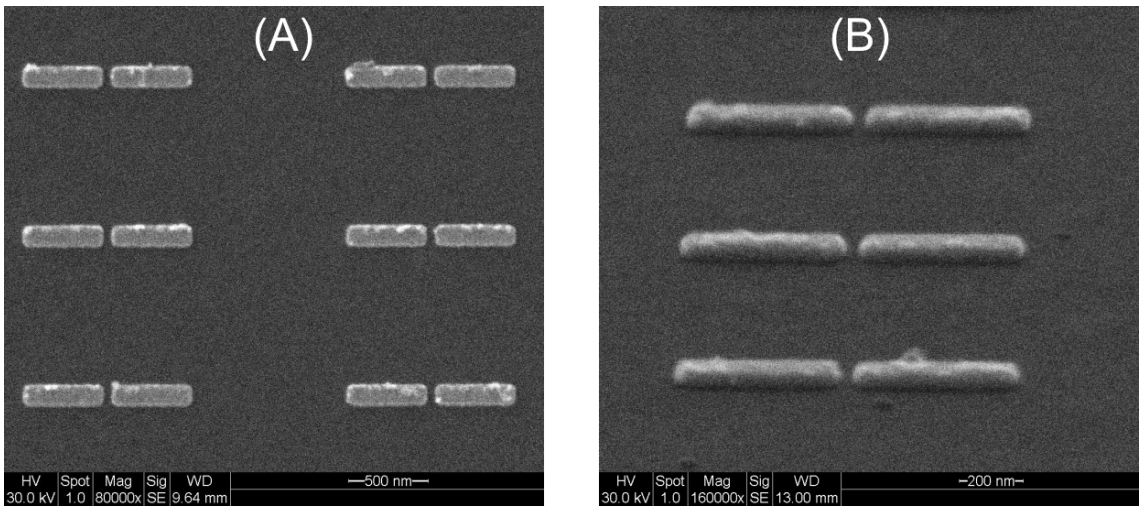

Figure A.3: *Nanoantennas fabricated by e-beam lithography with a 30 nm gap. (A) top view and (B) side view. Scale bars: 500 and 200 nm respectively.*

References

A.Hohenau, H.Ditlbacher, B.Lamprecht, J.R.Krenn, A.Leitner & F.R.Aussenegg (2006). Electron beam lithography, a helpful tool for nanooptics. *Microelec. Engin.*, **83**, 1464.

Lamprecht, B., Schider, G., Lechner, R.T., Ditlbacher, H., Krenn, J.R., Leitner, A. & Aussenegg, F.R. (2000). Metal nanoparticle gratings: Influence of dipolar particle interaction on the plasmon resonance. *Phys. Rev. Lett.*, **84**, 4721–4724.

Quidant, R., Badenes, G., Cheylan, S., Alcubilla, R., Weeber, J.C. & Girard, C. (2004). Sub-wavelength patterning of the optical near-field. *Opt. Express*, **12**, 282–287.

Rechberger, W., Hohenau, A., Leitner, A., Krenn, J.R., Lamprecht, B. & Aussenegg, F.R. (2003). Optical properties of two interacting gold nanoparticles. *Opt. Comm.*, **220**, 137–141.

Schuck, P.J., Fromm, D.P., Sundaramurthy, A., Kino, G.S. & Moerner, W.E. (2005). Improving the mismatch between light and nanoscale objects with gold bowtie nanoantennas. *Phys. Rev. Lett.*, **94**, 017402.

Sundaramurthy, A., Schuck, P.J., Conley, N.R., Fromm, D.P., Kino, G.S. & Moerner, W.E. (2006). Toward nanometer-scale optical photolithography: utilizing the near-field of bowtie optical nanoantennas. *Nano Lett.*, **6**, 355–360.